Design, Processing and Characterization of High Entropy Alloys for High Temperature Applications

A Thesis Submitted in

Partial Fulfillment of the Requirements

For the Degree of

DOCTOR OF PHILOSOPHY

by

SUJIT DAS

(Roll No: 146103005)

DEPARTMENT OF MECHANICAL ENGINEERING

INDIAN INSTITUTE OF TECHNOLOGY GUWAHATI

GUWAHATI-781039, INDIA

SEPTEMBER 2022

Department of Mechanical Engineering

Indian Institute of Technology Guwahati

Guwahati-781039,

INDIA

CERTIFICATE

It is certified that the work contained in the thesis entitled "**Design, Processing and Characterization of High Entropy Alloys for High Temperature Applications**" submitted by **Mr. Sujit Das** (Reg. No. **146103005**) to the Indian Institute of Technology Guwahati for the award of degree of Doctor of Philosophy has been carried out under my supervision in the Department of Mechanical Engineering, Indian Institute of Technology Guwahati. This work has not been submitted elsewhere for the award of any other degree or diploma.

The thesis, in my opinion, has reached the standard fulfilling the requirements for the award of degree of Doctor of Philosophy in accordance with the regulations of the institute.

Professor P. S. Robi

Department of Mechanical Engineering

Indian Institute of Technology Guwahati

Guwahati-781039

INDIA

DEDICATED TO

I would like to dedicate this thesis to my

loving mother Mrs. Sugati Das and

Father Mr. Nrusingha Charan Das

whose huge patience and sacrifice

makes me able to get such success.

I would also be grateful for my

lovely sister Mrs. Nibedita Das

whose boundless support and guidance

made it possible for me to complete this work.

ACKNOWLEDGEMENTS

First and foremost, my love and gratitude goes to the God, the Almighty, for His showers of blessings throughout my work to complete the research successfully.

I would like to express my deepest appreciation to my mentor, philosopher and guide Prof. P. S. Robi for his continuous support, suggestion, motivation and immense knowledge. He has taught me the methodology to carry out the research and to present the research work as clearly as possible. It was a great privilege and honor to work and study under his guidance. I am extremely grateful for what he has offered me. I would also like to thank him for his friendship, cooperativeness and great sense of humor.

Besides my guide, I owe a deep sense of gratitude to my doctoral committee members, Prof. R. Ganesh Narayanan, Prof. S. Kanagaraj and Prof A. Srinivasan for their encouragement, insightful comments and hard questions during the period of my research work.

My sincere gratefulness to Prof. S. Senthilvellan, Head of the Department, Mechanical Engineering, Indian Institute of Technology, Guwahati for his huge support by providing his research equipments during the most

necessary period. I would highly appreciate all the friendly workshop staffs specially Mr. D. Khaklary and Mr. Gokul Das for their commendable suggestions and constant supports from the beginning to the end of my research work.

My special gratitude is for Dr. Sidananda Sharma, Department of Physics, Indian Institute of Technology Guwahati for his warm support and friendliness at the most important periods of my research work.

I would like to acknowledge all the staffs of the Central Instrumentation Facility, IIT Guwahati specially Mr. Chandan Borgohain, Dr. Kula Kamal Senapati, Dr. Dolly Gogoi, Dr. Ashim Malakar, Ms. Rumi Rani Pao and Mr. Sujit Deb for their timely support in providing the instruments during my research work.

Finally I would whole heartily like to thank my colleagues and friends who gave me the most important mental support in my research work especially to Mr. Pranay Kumar Sarkar, Mr. Saptarshi Dutta, Mr. Pritam Kumar Rana, Mr. Biswajyoti Das, Mr. Ramesh Kumar, Miss. Aneeta Padhan, Mr. Samrat Tamuly, Mr. Brijesh Pandey, Mr. Pronot Kumar and Mr. Saurabh Kumar Nishad.

2nd September 2022 *Sujit Das*

ABSTRACT

High entropy alloys (HEAs) are a novel class of alloys that contain multiple principal elements. HEAs possess high mixing entropy that inhibits the formation of multiple phases in them by reducing their Gibbs free energy, especially at high temperature. Refractory high entropy alloys (RHEAs) generally have BCC structure and possess very high mechanical strength at elevated temperatures. Fabrication of RHEAs is difficult due to the high melting point of individual elements. Transition metal HEAs contain transition elements. These HEAs often contain Al that tailors the fraction of BCC or FCC phases. Transition metal HEAs containing Cu are difficult to crystallize due to their low solid solubility that causes segregation of Cu-rich phases. Guo et al. proposed the basic criteria to design the equiatomic HEAs in order to achieve high solid solubility by considering three design parameters such as enthalpy of mixing (ΔH_{mix}), entropy of mixing (ΔS_{mix}) and radius ratio (δ). In this research work, two RHEAs such as WMoVCrTa and $W_{23}Mo_{23}V_{17}Cr_8Ta_7Fe_{22}$, and one Al and Cu contained transition metal HEA such as $(Al)_{10}(FeCoNiCu)_{90}$ were designed based on alloy design criteria of Guo et al. and Takeuchi et al., and fabricated subsequently. To minimize the difficulties in processing the alloys, mechanical alloying by ball milling was done prior to the consolidation. Milling characteristics of the alloys were established. The milled WMoVCrTa powder revealed two BCC phases such as BCC1 and BCC2 having the lattice parameters of 3.16 Å and 2.88 Å respectively. The milled $W_{23}Mo_{23}V_{17}Cr_8Ta_7Fe_{22}$ powder revealed a single BCC phase having the lattice parameter of 3.143 Å. The milled $(Al)_{10}(FeCoNiCu)_{90}$ powder revealed two FCC phases such as FCC1 and FCC2 having the lattice parameters of 3.60 Å and 5.21 Å respectively. The as-milled WMoVCrTa and $W_{23}Mo_{23}V_{17}Cr_8Ta_7Fe_{22}$ powders were cold compacted followed by vacuum arc melted and heat treated, whereas the milled $(Al)_{10}(FeCoNiCu)_{90}$ powder was cold compacted and sintered to fabricate the alloy ingots. The structure, mechanical and tribological properties of the alloys were determined. The two

RHEAs show very high mechanical strength at room and elevated temperatures. WMoVCrTa and $W_{23}Mo_{23}V_{17}Cr_8Ta_7Fe_{22}$ respectively exhibited yield strength retention of 79% and 90% of the room temperature value, at 1000 °C. They also have reasonable ductility both at room and high temperature, and very high hardness. The $Al_{10}(FeCoNiCu)_{90}$ exhibits high mechanical strength and ductility. The two RHEAs have higher wear resistance than that of high-speed steel (HSS). The valuable mechanical and tribological properties possessed by these alloys indicate that they are viable materials for high temperature applications viz., turbine blade coating, refractory lining, nuclear reactor walls, coating on cutting tools, etc.

CONTENTS

LIST OF FIGURES

LIST OF TABLES

NOMENCLATURE

ΔG_{mix}	Gibb's free energy change of mixing
ΔH_{mix}	Enthalpy change of mixing
ΔH^{AB}_{mix}	Enthalpy change of binary AB alloy
ΔS_{mix}	Entropy change of mixing
T_m	Effective melting temperature of ***n*** constituents
T_{mi}	Melting temperature of i^{th} element
c_i	Atomic percentage of i^{th} element
c_j	Atomic percentage of j^{th} element
Ω_{ij}	Melt interaction parameter between the i^{th} and j^{th} element
R	Universal gas constant
δ	Atomic size difference parameter
r_i	atomic radius of i^{th} element
$\bar{r}$	Average atomic radius of the constituent elements
S_σ	mismatch entropy parameter
k_B	Boltzmann constant
d_i	Atomic diameter of i^{th} element
d (0.5)	Average size of 50% particle volume
R_a	Roughness average
R_p	Height of the highest profile peak
R_v	Depth of the deepest profile valley
R_z	Mean roughness depth

Abbreviations

HEA	High entropy alloy
RHEA	Refractory high entropy alloy
MPEAs	Multi Principal Element Alloys
BMGs	Bulk metallic glasses
BCC	Body centered cubic
FCC	Face centered cubic
HCP	Hexagonal closed pack
TEM	Transmission electron microscope
SEM	Scanning electron microscope
XRD	X-ray diffraction
WEDM	Wire-cut Electro Discharge Machining
HV	Vickers hardness
HRTEM	High resolution transmission electron microscope
EDS / EDX	Electron dispersive X-ray spectroscope
LM	Light microscope
UTM	Universal testing machine
SAED	Selected area electron diffraction
YSA	yield-stress anomaly
HDBSD	High definition backscattered electron detector
IFFT	Inverse fast Fourier transformation
PDF	Powder Diffraction File
FWHM	Full width at half maximum
VEC	Valence electron concentration
SE2	Secondary scanning electron
COF	Coefficient of Friction

Chapter 1

Introduction

High entropy alloys (HEAs) are a new class of alloys containing multiple principal elements and exhibiting very high strength with reasonable ductility [1-3]. The special characteristics of these alloys are that their microstructure and mechanical properties are stable from room temperature to very high application temperatures. Till the beginning of the 21st century, alloy developments by researchers were based on the concept of having a major metallic element into the lattice of which small amount of other metals were added in order to achieve some specific properties. Some of these alloy developments were the alloys of Fe, Al, Mg, Cu, etc. and the later being the Ni super alloys. The major technological advancements were achieved during the last century in the development of Ni-based super alloys for high temperature gas turbine materials especially for aerospace applications. Ni-based super alloys have been developed for applications up to 1130 °C [4], which is above 78% of the melting point of Ni and a far higher homologous temperature than any other structural material. Currently the development of Ni-based super alloys has almost reached saturation. Hence researchers are focusing their attention in development of new alloys that demand still higher working temperature for future applications.

In the pursuit of developing novel materials with enhanced properties to further increase the efficiency of the engines working at high temperatures, novel alloy design strategy has evolved since 2004. This led to the development of HEAs which was centered on mixing of at least 5 principal metals with atomic percentages from 5 to 35 [1, 2]. The proposed philosophy was based on the thermodynamics of solutions where the alloy should have the mixing entropy (ΔS_{mix}) of $\geq$ 1.61R, where R is the universal gas constant. This was based on the hypothesis that the $\Delta S_{mix} \geq 1.61R$ can reduce the Gibbs free energy and eases the yield of solid solution phases

by suppressing the formation of a number of intermetallic compounds in the HEAs. This led to evolve of different definitions and terminologies for these HEAs on later periods and at the same time evolution of different design criteria.

New alloys that have been developed based on the proposed HEA design criteria are capable for use in a wide range of applications due to their combination of stable microstructure and properties over a wide range of temperature, viz, high hardness, high strength at room and elevated temperature, unique electrical and magnetic properties, high wear resistance, high oxidation and corrosion resistance etc. [5]. The rationales behind achieving these outstanding properties have been assumed to be due to four core effects viz, severe lattice distortion, sluggish diffusion, high entropy, and cocktail effects [12]. In spite of these assumptions, extensive investigation is highly required to have a fundamental understanding of the alloy formation, viable processing techniques, micro-structure that can be formed and processing-structure-property correlation in HEAs.

Over the past decade the characterization, design, and optimization of the high entropy alloys were mostly focused on achieving a Face-Center Cubic (FCC) structure in the alloy containing transition metal elements such as: Fe, Ni, Co, Cr, Mn, Zn, Ti, Cu, Sn, Zn etc) [11, 13-18, 24, 25]. Some of these HEAs were processed by addition of aluminum with atomic percentage $\leq$ 10, to obtain stable FCC structure [5]. The investigations carried out in the FCC HEAs revealed good phase stability, superior mechanical properties, stable microstructure and very good corrosion resistance at high temperatures below 800°C. The excellent high temperature properties by the FCC alloys are generally associated with high stacking fault energy. However, the transition metal HEAs that contain Copper as one of the constituents are difficult to crystallize in only FCC phases due to the segregation of Cu-rich phases [3, 5, 19-21, 126]. Though the Copper causes segregation, it facilitates nano-twin that enhances the work hardening of HEAs [34]. Proper processing methods to fabricate Cu-contained HEAs are

required to be identified to minimize the segregation effect. The method of 'mechanical alloying' by ball milling of powder mixtures has been found to be effective for eliminating the segregation in one of the Cu-contained HEAs [22]. This shows the feasible direction in processing the Cu-contained HEAs in order to crystallize them in only FCC phase.

Recently few refractory HEAs (RHEAs) containing high melting point elements such as W, Mo, V, Cr, Nb, Ta, Hf and Ti have been developed to obtain enhanced mechanical properties and stable alloy structure for very high temperature applications [7-10, 26]. These RHEAs were found to have BCC crystal structure and some of them exhibited very high mechanical strength at temperature above 1000°C [7-10, 26]. Senkov et al. reported that the two alloys of NbMoTaW and VNbMoTaW, processed by arc melting technique show excellent compressive yield strengths up to 1600°C [9]. Guo et al. reported equiatomic MoNbHfZrTi RHEA possessing excellent compressive yield strength up to 1100°C [10]. Juan et al. processed two alloys of HfMoTaTiZr and HfMoNbTaTiZr exhibiting high compressive strength up to 1200°C [26]. Chen et al. reported the results on NbMoCrTiAl alloy that indicated high compressive strength up to 1000°C [27]. Though the RHEAs exhibit excellent strength, their ductility has been found to be poor [9-10, 18, 27-29].

Despite the fact that RHEAs possess very good mechanical properties for high temperature applications, the processing of these alloys still remains a challenge. Major difficulties encountered while processing them by liquid melting techniques are: (a) conventional crucible materials are incapable to hold the molten RHEA due to its extremely high melting temperature; (b) large variation in the melting temperature of the constituent elements of RHEA, hence some of the elements start vaporizing at the melting temperature of high melting point elements (eg. Boiling point of Cr is 2672 °C where as the melting point of W is 3422 °C) resulting in porous alloy and at the same time obtaining inconsistent composition and non-homogeneity in structure like coring and segregation, (c) the large difference between the densities of the constituents in

RHEAs resulting in inherent defects [30]. It appears that RHEAs can be processed by PM technique that has the following advantages over the solidification [8, 30]. (i) The intrinsic enthalpy of reaction during processing is the thermally efficient driving force for densification thereby overcoming the requirement of very high furnace temperatures, (ii) The material can be processed at low (sintering) temperatures where volatilization of the low melting point elements is prevented resulting in a non-porous and chemically homogeneous material, (iv) The technique has the unique advantage of successfully processing several alloys and compounds which cannot be prepared by conventional melt techniques, especially in systems containing elements with remarkably different melting points. (v) The material processed by P/M technique is free of coring and segregation that are observed in the products produced by melting technique, (vi) Grain size distribution is narrow in materials prepared by P/M route, (vii) Near net shaped components can be obtained ensuring minimum material wastage and circumventing the need of machining process.

The Vacuum arc melting process is a viable method to produce the RHEAs due to the extremely high arc temperature (~3000 °C). However, the melting point of some refractory elements such as W and Ta (i.e. 3017 °C for Ta and 3422 °C for W) are such higher than the expected arc temperature that a proper melting of these elements to obtain a homogeneous alloy will be difficult. In such cases, the melting point can be reduced if the raw material for the melting is in the form of a homogenous alloy powder which can be achieved by mechanical alloying (i.e. by ball milling). Ball milling is a complex process where the deformation between different powder particles occur due to the impact between balls, hence atoms of different elements are forced into non equilibrium positions. Hence through ball milling, the mixture of metal powders transforms to alloy powder by cold welding / fracturing resulting in homogeneous solid solution alloy at the atomic level. This lowers the melting temperature of the alloy thereby facilitating processing the alloy by arc melting. For example, melting temperature

of the ball milled alloy powder of WMoVCrTa and $W_{23}Mo_{23}V_{17}Cr_8Ta_7Fe_{22}$ are estimated to be 2849° C and 2880° C respectively [132]; whereas that of W is 3422 °C and Ta is 3017 °C. Hence the combination of ball milling and subsequent arc melting appears to be a viable method for processing the RHEAs.

The broad objectives of the present study are to design and fabricate three alloys (two RHEAs having BCC structure and one transition metal HEA having FCC structure) for high temperature applications; study the extent of mechanical alloying; characterize the microstructure of the alloys and investigate their mechanical properties.

The thesis contains five chapters. Chapter 1 briefly introduces the research area and explains the main significance of the thesis work. A detailed literature survey related to the present topic is summarized in Chapter 2. The research gaps and objectives of the thesis work are also discussed at the end of this chapter. Chapter 3 is the 'Experimental Procedure' that describes the detailed procedures followed for the fabrication and characterization of the alloys which includes ball milling of powder mixture, extend of alloying, characterization techniques like particle size analysis, XRD, SEM, TEM, UTM, Micro-hardness testing, etc. In Chapter 4, the results obtained have been presented and discussed in detail. The main conclusions arrived at from the present work and the future scopes of investigation have been highlighted in Chapter 5. This is followed by references.

Chapter 2

Literature Survey

2.1 Introduction

The concept of HEAs was first proposed by both Yeh and Cantor in 2004; however the progress in this topic was slowed down till 2010. But thereafter the advancement of HEAs took a leap that more than 10000 research articles have been published globally on this field till now. In the last two decades the reports were mainly based on the HEAs containing 3d transition metals (from atomic number of 21 to 29 in periodic table) that exhibited superior properties than superalloys. The structure-property correlation was also established to some extent for these HEAs. The design principles for choosing those HEA combinations was also established but not fully justified due to some mismatch with the experimental results. Hence the HEAs processed by a suitable alloy design principle were less followed. Beyond 3d transition metals, a few reports were obtained for the HEAs consisting of refractory metals (W, Mo, V, Cr, Ta, Hf, Zr, Nb, Ti, Re, Ru, Os, Rh) that exhibited very promising and superior properties than the conventional super alloys. To rationalize these promising properties, some most allied thermodynamic and other basic concepts were established for both 3d transition metal and refractory HEAs. In this chapter, these concepts were briefly discussed and successively the fundamental design principles for HEAs were explicated. The structure, notable properties and their rationalizations for some most important 3d transition metal HEAs and refractory HEAs were subsequently highlighted.

2.2 Thermodynamic concept

HEAs are multi element alloys. The basic principle behind HEAs is the high mixing entropy which tends to stabilize the solid solution phases in the alloy rather than forming a number of inter-metallic phases, especially at high temperatures. Inter-metallics are usually ordered phases

with lower configurational entropy whereas the HEAs have disordered phases. The reason behind possessing high entropy in HEAs evolves from the application of statistical thermodynamics for determining the stability of the alloys. The statistical entropy of any solid material can be obtained considering the degeneracy in the energy states of a typical crystalline solid which mainly has three primary sources such as (a) electronic entropy, (b) Vibrational entropy and (c) configurational entropy which are explained below.

A. Electronic entropy (S_e): The valence electrons in the solid can be distributed in many different ways over the quantum states available to them, which produce the electronic entropy, S_e. The electronic entropy is much higher in a metal than in a semiconductor or insulator. There are many empty electron states that have energies comparable to those that are occupied by the valence electrons, and hence there are many distinguishable ways in which the electrons can be distributed without changing the energy or violating the Pauli Exclusion Principle. The electronic entropy of a semiconductor or insulator is much smaller since almost all of the valence electrons are confined to particular atomic or bonding states that are very nearly full.

B. Vibrational entropy (S_v): Crystalline solids have vibrational entropy. It occurs due to the thermal oscillation of the atoms about their equilibrium positions in the crystal lattice. The motions of the individual atoms are correlated in quantized vibrational states called phonon and hence the degeneracy remains finite. The small displacements associated with the lattice vibrations significantly increase the degeneracy of the crystalline phase. The vibrational entropy decreases with the strength and directionality of the crystal bonds, thereby inhibits atom displacements. Further, the S_v increases with the openness of the crystal structure. Hence very stable, high-melting temperature solids tend to have relatively low vibrational entropies. Metals with the more open structure like BCC structure tend to have higher

vibrational entropies compared to the same metals in the close-packed structures like FCC or HCP crystals.

C. Configurational entropy (S_c): In multi-component solids, various chemical species can be distributed over different atom sites in its structure in many different ways. Hence they have configurational entropy. The number of distinct configurations can be calculated by assuming a system with $\boldsymbol{N}$ total sites. Out of the $\boldsymbol{N}$ atom sites there are $\boldsymbol{N_A}$ atoms of type A and $\boldsymbol{N_B}$ atoms of type B. Hence $\boldsymbol{N = N_A + N_B}$. The different ways of distributing $\boldsymbol{N}$ atoms over $\boldsymbol{N}$ sites are $\boldsymbol{N!}$. However, distributions that differ only through the interchange of A atoms with one another or B atoms with one another are physically indistinguishable. Since there are $\boldsymbol{N_A!}$ ways of redistributing the A atoms over the sites occupied by A atoms in a given configuration, and $\boldsymbol{N_B!}$ ways of redistributing the B atoms, the total number of distinguishable configurations is

$$\Omega = \frac{\boldsymbol{N}!}{\boldsymbol{N_A}!\boldsymbol{N_B}!} \tag{1}$$

Ω is the randomness of the system. If the energy of the crystal is independent of the way in which the atoms are distributed then its configurational entropy is

$$\boldsymbol{S_c} = \boldsymbol{k}\ln(\Omega) = \boldsymbol{k}[\ln(\boldsymbol{N}!) - \ln(\boldsymbol{N_A}!) - \ln(\boldsymbol{N_B}!)] \tag{2}$$

Where k is the Boltzman's constant.

By the sterling approximation,

$$\ln(\boldsymbol{N}!) = \boldsymbol{N}\ln(\boldsymbol{N}) - \boldsymbol{N} \tag{3}$$

Hence the configurational entropy can be written as

$$\begin{aligned} \boldsymbol{S_c} &= \boldsymbol{k}[\boldsymbol{N}\ln(\boldsymbol{N}) - \boldsymbol{N_A}\ln(\boldsymbol{N_A}) - \boldsymbol{N_B}\ln(\boldsymbol{N_B})] \\ &= -\boldsymbol{kN}[\boldsymbol{x}\ln(\boldsymbol{x}) + (1-\boldsymbol{x})\ln(1-\boldsymbol{x})] \end{aligned} \tag{4}$$

where x is the atom fraction of A.

Unlike the crystalline solids, in the glass or amorphous solids the atom positions are distributed in a less regular way and are not confined to any crystal lattice and hence has additional entropy. Hence the entropy of the solids with amorphous configuration of atoms or molecules is always greater than that of the same metal with crystalline structure. Although total mixing entropy has four contributions such as configurational, vibrational, magnetic dipole, and electronic randomness, the configurational entropy is dominant over other three contributions.

From equation (4) the mixing entropy change per mole for the formation of a solid solution from *N* elements with x_i mole fraction is

$$\Delta S_{mix} = -R \sum_{i=1}^{N} x_i \ln x_i \tag{5}$$

Where R is the universal gas constant (8.314 J/K mol)

From the above equation, ΔS_{mix} for equiatomic alloy system is R ln (*N*). For five element ΔS_{mix} is R ln (5) = 1.61R. For a non-equiatomic HEA, the mixing entropy would be lower than that for an equiatomic alloy. Table 2.1 shows the mixing entropy values of equiatomic alloys with constituent elements up to 13. Hence the entropy increases as the number of element increases.

Table 2. 1 The mixing entropy values for alloys with different number of equi-atomic elements.

N	1	2	3	4	5	9	7	8	9	10	11	12	13
ΔS_{mix}	0	0.69R	1.1R	1.39R	1.61R	1.79R	1.95R	2.08R	2.2R	2.3R	2.4R	2.49R	2.57R

From Richards' rule,

$$\Delta H_f / T = \Delta S_f \approx R \tag{6}$$

where, ΔH_f is the enthalpy change or latent heat per mole, T is the melting point of the alloy. The entropy change per mole, ΔS_f, during solid to liquid is about 1*R*, and ΔH_f can be

estimated as RT. In a random solid solution, the mixing entropy of R per mole (i.e $\Delta S_{mix} = 1R$) is large enough to lower its Gibb's free energy of mixing ΔG_{mix} by the amount of RT, since $\Delta G_{mix} = \Delta H_{mix} - T\Delta S_{mix}$. The free energy lowering causes the solid solution phases to have a higher stability compared to inter-metallic compounds which usually have much lower ΔS_{mix} due to their ordered nature. This indicates that the tendency to form the mixing state of elements is higher in HEAs due to increased mixing entropy, especially at high temperatures. In addition, mixing entropy smaller than 1R is expected to have less power to compete with the strong bonding energies. It is evident from the Table 2.2 (see below) that the traditional alloys have entropy smaller than 1R whereas some concentrated alloys of Ni-base, Co-base super alloys, and BMGs have entropy between 1.13 and 1.37R. That means none of the traditional alloys have mixing entropy ≥ 1.61R (mixing entropy for quinary equiatomic HEAs). Hence the stability of these traditional alloys at high temperature is less than that of equiatomic quinary HEAs.

Table 2. 2. Configurational entropies calculated for typical traditional alloys at their liquid state or random state.

Systems	Alloys	ΔS_{conf} at liquid state
Low alloy steel	4340	0.22R (low)
Stainless steel	304	0.96R (low)
	316	1.15R (medium)
High speed steel	M2	0.73R (low)
Mg alloy	AZ91D	0.35R (low)
Al alloy	2024	0.29R (low)
	7075	0.43R (low)
Cu alloy	7-3 Brass	0.61R (low)
Ni base super-alloy	Inconel 718	1.31R (medium)
	Hastelloy X	1.37R (medium)
Co base super-alloy	Stellite 6	1.13R (medium)
BMG	$Cu_{47}Zr_{11}Ti_{34}Ni_8$	1.17R (medium)
	$Zr_{53}Ti_5Cu_{16}Ni_{10}Al_{16}$	1.30R (medium)

2.3 Core Effect concepts of HEAs

The concepts for remarkable properties in HEAs were first proposed by Yeh et.al called as 'Core Effects' [33]. The four most basic or core effects that affect the microstructure and the properties of the HEAs are:

a. High entropy effect
b. Severe lattice distortion
c. Sluggish diffusion
d. Cocktail effect

Briefly, considering thermodynamics, high entropy effect could inhibit the complex phase formation. From structural point of view, severe lattice distortion effect could alter alloy properties to an extent. The sluggish diffusion effect could slow down the phase transformation process. The overall properties of the HEAs can be enhanced by the cocktail effect.

a. High entropy effect

High entropy effect is the most important effect because it can enhance the solid solution and makes the microstructure much simpler than expected. The entropy of mixing ΔS_{mix} is expressed in equation 5. ΔS_{mix} for equiatomic alloy system is R ln (N). Here N is the number of elements in the HEA system. So at high temperatures, and taking more number of elements, the Gibbs free energy of the HEA becomes lower due to the contribution of larger ΔS_{mix}. From the Gibbs free energy relationship, a competing effect exists between the enthalpy and entropy. If an element in the alloy has strong repulsion force (or large positive mixing enthalpy) to other elements, then that element will segregate to form an elemental phase with little solubility with other elements. That means, mixing entropy effect is not sufficient to overcome the large enthalpy effect. Suppose the element has weak repulsion force (small positive mixing enthalpy)

with other elements, its segregation phase will contain reasonable concentration of other elements due to mixing entropy effect and becomes a concentrated solid solution with a major element. In general, if the enthalpy of mixing for unlike atomic pairs has smaller difference, simple solid solution phases would be formed in the equilibrium state.

b. Severe lattice distortion effect

Because the multi-component matrix of each solid solution phase in HEAs is a whole-solute matrix, every atom is surrounded by different kinds of atoms and thus suffers lattice strain and stress mainly due to the atomic size difference. Besides atomic size difference, different bonding energy and crystal structure among constituent elements are also expected to cause even higher lattice distortion. This can be due to the non-symmetrical neighboring atoms resulting in non-symmetrical bonds and electronic structure around an atom and such non-symmetry varies from site to site. Hence the overall lattice distortion would be more severe in HEAs compared to the conventional alloys where most matrix atoms (or solvent atoms) have the same kind of atoms as their neighbors. Lattice distortion causes electron scattering and significant decrease in electrical conductivity. So it reduces the electron contribution to thermal conductivity by electron conduction. So lattice distortion reduces thermal effect on HEAs. Also in the heavily distorted lattice, large solution hardening results in the increase in hardness and strength.

c. Sluggish diffusion effect

HEAs mainly contain random solid solutions and/or ordered solid solutions. Since their matrix could be regarded as whole-solute matrix, the diffusion of an atom in the whole-solute matrix would be very different from that in the matrix of conventional alloys. A vacancy in the whole-solute matrix is in fact surrounded by different-element atoms during diffusion. Slower diffusion and higher activation energy occurs in HEAs due to larger fluctuation of lattice potential energy (LPE) between lattice sites. The abundant low-LPE sites can serve as traps and

hinder the diffusion of atoms. This leads to the sluggish diffusion effect. It is also found that the greater the number of elements, the slower is the diffusion rate. Sluggish diffusion provides various advantages in controlling microstructure and properties, *viz.*, easiness to get supersaturated state and fine precipitates, increased re-crystallization temperature, slower grain growth, reduced particle coarsening rate, and increased creep resistance. In general, sluggish diffusion is favorable for improving properties of HEAs.

d. Cocktail effect

Since HEAs consists of at least 5 elements, these alloys can have either/or a single phase, two phases, three phases, or more depending on the composition and processing. The overall property of the HEA therefore can evolve from the overall contribution of all the constituent phases. This relates with the phase size, shape, distribution, phase boundaries, and properties of each phase. Moreover, each phase is a multi-component solid solution phase and can be regarded as an atomic-scale composite. Its composite properties not only come from the basic properties of elements by the mixture rule but also from the mutual interactions among all the elements.

2.4 HEA design criteria

The fundamental criteria to design an HEA are not established yet. The researchers generally commence the fabrication of HEA by taking the equiatomic combination of multiple elements. Later the equiatomic proportion of the elements in the HEA combination is altered to enhance the property. Though the literatures on HEA design are few, they are essential to provide an initial route map to decide the combination of multiple elements for an HEA. Some design criteria are most vital to select the combination and predict the phase formation of HEAs such as:

a. Equiatomic HEA design criteria proposed by Guo et al [6].

b. Alloy design criteria proposed by Takeuchi et al [32].

The design criteria for equiatomic HEAs proposed by Guo et al. are important to predict the phase stability [6]. Guo et al. found that the configurational entropy is not the sole parameter to crystallize the HEAs in simple solid solution phases. After statistically analyzing a number of equiatomic HEA systems, they proposed some design parameters and their ranges that can perfectly predict the solid solution or amorphous phase formation in equiatomic HEAs.

The design parameters are as follows:

The Gibb's free energy change of mixing (ΔG_{mix}) of the HEA is determined by

$$\Delta G_{mix} = \Delta H_{mix} - T_m \Delta S_{mix} \tag{7}$$

where ΔH_{mix} is the change in enthalpy of mixing (J mol^{-1}), T_m is the effective melting temperature of $\boldsymbol{n}$ constituents in Kelvin ($\boldsymbol{n}$=5 in the present work) and ΔS_{mix} is the change in mixing entropy (J mol^{-1} k^{-1}) and is expressed in equation 5 [6].

ΔH_{mix} is expressed by

$$\Delta H_{mix} = \sum_{i=1, i\neq j}^{n} \Omega_{ij} c_i c_j \tag{8}$$

where c_i and c_j are atomic percentages of the i^{th} and j^{th} components, Ω_{ij} is the melt interaction parameter between the i^{th} and j^{th} element which is expressed by

$$\Omega_{ij} = 4\Delta H_{mix}^{AB} \tag{9}$$

where ΔH_{mix}^{AB} is the enthalpy change of binary AB alloy (J mol^{-1}), which is determined using the Miedema's model table [31]. For the current refractory and non-refractory alloys, the ΔH_{mix}^{AB} obtained from Miedema's table are given in Table 2.3.

Table 2. 3 Enthalpy change of (a) refractory and (b) non-refractory binary alloy pairs obtained from Miedema's table.

Cr	-1	0	-7	-2	1
-1	**Fe**	-2	-15	-7	0
0	-2	**Mo**	-5	0	0
-7	-15	-5	**Ta**	-1	-7
-2	-7	0	-1	**V**	-1
1	0	0	-7	-1	**W**

(a)

Al	-11	-19	-22	-1
-11	**Fe**	-1	-2	13
-19	-1	**Co**	0	6
-22	-2	0	**Ni**	4
-1	13	6	4	**Cu**

(b)

The effective melting temperature T_m of ***n*** components is determined by rule of mixtures and is expressed by

$$T_m = \sum_{i=1}^{n} c_i (T_m)_i \tag{10}$$

where $(T_m)_i$ and c_i are respectively the melting temperature and atomic percentage of i^{th} element.

The atomic size difference parameter (δ) for solid solution formation is defined by

$$\delta = 100 \sqrt{\sum_{i=1}^{n} c_i \left(1 - \frac{r_i}{\bar{r}}\right)^2} \tag{11}$$

where r_i and $\bar{r}$ are the atomic radius of i^{th} element and average atomic radius of the constituent elements respectively. The $\bar{r}$ is defined as

$$\bar{r} = \sum_{i=1}^{n} c_i r_i \tag{12}$$

Valence electron concentration (VEC) is useful for determining phase stability and can be calculated by

$$\mathrm{VEC} = \sum_{i=1}^{n} c_i (\mathrm{VEC})_i \tag{13}$$

where $(\mathrm{VEC})_i$ is the VEC for the i^{th} element.

Guo et al. found that solid solution phases are expected when the three conditions are simultaneously satisfied. They are:

$$-22 \text{ kJ/mol} \leq \Delta \boldsymbol{H_{mix}} \leq 7 \text{ kJ/mol},$$

$$11 \text{ J mol}^{-1} \text{ K}^{-1} \leq \Delta \boldsymbol{S_{mix}} \leq 19.5 \text{ J mol}^{-1} \text{ K}^{-1}$$

$$\text{and } 0 \leq \boldsymbol{\delta} \leq 8.5.$$

Guo et al. also noted that larger VEC (≥8) favours the formation of FCC-type solid solutions, while smaller VEC (<6.87) favours the formation of BCC-type solid solutions [6].

Takeuchi and Inoue established the mismatch entropy parameter (S_σ) that predicts the probability of formation of crystalline or amorphous phase in multi-component alloy system by estimating the atomic size difference effect [32]. The formation of amorphous phase is favored at higher values of S_σ/k_B and vice-versa [32]. The parameter S_σ is determined by Eq. (14) as:

$$S_\sigma = k_B \left[\frac{3}{2}(\zeta^2 - 1)y_1 + \frac{3}{2}(\zeta - 1)^2 y_2 - \left\{\frac{1}{2}(\zeta - 1)(\zeta - 3) + ln\zeta\right\}(1 - y_3)\right] \quad (14)$$

Here k_B is the Boltzmann constant. ζ is a parameter defined as $\zeta = 1/(1- \acute{\varepsilon})$, where $\acute{\varepsilon}$ is the packing fraction. For BCC and FCC structures $\acute{\varepsilon}$ values are 0.68 and 0.74 respectively. y_1, y_2 and y_3 are dimensionless parameters having relation $y_1 + y_2 + y_3 = 1$ and are defined by Eq. 15, 16 and 17 below.

$$y_1 = \frac{1}{\sigma^3} \sum_{j>i=1}^{3} (d_i + d_j)(d_i - d_j)^2 c_i c_j \quad (15)$$

$$y_2 = \frac{\sigma^2}{(\sigma^3)^2} \sum_{j>i=1}^{3} (d_i d_j)(d_i - d_j)^2 c_i c_j \quad (16)$$

$$y_3 = \frac{(\sigma^2)^3}{(\sigma^3)^2} \quad (17)$$

Where $\sigma^k = \sum_{i=1}^{3} c_i d_i^k$; $k = 2, 3$. The d_i represents atomic diameter of i^{th} element and c_i and c_j are atomic percentages of the i^{th} and j^{th} component.

2.5 Crystal structure of HEAs

In alloys, tailoring the microstructure can tailor their mechanical and physical properties. Hence details study of microstructure as well as structure property correlations should be established for HEAs. The HEAs are mostly reported to possess either single/multiple solid solution (SS) phases or Intermetallic (IM) phases or both SS+IM phases. A SS phase with atoms of different alloying elements occupying random lattice sites in crystal lattices is described as a disordered SS phase (e.g. FCC, BCC and HCP). The SS phase with atoms occupying certain preferred lattice sites in crystal lattices are referred as ordered SS phase (e.g. L12, B2 or B4). The IM phases (e.g. Sigma or Laves) are firmly ordered phases. All the disordered and ordered SS phases are classified in HEA family as simple phases. The only SS contained or SS+IM contained HEAs are commonly reported in literatures. Only IM phases in HEAs are less reported.

FCC or BCC SS phase in HEAs are frequently reported and so far a few HCP phase HEAs are obtained [34]. AlxCoCrFeNi [35-37], CoCrCuFeNi [38-40], CoCrCuFeMnNi [1, 41, 42], CoCrFeMnNi [2, 43, 44] are reported as some of the common single FCC phase HEAs. However, Schuh et al. investigated that although the CoCrFeMnNi HEA has single FCC phase, after annealing and subsequent plastic deformation the alloy possess three more phases [17]. Those phases are MnNi, FeCo and a Cr-rich phase observed by Transmission Electron Microscopy (TEM) and Atom Probe Tomography (APT) analysis in his work [17]. The transition metal HEAs with BCC phase commonly contain Al, Cr and Fe and some also contain Ti, Si and BCC refractory metals [5, 32, 45, 46]. Refractory HEAs showing single BCC structure contain BCC refractory metals with small amount of Al, Hf, Ti and Zr [9, 10, 47, 48, 49, 50, 51]. Dual phase (BCC+FCC) HEAs generally consist of transition metals.

Al and Cu are most effectual elements in 3d transition metals but the HEAs with Cu as one of the constituents are difficult to crystallize in single phase due to the segregation of Cu or

Cu-rich phases [5, 19, 20, 21]. Though pure Al crystallizes in FCC structure but it performs as a BCC stabilizer in HEAs. For example, Tong et al. reported the $Al_xCoCrCuFeNi$ HEA that crystallizes in only FCC phase if $x < 0.8$, FCC+BCC phases if $0.8 < x < 1$ and only BCC phase if $x > 1$ [52]. Zhang et al. also reported that the phase change from FCC to BCC in $Ti_xCoCrFeNiCu_{1-y}Al_y$ alloy occurs on increasing Al content [53]. This is due to the increase in atomic level stress on addition of large Al atoms [54, 55]. FCC structures have high atomic packing density than BCC structures. Thus addition of Al in FCC HEAs increase atomic level stress and hence transition of FCC to BCC occurs when atomic percentage of Al exceeds 11 [5] in order to reduce the stress and Gibbs free energy. Annealing also changes the proportion of BCC or FCC phase in the dual phase BCC+FCC HEAs, depending on the temperature induced. Wen et al. reported the HEA system of Al-Co-Cr-Cu-Fe-Ni that contains both FCC+BCC phases [15]. The phase fraction of BCC increases in the corresponding HEA system if annealed below 800°C and the phase fraction of FCC increases if the annealing temperature is above 800°C [15]. The increase in BCC phase increases brittleness and hardness of the corresponding HEA whereas the increase in FCC phase makes the alloy ductile and softer. However Ng et al. found that annealing for long duration leads to the formation of IM (σ) phase that makes the HEA hard and less ductile [56]. Hence tailoring the annealing temperature can tailor the phases and properties in HEAs. The ordered L12 phase is generally appeared with the HEAs crystallizing in FCC structure [34]. The ordered B2 phase is generally appeared with the HEAs crystallizing in BCC structure [34]. All B2 and L12 phases are reported in HEAs containing Aluminium [34]. The precipitation of IM phases are mostly reported in transition metal HEAs and barely exhibited by RHEAs [34].

2.6 Transition metal HEAs

The nuclear, turbine and aerospace industries strongly demand advanced materials that can be fulfilled by the transition metal HEAs as they exhibit high compressive strength and hardness at

both room and elevated temperature. Some transition metal HEAs exhibit very good tensile properties such as strength and ductility. Overall, the literatures show that these HEAs possessing FCC structure exhibit low strength and high ductility and possessing BCC structure exhibit high strength and low ductility. Hence, the crystal structure plays an important role in controlling the mechanical properties of these HEAs. Some important reports on the mechanical properties of these HEAs are outlined below.

2.6.1 Mechanical properties

Hardness results of different transition metal HEAs were reported frequently in various literatures [57-67]. The literatures show that the only FCC phase HEAs have Vickers hardness ranges from 100-200 HV and the only BCC phase HEAs have Vickers hardness > 600HV. The alloys having both FCC+BCC phases show high Vickers hardness if the fraction of BCC phase is higher and vice-versa. Li et al. and Tung et al. reported that the increase in the B2 phase fraction increases the hardness of the HEAs [39, 68]. Ivchenko et al. and Welk et al. investigated that the $Al_xCoCrCuFeNi$ HEAs possessing BCC + B2 structure have high hardness values [69, 70]. In the same HEAs the hardness is proportional to the content of Al [69, 70]. This is due to the reason that with the increase in Al, the alloy changes from FCC to FCC+BCC and then to single BCC structure [5]. Precipitation of IM phases increases the hardness and strength in the HEAs. Stepanov et al., Shu et al. and Chen et al. reported that the increase in the fraction of IM (Laves and σ) phases present in FCC or FCC+BCC HEAs resulted in increase in hardness [71, 72, 73]. Shun et al. reported that due to the precipitation of IM (σ) phase by the addition of Mo in the AlCoCrFeNi HEA, the strength increases from 1051 MPa to 2757 MPa [74]. Chen et al. noticed that the addition of Ti in $Al_{0.5}CoCrCuFeNiTi_x$ HEA increases the hardness to 600 HV or higher due to the presence of IM phase when the value of x is larger than 1 [75]. Chuang et al. stated that the annealing of Ti-contained HEAs increases their hardness due to the formation of more IM phases [76]. Tsai et al. reported a Mn-contained HEA of $Al_{0.3}CrFe_{1.5}MnNi_{0.5}$ that on aging in

600-900°C increases its hardness value from 300 HV to 900 HV due to the transformation of BCC to σ phase [77]. HEAs with BCC and B2 structures possess high compressive yield strength in the range from 1300-2400 MPa with the compressive ductility mostly below 10% which is regarded as a standard minimum value for structural applications [34]. The HEAs exhibiting FCC structure have lower compressive strength and higher ductility [15]. The compressive strength and ductility generally behave inversely but Liu et al. reported that in $Al_xCrFeNiTi_{0.25}$ HEA, the maximum ductility and compressive strength was achieved at x = 0.5 and then the ductility and compressive strength both decreases as the x increases or decreases [78]. The presence of intermetallic phase in the FCC or BCC HEAs affects the ductility [34]. Stepanov et al. and Salishchev et al. found that the ductility decreases quickly as the volume percentage of intermetallic phases reaches a critical value [71, 79]. Zhuang et al. affirmed that the ductility can be increased by annealing the alloy but it results in decreasing the strength [80].

Otto et al. in the tensile test experiment of CoCrFeMnNi HEA showed that the tensile strength and strain of the HEA decreased as the service temperature increased from -196°C to 800°C [81]. Deformation occurs in the corresponding HEA due to nano twinning at 77K when $\varepsilon \geq 20\%$. Nano twinning was not seen below room temperature at low strain in the corresponding HEA. The primary deformation mechanisms in the FCC HEAs are deformation slip and twin [34]. Stepanov et al. also reported the tensile test data of the above HEA after cold rolling that exhibited higher tensile stress of more than 1200 MPa due to the presence of small grains [82]. Schuh et al. reported the tensile test results on the same HEA that possess very high tensile strength of 1950 MPa due to the reduction of the grain size after plastic deformation [17]. Kuznetsov et al. found that the $Al_xCoCrCuFeNi$ HEA (at x=16.7 at. %) shows brittle to ductile transition above 873 K; however above 973 K it shows superplasticity with tensile elongation of 1240% [83, 84, 85]. Some reports also show that the Sn addition in the HEAs increases ductility. Liu et al. investigated the tensile properties of the $CoCuFeMnNiSn_x$ HEA and found that the

ductility increases till the x reaches a value of 0.03 [86]. Liu et al. also investigated the tensile properties of the $CoCuFeNiSn_x$ HEA and found that both the ductility and strength increases in the HEA till $x \leq 0.07$ [87]. Ma et al. reported a single crystal FCC HEA of $Al_{0.3}CoCrFeNi$ possessing room temperature ultimate tensile strength and high ductility of 399 MPa and 80% respectively [88].

2.6.2 Mechanical properties at cryogenic temperature

A few reports are available on the mechanical properties of the transition metal HEAs at cryogenic temperature out of which some are discussed below. Stepanov et al. investigated the microstructure in CoCrFeNiMn during plane-strain multi-pass rolling to a thickness strain of 80% at 293K and at 77 K [89]. The key deformation mechanism in the corresponding HEA at both the temperatures was associated with twinning. At 77 K, the twinning was more extensive in terms of the fraction of twinned grains and the length of the twinning stage, which resulted in faster kinetics of the microstructure evolution. Micro-shear bands were formed in the microstructure of the corresponding HEA at the later stages of rolling (at ε = 80% for 293 K and at ε =40% for 77 K). The ultimate tensile strengths of corresponding HEA specimens rolled at 77 K and 293 K were found to be 1500MPa and 1200 MPa respectively [89]. Qiao et al. also reported the mechanical properties of an HEA at cryogenic temperature that the compressive yield strength and fracture strength of a BCC structured AlCoCrFeNi HEA at 77 K are 1880 MPa and 3550MPa respectively while at 298 K are 1450 MPa and 2960 MPa respectively [90]. The fracture strains of the corresponding HEA at 77 K and 298 K were 14.3% to 15.5% respectively [90].

2.6.3 Tribological properties

Chuang et al. processed the $Al_xCo_{1.5}CrFeNi_{1.5}Ti_y$ HEAs with different Al and Ti content by arc melting and compared their adhesive wear behavior with conventional wear resistant steels SUJ2 and SKH51 [91]. The wear resistance of the $Co_{1.5}CrFeNi_{1.5}Ti$ and

$Al_{0.2}Co_{1.5}CrFeNi_{1.5}Ti$ alloys is at least two times better than that of conventional wear-resistant steels with similar hardness [91]. The anti-oxidation and resistance to thermal softening properties in these HEAs are the key reasons for the excellent wear resistance. Wu et al. prepared the $Al_xCoCrCuFeNi$ HEAs with different aluminum contents by arc melting and subsequently investigated for adhesive wear behaviors [92]. With increasing Al content, both the volume fraction of BCC phase and the hardness value increases, and thus the wear coefficient decreases in the corresponding HEA. Moreover, the wear mechanism changes from delamination wear to oxidative wear. For low aluminum content, $x = 0.5$, the microstructure of the HEA is FCC and the worn surface is deeply grooved and undergoes a periodic delamination which produces big debris. For medium aluminum content, $x = 1.0$, the microstructure is FCC + BCC, and the worn surface is deeply grooved in FCC region but smooth in BCC region. Delamination wear is still dominant though oxidative wear occurs in the smooth region. For high aluminum content, $x = 2.0$, the microstructure is BCC and the worn surface is smooth and yields fine debris with high oxygen content. The high Al content in the above HEA enhances wear resistance highly [92].

2.6.4 Distinctive properties

Hemphill et al. observed the fatigue strength of a cold rolled $Al_{0.5}CoCrCuFeNi$ HEA [94]. The four point bending fatigue on this HEA determined the endurance limit between 540 and 945 MPa [94]. The corresponding HEA shows promising fatigue strength as that of the steels and Ti alloys. The Al-Cu contained HEA of $Al_{10}(FeCoNiCu)_{90}$ was developed to investigate for structural applications due to their combination of high strength and ductility [93]. The corresponding HEA can also be investigated for engineering materials due to its viability of being fabricated richly at industry level [93]. The fracture toughness of some HEAs was also reported. Roy et al. reported the plane strain fracture toughness of the $Al_{23}Co_{15}Cr_{23}Cu_8Fe_{15}Ni_{15}$ HEA using single-edged notch bend and chevron-notched rectangular bars whose K_{IC} values are

5.8 ± 0.2 MPa-$m^{1/2}$ and 5.4 ± 0.2 MPa-$m^{1/2}$ respectively [95]. Gludovatz et al. reported the crack initiation fracture toughness of CoCrFeMnNi HEA at room temperature as J_{IC}= 250 KJ-m^{-2} and the stress intensity as K_{JIC}= 217 MPa-$m^{1/2}$ [96]. The 3d transition metal HEAs were also reported for stacking fault energies [97], single crystal elastic modulus [88] and shear modulus with Poisson's ratio [98].

2.7 Refractory HEAs (RHEAs)

RHEAs are in their infant stage of development unlike transition metal HEAs. In structural applications the Ni based super alloys have shown promising properties such as good fatigue strength, fracture toughness, creep strength, tensile ductility, oxidation resistance and wear properties. High temperature properties of these super alloys are still lacking for requirement in turbine and aerospace applications that may achieve by some new RHEAs [9, 34]. These RHEAs mostly contain refractory elements (some contain small amount of Al or Si) and generally crystallize in BCC phase. Small amount of laves phases often crystallize with the BCC phase if the RHEA contain V or Cr. The mechanical properties particularly the compression and hardness results for this type of RHEAs were often reported. Some of the important results for the RHEAs are discussed below. Senkov et al. found that the Vickers hardness of $Al_{0.5}MoNbTa_{0.5}TiZr$ is as high as 5.8 GPa [100]. The experimental hardness values of the RHEAs are commonly greater than the hardness calculated by rule of mixture. Senkov et al. reported that the hardness of MoNbTaVW and HfNbTaTiZr were achieved as 5250 and 3826 MPa respectively whereas the corresponding values by rules of mixture were more than three times lower than the above experimental values [101, 102]. The hardness values for different RHEAs can be found from several reports [9, 10, 47, 48, 49, 100, 101, 102, 103, 104, and 105]. At high temperature, most of the RHEAs show better compressive properties than INCONEL 718 and MAR-M 247 (Figure 2.1) [34]. Senkov et al. reported two RHEAs of MoNbTaW and MoNbTaVW that show exceptional compressive strengths (> 400 MPa) still at 1600 °C [9].

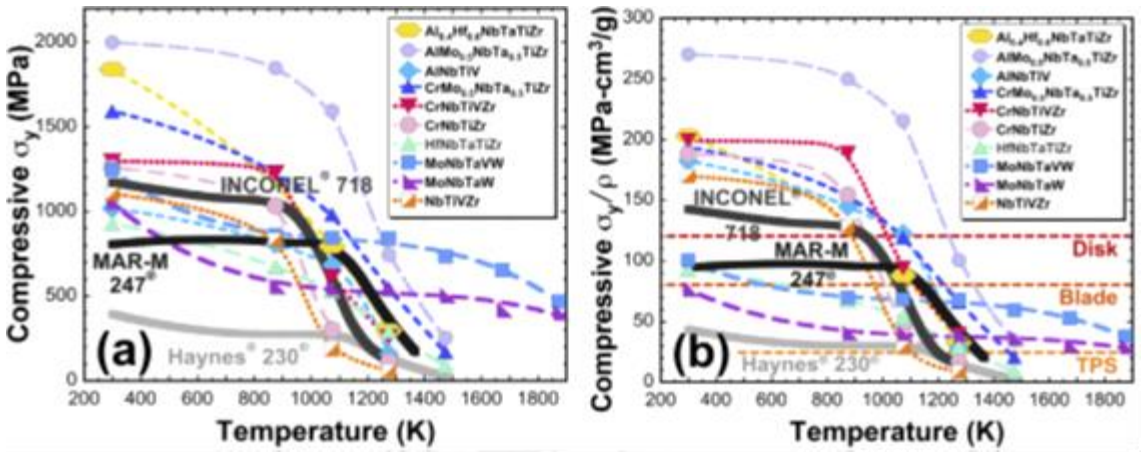

Figure 2. 1. Comparison of the compressive properties of different HEAs with INCONEL 718 and MAR-M 247 alloys [34].

Although high compressive strengths were obtained for these RHEAs at elevated temperatures, their ductility lacks at room temperature [9, 10, 18, 27-29]. The density values of the RHEAs are also high. Hence to improve ductility and simultaneously to reduce density, addition of Al in small quantity were intended with RHEAs. Senkov et al. reported that the two RHEAs such as $Al_{0.4}Hf_{0.6}NbTaTiZr$ and $AlMo_{0.5}NbTa_{0.5}TiZr$ show less density and good room temperature compressive ductility (≥10%) [100]. Al based RHEAs also show promising compressive strengths at elevated temperatures [100 and 106]. Though some RHEAs, without containing Al have less room temperature compressive ductility, there high temperature compressive stress and strain values are very high [9, 10, 48, 104, 107]. The tensile strength data of these HEAs are less reported. Only two RHEAs till date are tested for room temperature tensile test and they are HfNbTiZr and HfNbTaTiZr [49, 108]. HfNbTaTiZr was the first RHEA that cold rolled successfully among the BCC HEAs processed till date [108]. The oxidation resistance properties of this RHEA group are less reported yet. Senkov et al. reported that the $NbCrMo_{0.5}Ta_{0.5}TiZr$ RHEA shows parabolic weight gain due to oxidation after 100 hours at 1273 K [99]. Liu et al. also reported non-protective linear oxidation by an RHEA at 1573 K [109]. The enhanced mechanical properties in RHEAs enable them suitable for application in

high temperature coatings in gas turbines. Several RHEAs exceed the range of the properties such as specific strength, compressive strength and maximum use temperature of conventional super alloys [34]. The high temperature compressive ductility of some RHEAs are also notable that estimates the possibility of achieving good high temperature tensile ductility [9, 10, 48, 104, 107].

In spite of exhibiting good mechanical properties and stable structure at high temperatures, the reports on the tribological properties of the RHEAs are only a few but impressive [110, 111, 112, 113]. Poulia et al. reported that the wear resistance of the RHEA of $Mo_{20}Ta_{20}W_{20}Nb_{20}V_{20}$ is much better than that of the Inconel 718 [110]. Bhardwaj et al. found that the addition of Al increases the wear resistance in the RHEA of $Al_xTiZrNbHf$ (x = 0, 0.25, 0.50, 0.75, 1) [111]. Sadeghilaridjani et al. showed that the wear rate of two RHEAs of HfNbTiZr and HfNbTaTiZr decreased on increasing the temperature from 423 K to 573 K due to the formation of protective oxide layers on the alloy surface [112]. Pole et al. reported that the wear mechanism for HfTaTiVZr and TaTiVWZr changed from adhesive and abrasive wear at 298 K to severe oxidative wear at 573 K and 723 K [113].

2.8 Summary

The summary of the literature in HEAs reveal the following major findings:

a. Almost 90 % of the reports of HEAs to date contain transition metal elements with or without small addition of Mo, Si, Sn etc. The Al is often added with these HEAs to control the crystal structure as well as various properties. These HEAs exhibit high compressive strengths and hardness at room temperatures. The correlations in composition-structure-property for these alloys were studied to some extent.
b. The 3d transition metal HEAs containing Cu are difficult to crystallize in single phase due to the segregation of Cu or Cu-rich phases in the alloy after processing.

c. So far the reports on RHEAs are very few that mainly consist of combination of refractory elements like Hf, Nb, Ta, Ti, V, Zr, W, Mo, Cr etc. RHEAs generally crystallize in BCC structure with or without small amount of intermetallic phases. The study for establishing correlations in composition-structure-property for these RHEAs is at its infant stage. Some reports on these alloys identify excellent mechanical properties even at extremely high temperature which shows their potential to employ in various high temperature applications required for jet engines, turbine industries and nuclear reactors.

d. Majority of the work carried out for transition metal HEAs or RHEAs were mainly aimed at investigating their crystal structures and determining mechanical properties (strength and hardness only).

2.9 Research Gaps

- A few literatures are available regarding the application of the new alloy design concepts for obtaining HEAs and RHEAs with stable microstructure.
- The structure and property of RHEAs and their correlations are less established.
- High temperature deformation studies of RHEAs are very few.
- The Cu containing transition metal HEAs are less studied.
- The study on tribological characteristics of HEAs and RHEAs are very limited.

2.10 Current Research Objectives

The main objectives of the present study are:

- To design, fabricate and characterize (a) two BCC HEAs and (b) one FCC HEA for high temperature applications.
- Two BCC HEAs should have five refractory metals (W, Mo, V, Cr and Ta) to achieve a stable high strength BCC alloy at elevated temperatures.
- The FCC HEA should have five metals such as Cu, transition metals (Fe, Co, Ni), and Al (< 10 at. % to obtain FCC HEA) to achieve high ductility.

- To design and fabricate the above three HEAs by proper processing techniques; i.e. for the two BCC refractory HEAs the combination of ball milling and arc melting, and for FCC HEA the combination of ball milling and sintering to be followed.
- To investigate the extent of alloying during ball milling of the elemental powder mixtures of the three HEAs.
- To determine the crystal structure and study the microstructure of the HEAs.
- To determine mechanical properties (viz, hardness, compressive properties at room and elevated temperatures), and establish the structure-property correlations of the above HEAs.
- To investigate the tribological properties of the HEAs and compare them with that of a commercial high-speed steel (HSS) tool.

CHAPTER 3

RESEARCH METHODOLOGY

3.1 Introduction

In this research work, three HEAs were developed. The first two were RHEAs, and the third one was Al and Cu contained transition metal HEA. The current chapter describes the detailed procedures followed in the design and fabrication of the three HEAs. This contains the initial procedure of selection of the elements for the three HEAs, fabrication methods of HEA powder and arc melted ingots and the techniques of characterization of the alloy powders and ingots.

3.2 Alloy Selection

The outlines of the selection and preparation of the three HEAs are briefly explained below.

Alloy-1

The work commenced by choosing equiatomic combination of multiple elements for the first HEA. The initial equiatomic powder combination of five elements was selected with the conditions and reasons such as they (i) should have high melting points for high temperature application, (ii) should be of BCC structure for high strength application, (iii) should be from refractory groups of the periodic table, (iv) radius difference among them should be less than 15% and (v) should satisfy design criteria by Guo et al for equiatomic HEAs and (vi) should satisfy the Takeuchi et al's mismatch entropy criteria. The powder combination of '$W_{20}Mo_{20}V_{20}Cr_{20}Ta_{20}$' satisfy the above five criteria. The corresponding powder mixture was subsequently mechanically alloyed by ball milling process. Milling characteristics of the powder mixture such as particle size variation, crystal structure, microstructure and morphology change throughout the milling was studied.

To prepare the alloy ingots, the corresponding milled powder was cold compacted and melted by vacuum arc melting technique and subsequently heat-treated in vacuum to enhance the properties. The crystal structure and microstructure of the alloy ingots were investigated. Hardness, room and high temperature mechanical properties of the alloy were determined. Tribological properties of the alloy were investigated and compared with other alloys at the end.

Alloy-2

Composition of Alloy-2 was decided by altering the composition of Alloy-1 to non-equiatomic proportion in order to enhance the properties. The atomic percentages of W, Mo were increased in the current RHEA to enhance the mechanical strength and hardness. The atomic percentages of Cr and Ta were decreased highly to reduce the amount of intermetallic phase. The Fe was added in RHEA to enhance the ductility. The final powder combination was verified for mismatch entropy criteria and decided to be of the non equiatomic combination as $W_{23}Mo_{23}V_{17}Cr_8Ta_7Fe_{22}$. The corresponding non-equiatomic RHEA powder was mechanically alloyed by ball milling process. The milled powders were analyzed for determining particle size change, crystal structure evolution, microstructure and morphology.

To prepare the alloy ingots, the corresponding milled powder was cold compacted and melted by vacuum arc melting technique and subsequently heat-treated in vacuum. The crystal structure, microstructure, hardness and mechanical strength (at room and high temperature) for the cast alloy were investigated. Tribological properties of the alloy were investigated and compared with other alloys at the end.

Alloy-3

For this transition metal FCC HEA, powder combination of five elements was selected with the conditions and reasons such as they (i) should be from the transition metal group of the periodic

table, (ii) radius difference among them should be less than 15% and (iii) less than 10 at. % of Al should be added with the combination to achieve FCC structure (iv) should satisfy the Takeuchi et al's mismatch entropy criteria. The authors arrived at the combination of the five elements such as $(Al)_{10}(FeCoNiCu)_{90}$ that satisfied the above four conditions. The Cu was taken in HEA. The above powder mixture was subsequently processed by ball milling. The particle size variation, chemical composition analysis and crystal structure evolution in the powder mixture during progressive milling were determined. The alloy ingots were fabricated by cold compacting, followed by sintering of the milled powder mixture. The crystal structure, microstructure and room temperature mechanical of the alloy ingot were investigated. Tribological properties of the alloy were investigated and compared with other alloys at the end.

3.3 Raw materials

The composition details of the three alloy powder mixtures (Alloy 1, 2 and 3) and their specifications are shown in this section. The composition of starting refractory and transition metal powder mixtures are shown by atomic percentage in Table 3.1 and Table 3.2, respectively. The Table 3.3 shows the details of all starting powders. The SEM micrographs of the elementary refractory powders selected for alloy preparation are shown in Figure 3.1.

Table 3. 1 Composition of starting refractory powder mixture

	W (at. %)	**Mo (at. %)**	**V (at. %)**	**Cr (at. %)**	**Ta (at. %)**	**Fe (at. %)**
Alloy-1	20	20	20	20	20	0
Alloy-2	23	23	17	8	7	22

Table 3. 2 Composition of starting transition metal powder mixture

	Al (at. %)	**Fe (at. %)**	**Co (at. %)**	**Ni (at. %)**	**Cu (at. %)**
Alloy-3	10	22.5	22.5	22.5	22.5

Table 3. 3 Details of starting powders

Elements	Size	Purity	Melting Temp (Kelvin)	Source
W	12 µm	99.9%	3695	Sigma-Aldrich
Mo	150 µm	99.9%	2896	Sigma-Aldrich
V	325 mesh	99.5%	2183	Sigma-Aldrich
Cr	60-100 mesh	99.0%	2180	Loba-Chemie
Ta	60-100 mesh	99.9%	3290	Sigma-Aldrich
Al	< 5 µm	99.5%	933	Sigma-Aldrich
Fe	250-300 µm	99.5%	1808	Loba-Chemie
Co	< 150 µm	99.9%	1767	Sigma-Aldrich
Ni	200 mesh	99.8%	1726	Loba-Chemie
Cu	< 45 µm	99.7%	1358	Sigma-Aldrich

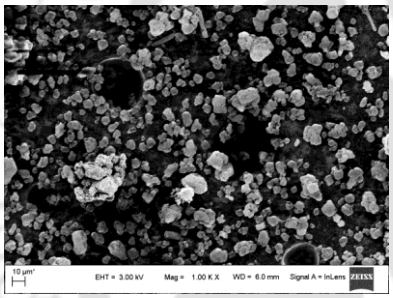

W

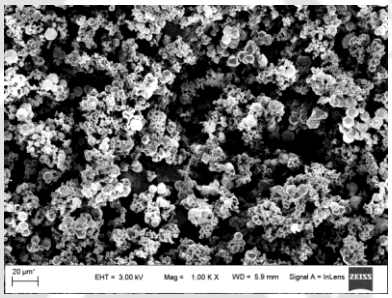

Mo

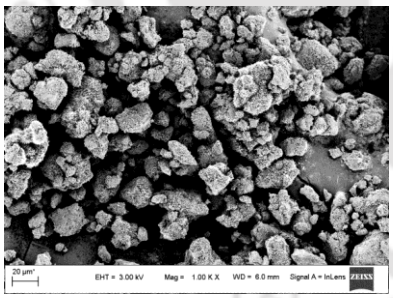

V

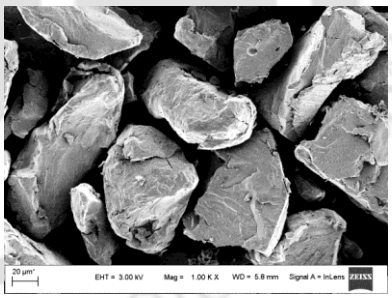

Cr

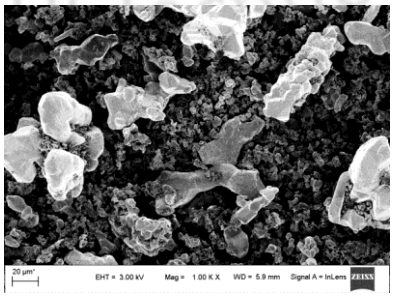

Ta

Figure 3. 1 SEM image of starting refractory powders

3.4 Mechanical alloying

The current section describes the details of the ball milling process followed for mechanically alloying three different powder combinations of WMoVCrTa, $W_{23}Mo_{23}V_{17}Cr_8Ta_7Fe_{22}$ and $Al_{10}(FeCoNiCu)_{90}$. Milling was performed in a high energy mono ball mill [PULVERISETTE 6, FRITSCH, Germany] with Tungsten vial and balls in dry condition (without any process control agent) in an Argon atmosphere. Total powder mixture of 40 g was taken and ball to powder weight ratio of 10:1 was maintained. A milling speed of 250 RPM was kept with relaxation time of 30 min after each hour of milling. Mechanical alloying was continued for 64 h, 48 hours and 80 hours for WMoVCrTa, $W_{23}Mo_{23}V_{17}Cr_8Ta_7Fe_{22}$ and $Al_{10}(FeCoNiCu)_{90}$, respectively. Sampling was carried out after regular intervals by taking 2 grams of milled powder mixture.

3.5 Fabrication of alloys

To consolidate the as-milled RHEA powders of WMoVCrTa and $W_{23}Mo_{23}V_{17}Cr_8Ta_7Fe_{22}$, they were first filled in the cylindrical rubber moulds (Figure 3.2 (a)) and cold compacted by cold isostatic press, model:AIP3-22-60WP (Figure3.2 (b)) at 40000 psi. The cold pressed cylindrical samples (Figure 3.2 (c)) were then melted by vacuum arc melting technique (Make: Vacuum Techniques (P) LTD. Bangalore, Model: VT-D2PP-01) to prepare the alloy ingots. The vacuum up to 10^{-6} torr was achieved in the sample chamber by rotary and diffuser pumps and the cold pressed samples were melted in a high purity Argon atmosphere by single Tungsten electrode. The melting was repeated for five times to attain good chemical homogeneity of the alloy ingots. The molten samples were finally gravity settled and molded for cylindrical shape by the blind hole chamber of cylindrical Copper mould. The molten sample was water cooled as water was circulated outside the Copper mould. The cold alloy samples, after high vacuum sealing in a quartz tube, were heat-treated in a muffle furnace [OKAY, BYSAKH & CO, India] at 900 °C for 48 h and subsequently furnace cooled. The final samples were cut by wire cut

EDM to achieve different dimensions. The photo of the alloy ingot of WMoVCrTa after machining by wire EDM is shown in Figure 3.3. The dimension of the alloy ingot is Φ3×6 mm.

Rubber moulds

(a)

Cold isostatic press

(b)

Cylindrical compacted powders

(c)

Figure 3. 2. (a, b) Cold pressing components and (c) final products

To consolidate the HEA powder of $Al_{10}(FeCoNiCu)_{90}$, the corresponding powder after 80 hours of milling was encapsulated in cylindrical rubber molds and cold compacted by a cold isostatic press (CIP) at 40 000 psi (model: AIP3-22-60WP). The cold-pressed cylindrical samples, after high vacuum (10^5 torr) sealing in a quartz tube, were sintered in a muffle furnace (OKAY, BYSAKH & CO, India) at 1100°C for 48 h.

Figure 3. 3. Alloy ingot of WMoVCrTa of Φ3×6 mm produced by arc melting

3.6 Characterization techniques and machine specifications

The as-milled powders and alloy samples were characterized by different techniques listed by the following sub sections. The machines used for the characterization along with their specifications are described in each sub sections below.

3.6.1 Particle size analysis

Particle size distribution of the milled powders after different milling time was measured by particle size analyzer (PSA) (Make: Malvern, Model: Master sizer 2000) using LASER diffraction technique, via water as dispersant. The PSA works on the principle that when a beam of light (LASER) is scattered by a group of particles, the angle of light scattering is inversely proportional to the particle size.

3.6.2 X-ray Diffractometry

The crystal structure and various phases present in the as-milled powders as well as in heat treated alloys were analyzed by an X-ray diffractometer (Make: Rigaku, model: TTRAX-IIIXRD) operating at 50 KV/100mA with Cu-kα radiation (λ=1.540Å). The X-Ray scan was carried out with a 2θ in the range 20° to 100° with a step size 0.03° and at scan rate of

0.067°/second. The heat treated alloys were finely polished by auto polishing machine (BUEHLER, AUTOMET 250 MODEL: 60-7230) with polishing papers of grit size up to 600 and then cloth polished using fine Alumina powders. The polished and unetched alloy samples were delicately cleaned by ultrasonication and those dry samples were taken for X-ray scan. The possible phases present in the milled powder and heat treated alloys were determined by comparing the peak position and intensity with powder diffraction files (PDF).

3.6.3 Light microscopy

Preliminary determination of number of phases present and their area percentages in the unetched heat treated alloys after polishing were carried out by an upright Light microscope (Make: Carl Zeiss, Model: Axiotech) under monochromatic light. The digital images were captured and analyzed for determination of phase percentage by Axio Vision Rel.4.2 software.

3.6.4 Field emission scanning electron microscopy

The morphology of the milled powders, the microstructure of the unetched alloy ingots after polishing, the fractured surface of the heat-treated alloy after compression test were analyzed using field emission scanning electron microscope (SEM) [zeiss, sigma]. Images were obtained by secondary electron (SE2) detector and back scattered electron detector (BSD). The chemical composition of the milled powders and heat-treated alloys were determined by an energy dispersive X-ray spectroscope EDS (Make: Oxford, Model: INCA X-Sight) attached with SEM. High purity Cobalt was used for the standard reference for quantitative analysis of the constituent phases. X-ray elemental mapping technique was used to determine the qualitative distribution of different elements in milled powders and heat treated alloys.

3.6.5 Field emission transmission electron microscopy

The crystal structure of the mechanically alloyed powder was also investigated by TEM analysis (Make: JEOL, Model: JEM-2100F), operated at 200 kV. The milled powder was sonicated thoroughly by adding with acetone as solvent and a drop of the solution was poured on a 400

mesh carbon coated copper grit for observation and the grit was placed in the sample holder of TEM. The selective area electron diffraction (SAED) pattern was obtained for identifying the crystal structure of the milled powders. Inter-planar spacings of the crystals were determined from the HRTEM images.

3.6.6 Compression Test

The alloy ingots were cut by WEDM to prepare cylindrical compression test samples of Φ3×6 mm. Uniaxial compression tests of samples were carried out by a Universal Testing Machine (model: MEDIAN 250 make: BISS) both at room and high temperature (up to 1000°C) with a constant cross head velocity of strain rate as 0.1 mm/min. Engineering stress-stain curve was obtained from the test results.

3.6.7 Hardness Test

The polished alloy samples were analyzed for hardness using a Vickers hardness tester (make: Omni Tech) with a diamond indenter (136° included angle). The constant load of 500 gram was applied for a time period of 15 seconds. The Vickers hardness (HV) was determined using the following relation.

$$HV = 1.854F/D^2 \tag{17}$$

where D is the arithmetic mean of the two diagonal lengths of the indentation in mm and F is the load applied in kilogram. The hardness values of the alloys were obtained by taking average of minimum 10 individual trials.

3.6.8 Density

Density of the alloy was determined by Archimedes principle using water as medium. According to the Archimedes principle,

$$\frac{weight\ of\ the\ sample}{weight\ of\ water\ displaced} = \frac{density\ of\ the\ sample}{density\ of\ the\ water} \tag{18}$$

$$Weight\ of\ water\ displaced = weight\ of\ object\ in\ vacuum - weight\ of\ object\ in\ water \tag{19}$$

3.6.9 Tribological Test

Wear test was carried out for the three HEAs by Pin on Disk wear tester to determine the tribological properties of the alloys and to compare them with that of HSS. The alloys were worn at different loads and their tribological properties such as wear coefficient and coefficient of friction (COF) were determined on varying sliding distance. The HSS rod of model no: DWAMM53202 was supplied by DEWALT (R), Brazil. The cylindrical pin samples of diameter 3 mm and length 8 mm were prepared from the above three materials by Wire-Cut Electro Discharge Machine. The pins were machined to very small diameter of 3 mm to minimize the uneven contact of their surface during the wear test. Moreover, to flatten the surface, the pins were initially grinded by auto polishing machine [Automet, Buehler] using SiC abrasives of grit sizes 180, 400 and 600. The grinded samples were finely polished by cloth using fine Alumina powder suspended in water. The polished samples were sonicated with Ethanol for 30 minutes and dried properly. The wear test of the pins was carried out by a Pin on Disk wear tester [TR-201, Duocom] against the 320 grit SiC [Carbimet, Buehler] abrasive disk. The SiC was selected as abrasive to wear the RHEAs due to its higher hardness (Mohr's hardness 9) than that of pure Tungsten (Mohr's hardness 7.5). The Tungsten carbide (WC) was not preferred as abrasive for RHEAs in order to avoid or reduce any material transfer or tribo-chemical reactions [113]. The SiC abrasive was also chosen to wear the 3d-HEA with the purpose of studying the tribological behavior of the HEA under most severe conditions [136]. The disk was rotated at a speed of 50 RPM. The relative speed of 0.13 m/s between the pin and the disk was maintained throughout the experiments. The wear tests were carried out for each pin with the constant loads of 30N and 40 N acting perpendicularly to the counter surface. Wear tests were conducted at room temperature under dry conditions. Wear volume after regular sliding intervals of 50 meters were determined by measuring the weight loss of the pins using a precision balance (accuracy = 0.0001 gram). Wear coefficient (W) was determined by the formula:

$$W = \frac{\Delta V}{F \times x} \tag{20}$$

where, W is in mm^3 / N m, ΔV is the Wear volume (mm^3), F is the normal load (N) and x is the sliding distance (m) [135].

The tangential frictional force (N) was determined by continuously grinding the pins against the disk up to 300 meters at both 30 and 40 N loads and recorded by Winducom software available with the wear tester. Each experiment for wear as well as frictional force determination was repeated for three times to ensure the accuracy of the results. The wear debris were also collected for analysis. The microscopic analysis of the worn surface and the debris were obtained by Field-emission scanning electron microscope (SEM) (Zeiss, Sigma) attached with an Energy-dispersive X-ray spectroscope (EDS). The phase analysis of the debris was carried out by an X-ray diffractometer [TTRAX-IIIXRD, Rigaku, Japan] operated at 50 kV/100 mA using Cu-kα radiation (λ = 1.540 Å). Topography of the worn surface was carried out using a high precision optical surface Profilometer (Taylor Hobson, Talysurf CCI lite).

Chapter 4

Results and Discussion

4.1 Introduction

The present chapter detailed the results of the investigation as per the experiments mentioned in Chapter 3. The alloy design parameters, extent of alloying during ball milling of the powder mixtures, microstructural characterization, mechanical and tribological properties of the sintered and the arc melted HEAs are presented and discussed in the following sub-sections.

4.2 Design parameters of HEAs

The Guo et al.'s design parameter values for the equiatomic HEA powder combination of WMoVCrTa were calculated. Corresponding results are depicted in Table 4.1. The calculated values are in agreement with that proposed by Guo et al. for the formation of solid solution phases by inhibiting the formation of BMGs [6].

Table 4. 1 Thermodynamic and other design parameters for WMoVCrTa HEA

Design Parameters	ΔH_{mix} (kJ/mol)	T_m (K)	ΔS_{mix} (kJ/mol.K)	ΔG_{mix} (kJ/mol)	δ	VEC
Values	-3.52	2849	0.01338	-41.64	5.025	5.60

The Takeuchi et al's mismatch entropy parameters for WMoVCrTa, $W_{23}Mo_{23}V_{17}Cr_8Ta_7Fe_{22}$ and $(Al)_{10}(FeCoNiCu)_{90}$ are 0.1992, 0.032, and 0.0998 respectively. These values are quite small that indicates the probability of BMG formation is less in the corresponding HEAs [32].

4.3 Mechanically alloyed WMoVCrTa powder

The powder mixture of WMoVCrTa was mechanically alloyed up to 64 hours by ball milling route to know the extent of alloying. Microstructural characterization and Crystal structure

determination of the milled powders were carried out by different techniques and the results are presented and discussed in the subsequent sections.

4.3.1 Particle size analysis

The variation of particle size of the powder mixture milled for various hours was analyzed by particle size analyzer and is shown in Table 4.2. The median particle size denoted by the symbol d (0.5) indicates the median size of 50% particle volume [114]. This means 50 % of the particles are larger than the value of d (0.5) and 50% are smaller than the corresponding value. The particle size decreased continuously with increase in milling time till 32 hours due to fragmentation of powder particles. In milling process, fragmentation and cold welding of powder particles occur simultaneously. The d (0.5) values of 4, 8 and 64 hours milled powders were obtained from the cumulative particle size distribution curves shown in the Figure 4.1. The particle size decreased marginally till 32 hours of milling. Milling beyond 32 hours showed an increase in the particle size.

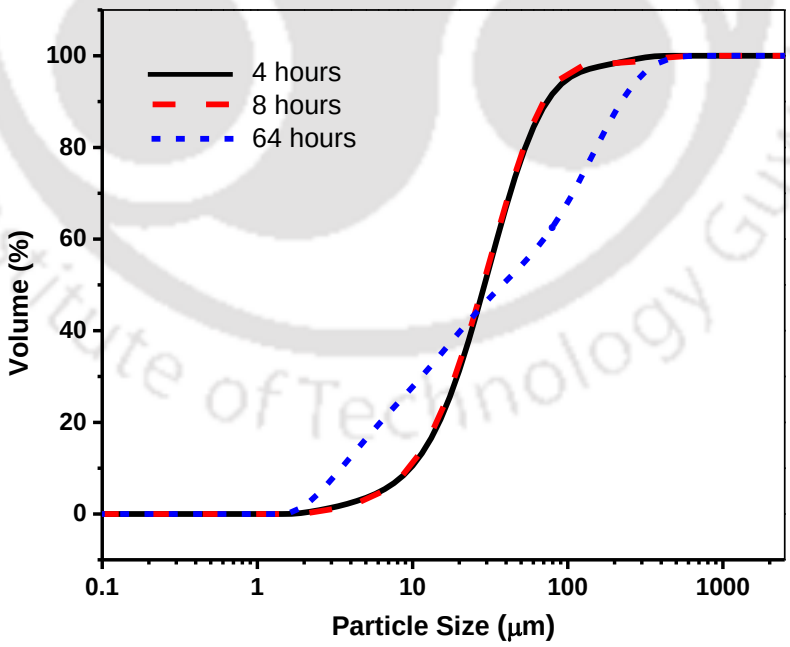

Figure 4. 1 Cumulative Particle size distribution curves of 4, 8 and 64 hours milled WMoVCrTa powder

Table 4. 2 Median particle size (d (0.5)) of the milled powder of WMoVCrTa after different hours.

Mill time (hour)	4	8	16	32	64
d (0.5) in µm	29.1	28.4	27.4	25.1	32.9

4.3.2 SEM and EDX analysis

The SEM micrographs of the powder mixture milled for various time periods are shown in Figure 4.2. The features of the powder mixture milled after 15 minutes show irregular morphology. With subsequent milling, the morphology of the powder mixture changed continuously. The average particle size measurement from the SEM micrographs using Image-J software reveals that the size of the particles decreased continuously with increase in milling time till 32 hours and then increases till 64 hours. This trend is similar to that obtained by the particle size analyzer. Features of particle fracturing during milling for 4 hours are evident as revealed from the micrographs shown in Figure 4.2 (b). During successive milling, plastic deformation of the powder particles occurs resulting in work hardening leading to loss of ductility [30]. The work hardened powder particles fracture due to the impact between the balls. The continuous cold welding and fracturing proceeds till the rate of cold welding and the rate of fracturing attain equilibrium [30]. The micrograph of 8 and 16 hours milled powders show further refinement of powder particles. Milling the powders up to 32 hours results in very fine particles, that can be observed in the micrograph in Figure 4.2 (e). After milling for 64 hours, the features representing agglomeration of the particles were observed in the micrograph (shown by arrow marks in Figure 4.2 (f).

The quantitative analysis of EDS spectra of WMoVCrTa powder milled for 16 and 64 hours are shown in Figure 4.3. Results of the EDS analysis of the powders milled for 16 hrs, and 64 hrs are depicted in Table 4.3. The values presented are the average of five reading.

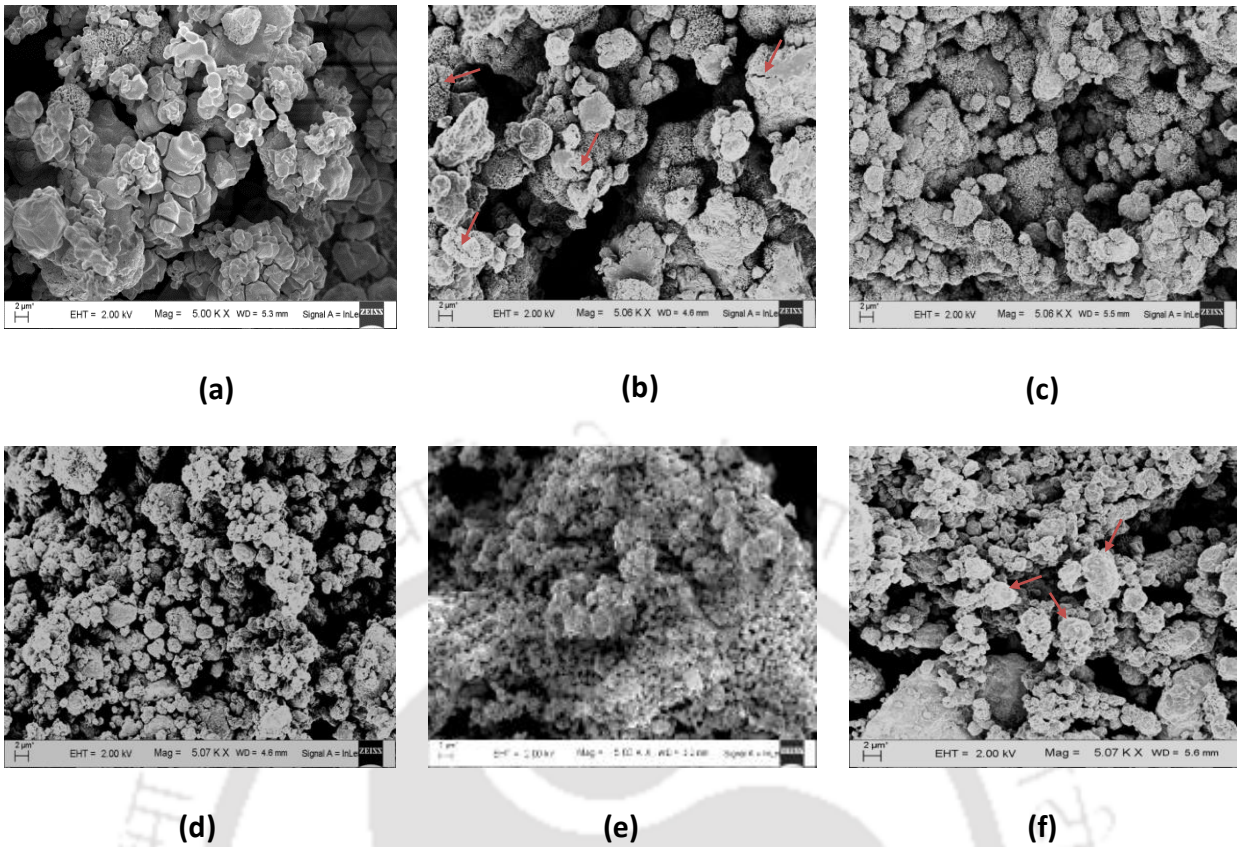

Figure 4. 2. SEM micrographs of WMoVCrTa milled powders after (a) 15 minute, (b) 4 hours, (c) 8hours, (d) 16 hours, (e) 32 hours, and (f) 64 hours

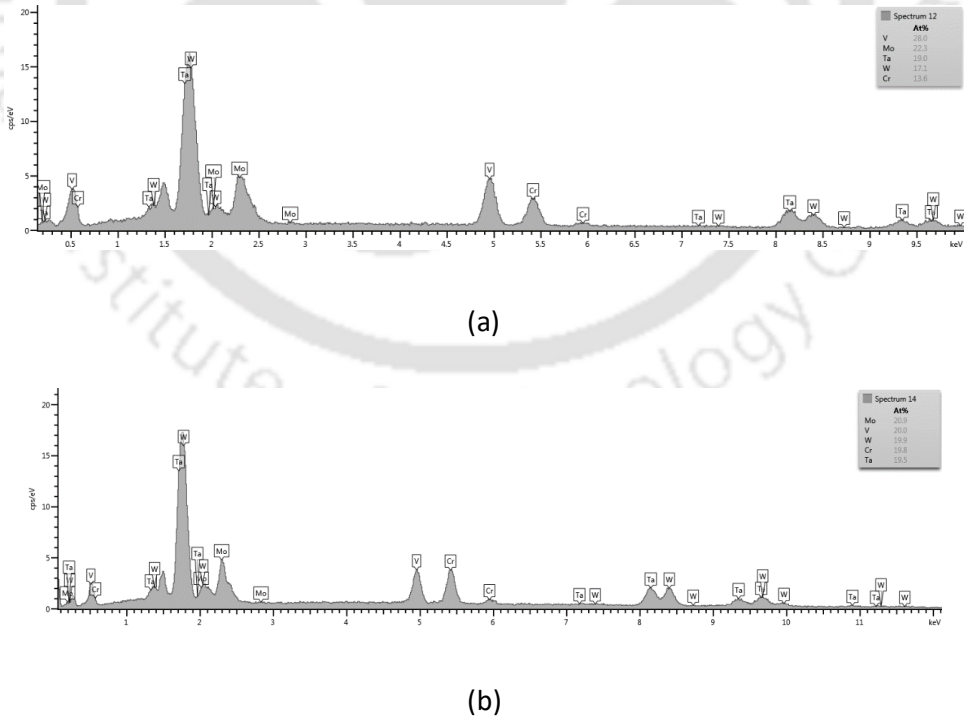

Figure 4. 3. EDS spectra of WMoVCrTa powder milled for (a) 16 hours and (b) 64 hours.

The results indicate that the alloy powder is in near equiatomic ratio after prolonged milling for 64 hours. Figure 4.4 shows the X-ray maps of the constituent elements in the WMoVCrTa alloy powder after milling for 64 hours. The figure indicates homogeneous distribution of individual elements in the 64 hour milled powder mixture.

Table 4. 3. Average atomic percentage of elements in milled WMoVCrTa powders

Mill time (hour)	W (at. %)	Mo (at. %)	V (at. %)	Cr (at. %)	Ta (at. %)
16	17.1 ± 0.7	22.3 ± 0.4	28.0 ± 0.3	13.6 ± 0.5	19.0 ± 0.7
64	19.9 ± 0.4	20.8 ± 0.8	20.0 ± 0.5	19.8 ± 0.4	19.5 ± 0.8

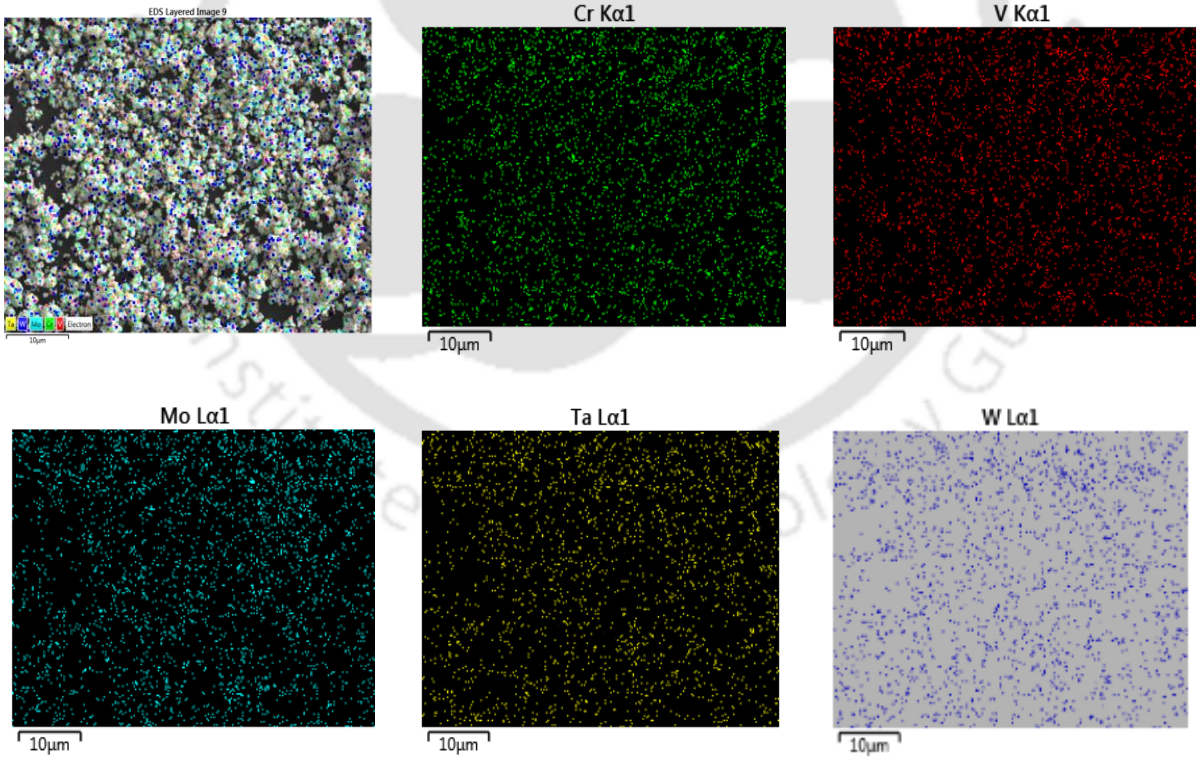

Figure 4. 4. Energy Dispersive Spectroscopy (EDS) map of 64 hours milled WMoVCrTa powder.

4.3.3 XRD analysis

The crystal structure of the WMoVCrTa powder mixtures milled for various hours were analyzed by XRD technique. The diffraction patterns are shown in Figure 4.5. In the XRD pattern of the 15 minutes milled powder mixture, sharp peaks with high intensities were observed corresponding to the reflections from the planes of W, Mo, Cr, and Ta. The peak intensities corresponding to the reflections from the planes of V powder were very weak at the initial milling period. The diffraction peaks from the planes of V could not be detected after milling for 4 hours. With further milling, the intensity of reflections from the planes of W, Mo, Cr, and Ta decreased with simultaneous increase in the peak width. The significant peak broadening and reduction in peak intensity indicate the refinement of crystallite size, change in microstrain and decrease in the crystallinity during milling process [115].

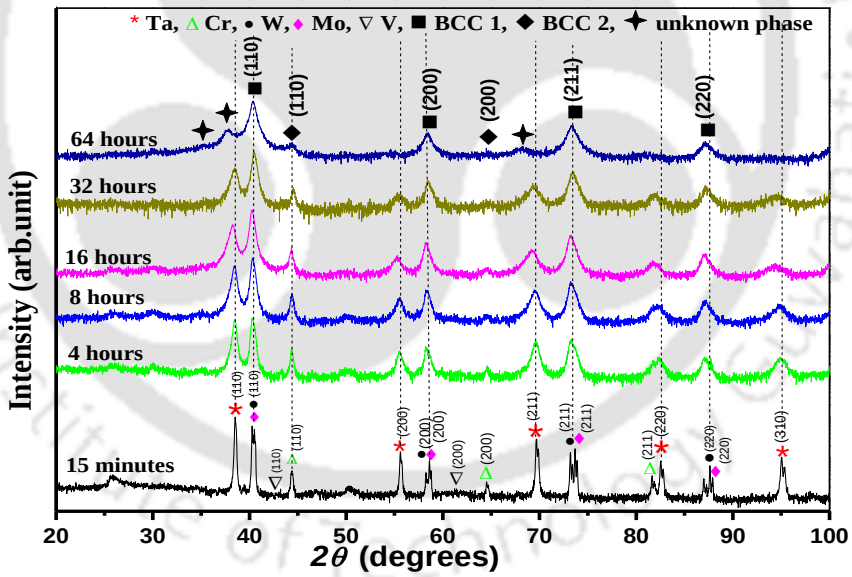

Figure 4. 5. XRD patterns of WMoVCrTa powder mixture for different milling periods.

The XRD analysis of the 64 hours milled powder mixture revealed a major BCC1 phase, a minor BCC 2 phase and an unknown phase (shifted to the left of the pure Ta peaks) shown in Figure 4.5. The four major peaks at 2θ values of 40.36º, 58.44º, 73.34º and 87.06º (close to pure W or Mo peaks) indicate reflections from the mechanically alloyed powder having the body-centered cubic (BCC) structure since this match with the standard BCC pattern and this phase is

henceforth designated as BCC1. Similar BCC phase was also obtained in other HEAs containing W and Mo [9, 116 and 117]. The above mentioned 2θ values corresponds to reflections from the (110), (200), (211) and (220) planes of BCC1 phase, respectively. The respective inter-planar spacing (d values) for these planes are 2.23Å, 1.57Å, 1.28Å and 1.12Å. Lattice parameter of the BCC1 phase is 3.160 Å. Two small intensity peaks (close to pure Cr peaks) were identified as minor BCC2 phase at 2θ values of 44.42º and 64.7º. The inter-planar spacings of this phase were obtained as 2.04Å and 1.44Å for the (110) and (200) planes respectively. Lattice parameter of the BCC2 phase was calculated to be 2.88Å. The small intensity peaks at *2θ* values of 35.2°, 37.8° and 68.3º are of unknown phase which were later confirmed as of Cr_2Ta phase after heat treatment of the ball milled powder.

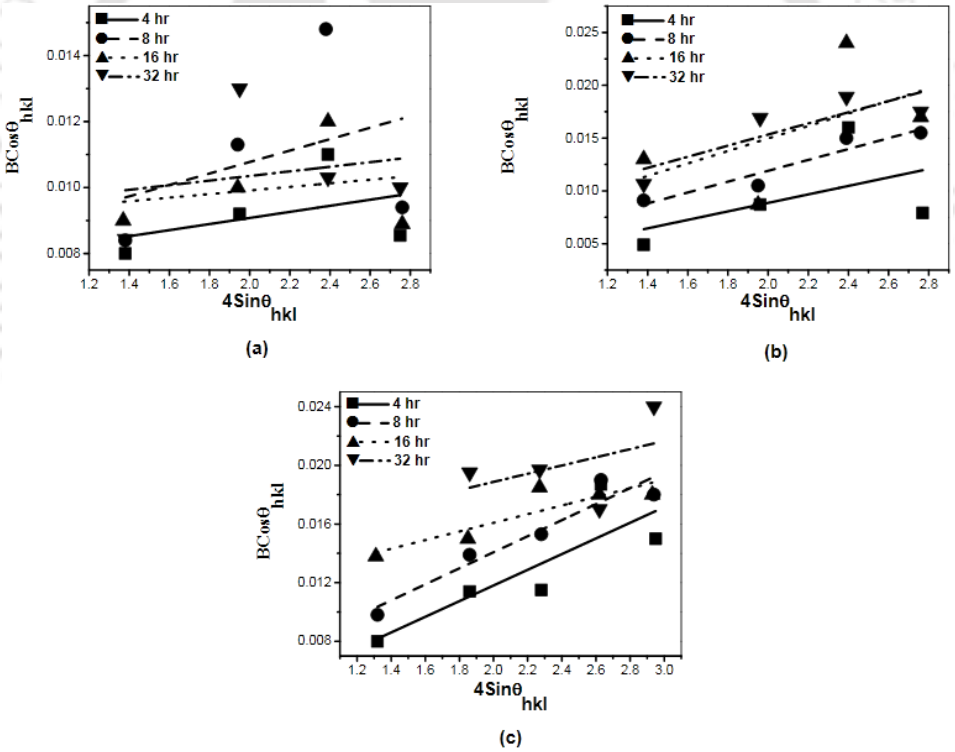

Figure 4. 6. W-H plot of (a) W, (b) Mo, and (c) Ta peaks in WMoVCrTa powder mixture.

The crystallite size and microstrain of W, Mo, and Ta during continuous milling process were determined by analyzing the X-ray peak profiles [118]. Gaussian function was chosen for fitting and separation of overlapping X-ray peak. To analyze the overlapping peaks, multiple (up

to two) Gaussians were used. The full width at half maximum (FWHM) was determined from the fit parameters for different peaks. Figure 4.6 (a), (b), and (c) shows the Williamson-Hall plot for W, Mo, and Ta peaks respectively of the WMoVCrTa powder mixture milled for different periods.

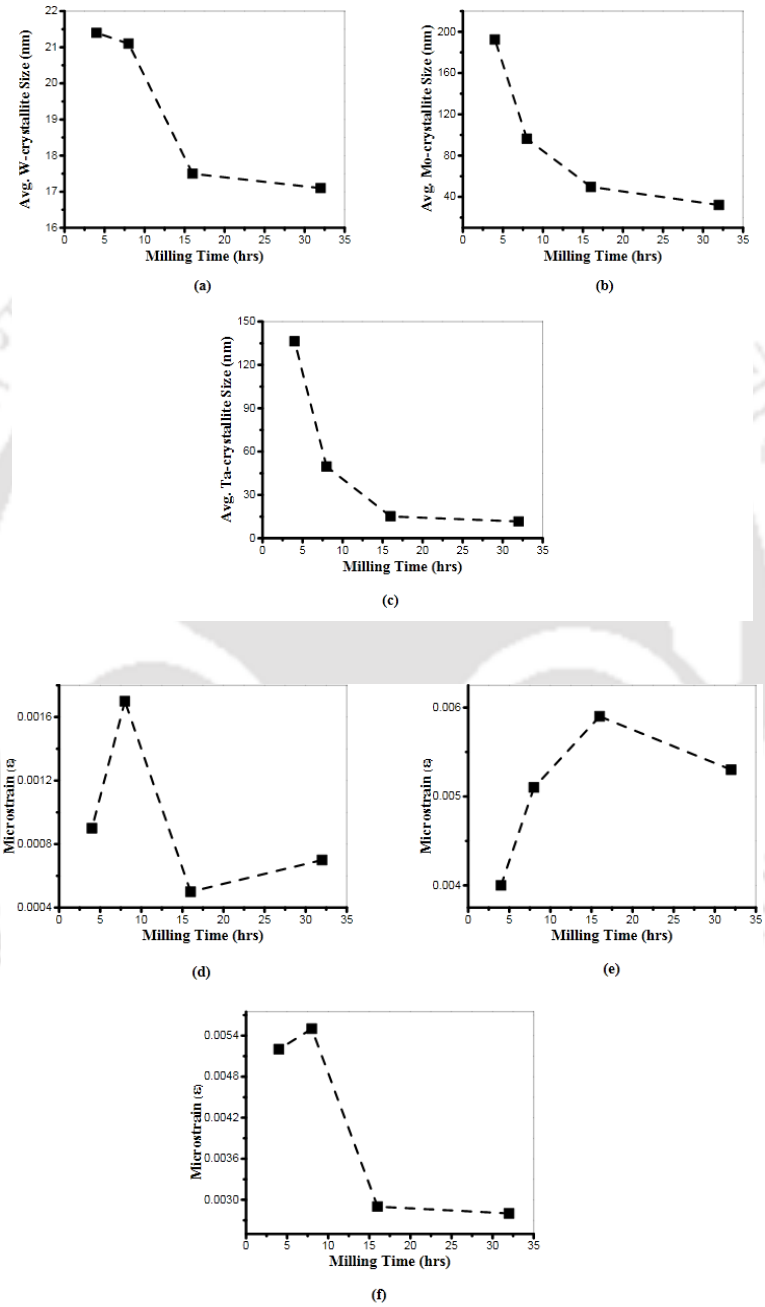

Figure 4. 7. Variation of avg. crystallite sizes with milling time for (a) W, (b) Mo, (c) Ta, and microstrain vs. milling time for (d) W, (e) Mo, (f) Ta in WMoVCrTa milled powder

The variation of average crystallite size as a function of milling time for W, Mo, and Ta is shown in Figure 4.7 (a), (b), and (c) respectively. The variation of microstrain as a function of milling time for W, Mo, and Ta is shown in Figure 4.7 (d), (e), and (f) respectively. The average crystallite sizes of W, Mo, Ta and Cr powders reduced continuously on progressive milling. After 32 hours of milling, the average crystallite sizes of Ta, Mo, and W were determined to be 11 nm, 32 nm and 17 nm respectively. The results indicate the formation of nano-crystalline WMoVCrTa alloy power by mechanical alloying after milling for 64 hours. The microstrains of the W, Mo, and Ta behave randomly on progressive milling as each of them has different mechanical properties.

Figure 4.8 shows the XRD pattern of 64 hours milled WMoVCrTa powder before and after heat treatment at 1000 °C for 20 hours. A major BCC1 and minor BCC2 phases were also identified after heat treatment as labelled in Figure 4.8. The four major peaks at 2θ values of 40.31º, 58.35º, 73.24º and 87.03º indicate reflections from the mechanically alloyed powder having the BCC1 structure. The inter-planar spacings of this phase were obtained as 2.24Å, 1.58Å, 1.29Å and 1.12Å for the (110), (200), (211) and (220) planes respectively. Lattice parameter of BCC1 phase was calculated to be 3.162Å. Two small intensity peaks for BCC2 phase in heat-treated powder were identified at 2θ values of 44.26º and 64.34º. The inter-planar spacing of this phase were obtained as 2.05Å and 1.45Å for the (110) and (200) planes respectively. The lattice parameter of BCC2 phase after heat treatment is 2.9Å. The lattice parameters of BCC phases after heat treatment increased compared to that of the as-milled powders indicating the starting of the alloying. The peak intensity corresponding to the BCC1 and BCC2 phases of the heat-treated powder were also increased than that of the as-milled powder (Figure 4.8).

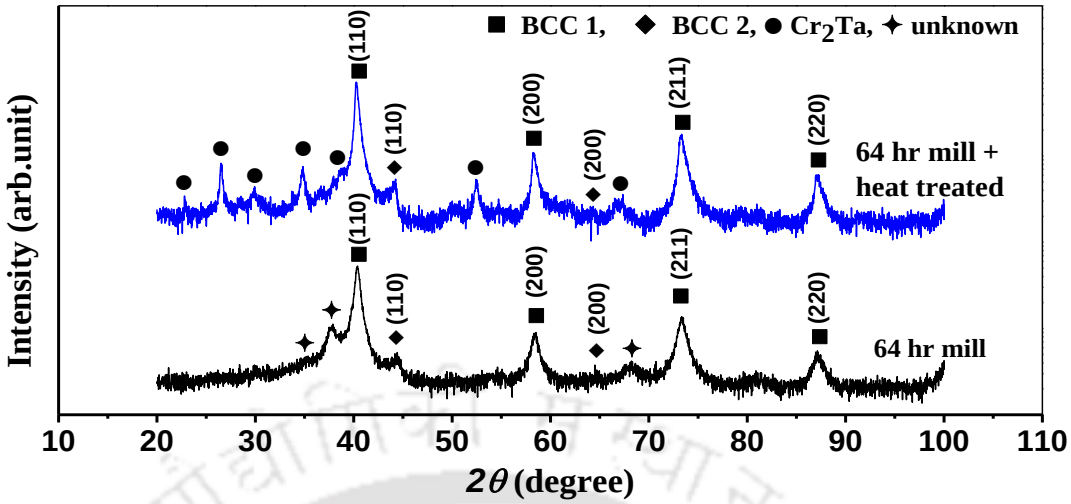

Figure 4. 8. Comparison of the XRD pattern of the 64 hours milled WMoVCrTa powder before and after heat treatment.

In addition to two BCC phases, new small intensity peaks were also evident at 2θ values of 22.87º, 26.54º, 29.86º, 34.83º, 38.9° and 52.5º and 66.9º (Figure 4. 8). Comparing to the Powder Diffraction File (PDF), these peaks were found to be corresponding to the formation of intermetallic compound Cr_2Ta (space group *Fd3m*, lattice constant $a = 11.4500$ Å, PDF Reference code: 00-020-0317).

4.3.4 TEM analysis

Figure 4.9 shows (a), (b), and (c) Bright Field TEM images at different magnifications; (d) HRTEM image of (c); (e) IFFT of (d); (f) line profile of (e) of the 64 hours milled WMoVCrTa powder. Nano particles were seen in the bright field images. The inter-planar (d) spacing measured from the HRTEM image was 2.3Å which confirms that it corresponds to (110) plane of BCC1 phase as the result is coincident with XRD results. Figure 4.10 shows (a) Bright Field TEM image; (b) HRTEM image of the dotted region in (a); (c) IFFT of (b); (d) line profile of (c); (e) SAED pattern of (a), of the 64 hours milled + heat treated WMoVCrTa powder. The inter-planar (d) spacing measured from two HRTEM images (at different locations) was 2.37Å which confirms that it corresponds to (110) plane of BCC1 phase as the result is coincident with

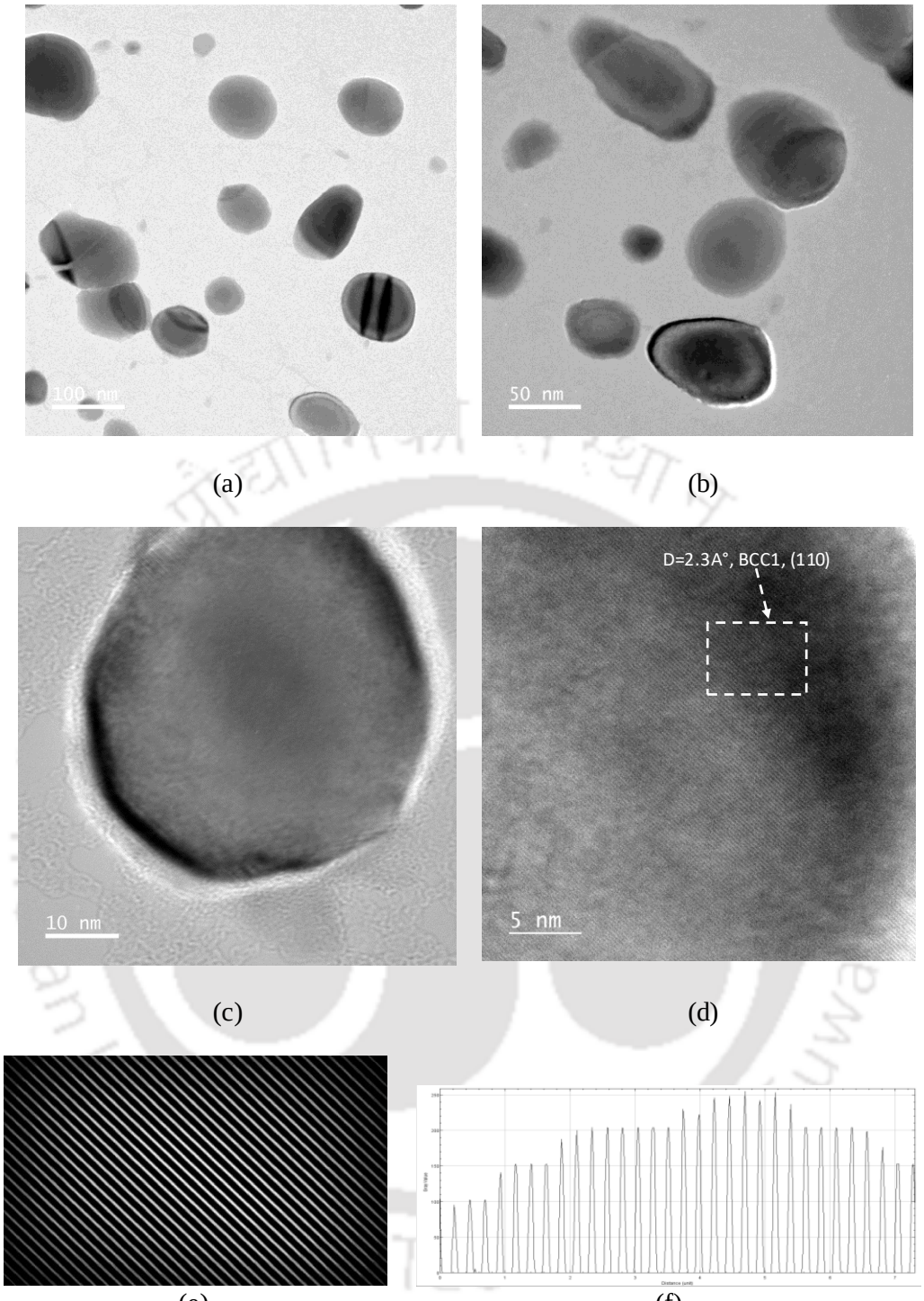

Figure 4. 9. (a), (b), and (c) Bright Field TEM images; (d) HRTEM image of (c); (e) IFFT of (d); (f) line profile of (e) of the 64 hours milled WMoVCrTa powder.

XRD results. The concentric rings with bright spots were found in the SAED pattern suggesting the alloy powder of WMoVCrTa is polycrystalline [119]. Image J software was utilized to measure the radius of the rings for indexing the concentric SAED ring patterns. A BCC phase

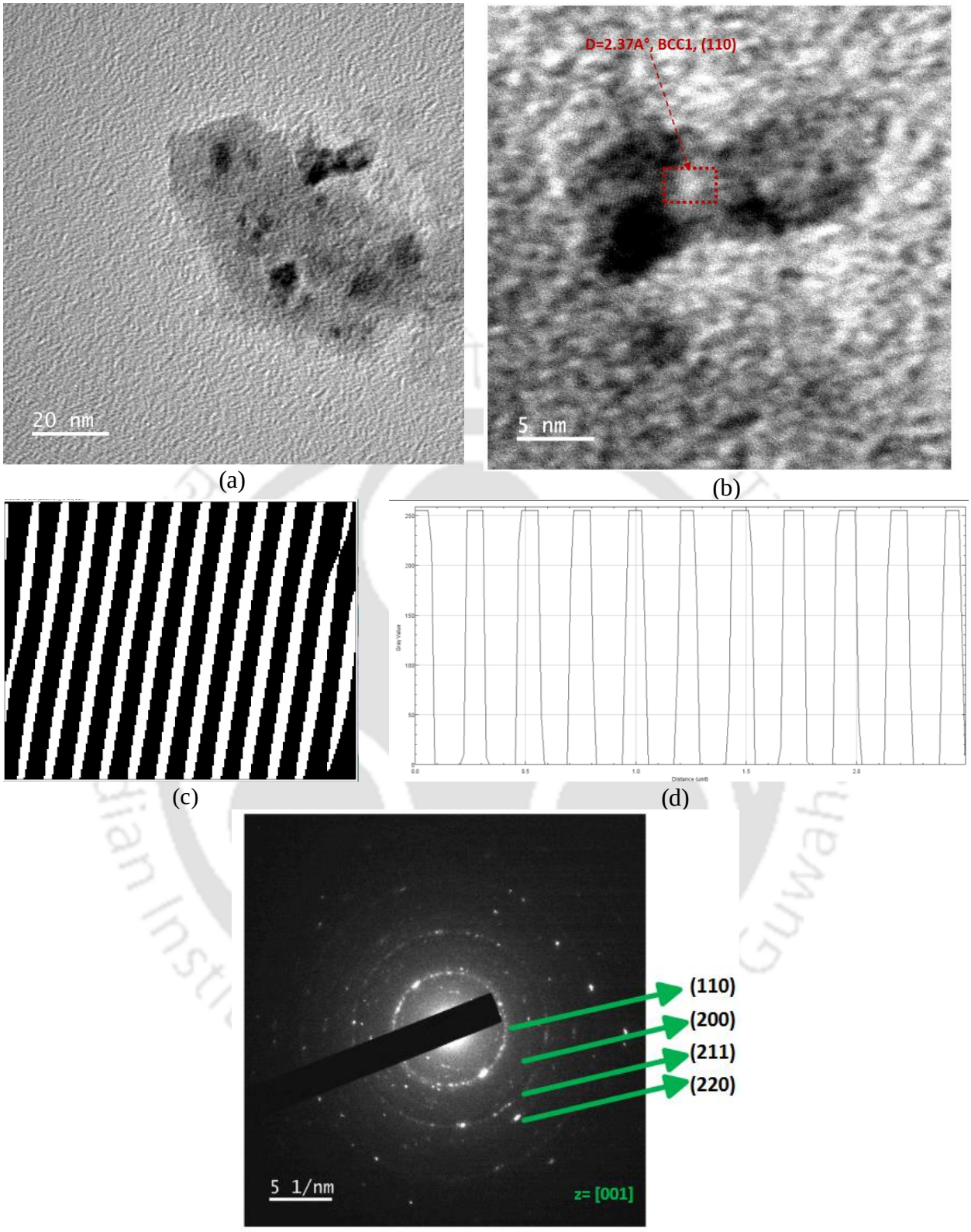

Figure 4. 10. (a) Bright Field TEM image; (b) HRTEM image of the dotted region in (a); (c) IFFT of (b); (d) line profile of (c); (e) SAED pattern of (a) of the 64 hours milled + heat treated WMoVCrTa powder

was confirmed from the SAED analysis. The rings were indexed as corresponding to the (110), (200), (211) and (220) planes of the BCC lattice. The inter-planar spacings of (110), (200), (211) and (220) planes are 2.22Å, 1.605Å, 1.298Å and 1.121Å respectively. The corresponding values of the d-spacings for the (110), (200), (211) and (220) planes of the BCC1 phase obtained from XRD analysis were 2.24Å, 1.583Å, 1.29Å, 1.12Å. This confirms that the SAED pattern of Figure 4.9 (b) corresponds to BCC1 phase having a lattice parameter of 3.170Å after 64 hours of milling + heat treatment. The lattice parameter obtained for the BCC1 phase by the XRD technique for the same conditions is 3.162 Å. Since the deviation in the lattice parameter determined by the two methods is only 0.3%, the lattice parameter obtained from the SAED analysis is acceptable.

4.4 Arc melted WMoVCrTa alloy

The alloy powder of WMoVCrTa was consolidated by cold compaction and subsequent arc melting to fabricate the alloy ingots. The following section shows the characterization of such ingots by illustrating their structure (crystal structure and microstructure) and properties (mechanical and tribological) investigated by various techniques.

4.4.1 SEM and EDX analysis

The metallographically polished surfaces of the arc melted alloy ingots were observed under Light microscope. The corresponding optical micrograph shown in Figure 4.11 reveals three distinct regions: (i) dendritic phase (Phase-A); (ii) inter-dendritic region (Phase-C) and (iii) black round phases (Phase-B). The micrograph indicates phase-B located inside the inter-dendritic region. It is to be noted that in TiZrNbMoV HEA the Laves phases located similarly inside the interdendritic regions [117]. The area percentages of 3 phases estimated by Axio vision software (average values calculated by taking results from 10 different micrographs) are 86%, 4% and 9% for phase A, B and C respectively. Thus, phase B and C are only minor phases in the alloy.

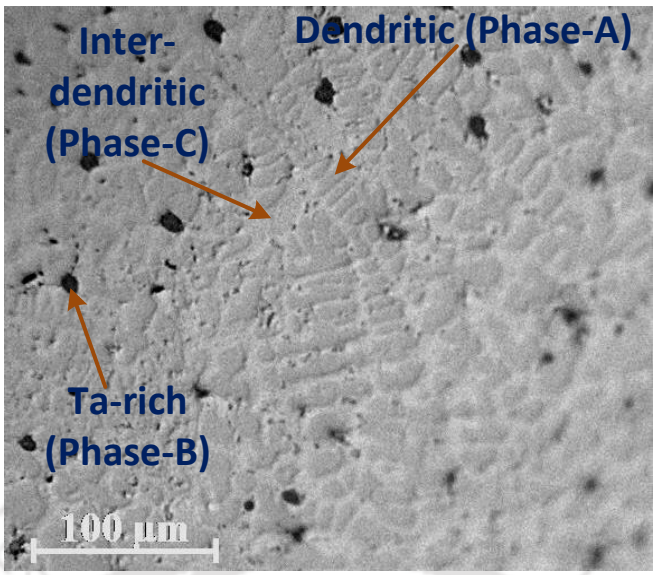

Figure 4. 11. Optical micrograph of the polished WMoVCrTa alloy.

SEM micrographs in HDBSD (High definition backscattered electron detector) mode are shown in Figure 4.12 (a) and (b). Segregation of phase B inside phase C and small pores were clearly visible in Figure 4.12 (a). White dendritic phase (Phase-A) along with phase C and phase B is shown in Figure 4.12 (b).

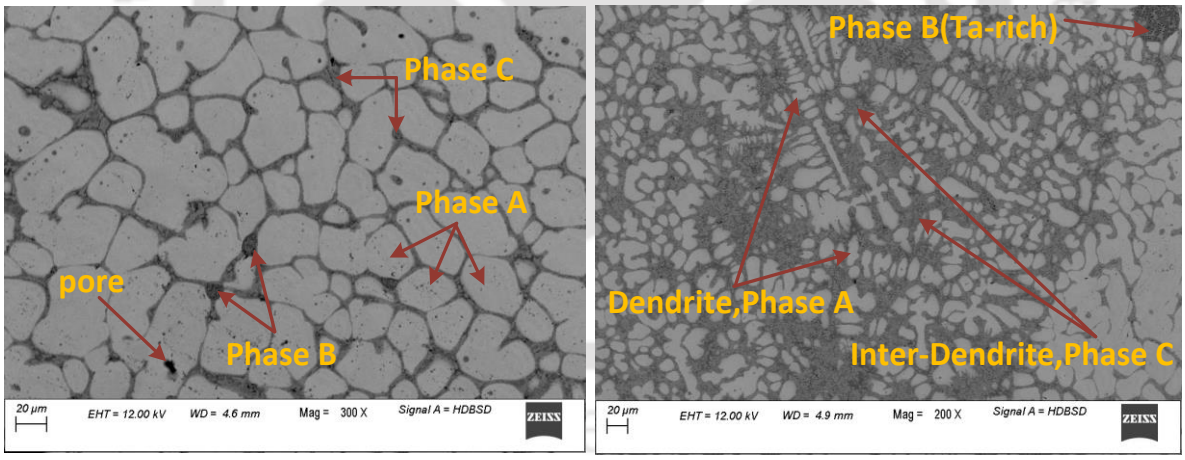

Figure 4. 12. SEM micrographs (HDBSD mode) of WMoVCrTa alloy in (a) 300x and (b) 200x magnifications.

Figure 4.13 Figure 4. shows the SEM micrograph of the region where the EDS analysis for phase-A, phase-B and phase-C were carried out. The average chemical composition of three phases obtained by EDS analysis are shown in Table 4.4. Phase A contains W and Mo as major

elements and is identified as $W_{38}Mo_{35}V_9Cr_6Ta_{12}$. W and Mo have nearly equal atomic sizes and good chemical affinity therefore can undergo substitutional solid solution easily, leading to phase A rich in W with Mo. The interdendritic Phase C is identified as $W_9Mo_{24}V_{21}Cr_{28}Ta_{18}$. The phase B that is located inside the interdendritic phase is identified as $W_4Mo_3V_{20}Cr_{19}Ta_{54}$ and is mainly formed due to the segregation due to excess of Ta. Ta has the largest atomic radii among all the constituent elements in the alloy and the excess of it results in segregation during solidification.

Table 4. 4. Chemical composition of various phases in WMoVCrTa alloy.

Elements	W (at%)	Mo (at%)	V (at%)	Cr (at%)	Ta (at%)
Phase A (BCC1)	38 ± 0.8	35± 0.7	9± 0.9	6± 0.8	12± 0.7
Phase B (laves)	4± 0.5	3± 0.4	20± 0.8	19± 0. 9	54± 0.8
Phase C (BCC2)	9± 0.4	24± 0.4	21± 0.5	28± 0.9	18± 0.9

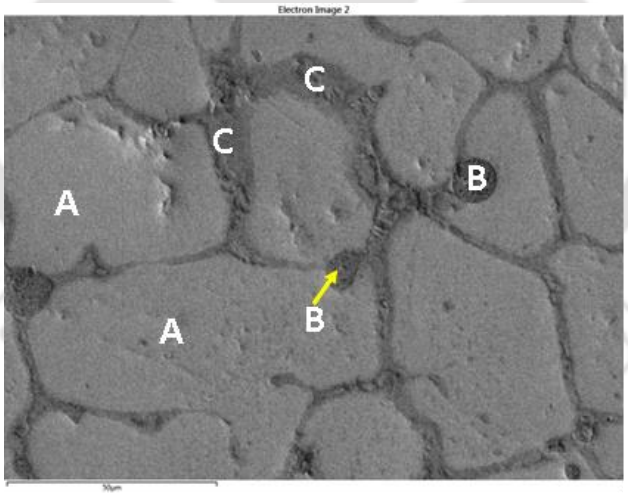

Figure 4. 13. SEM micrograph of WMoVCrTa alloy

4.4.2 XRD analysis

Figure 4.14 shows the XRD patterns obtained for the 64 hours milled powder mixture and arc melted (AM) WMoVCrTa alloy. Analysis of the pattern for the AM alloy reveals three phases: (i) a major BCC1 phase, (ii) a minor BCC2 and (iii) a minor Ta-rich intermetallic phase.

The reflections from the planes corresponding to (110), (200), (211) and (220) of the BCC1 lattice are shown in Figure 4.14. The peaks corresponding to the BCC1 phase of the AM alloy was found shifted to the right compared to that found in the 64 hours milled powder mixture. The peak shift indicates contraction of the BCC1 lattice after melting and the fast cooling. Analysis reveals the lattice parameter of the BCC1 phase in the alloy ingot as 3.05 Å; whereas the lattice parameter of the same phase in 64 hours ball milled powder is 3.16 Å. This confirms lattice contraction during the solidification processing technique. Lattice contraction can occur due to the depletion of large Ta atoms in BCC1 phase shown in Table 4.4. Comparison of the XRD and SEM (section 4.4.1) results reveal that the BCC1 phase corresponds to Phase A in the alloy.

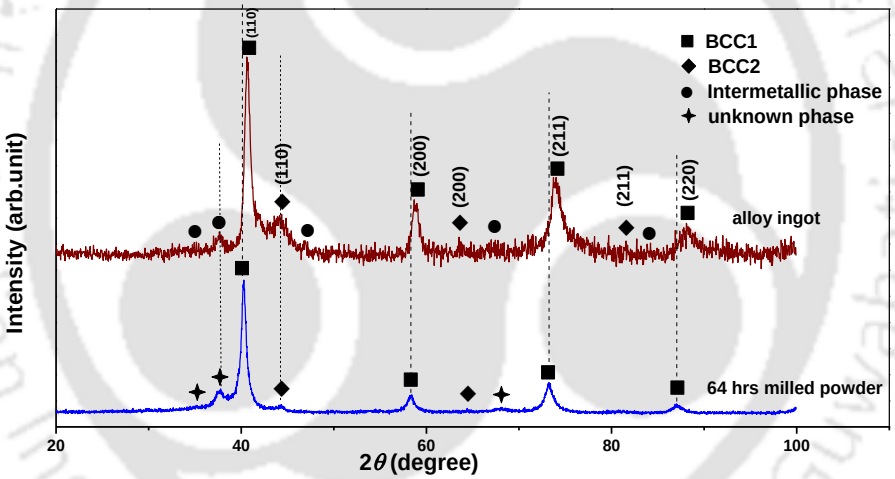

Figure 4. 14. XRD patterns of 64 hours milled powder of WMoVCrTa, and the cast alloy.

Three small intensity peaks in the XRD pattern of the alloy ingot at 2θ values of 44°, 63° and 80° can be seen. This corresponds to the reflection from (110), (200) and (211) of the BCC2 phase [23]. It may also be noted that these reflections are same as that of the reflections from the BCC2 phase of milled powder mixture without any peak shifts. The lattice parameter of BCC2 is 2.85 Å and corresponds to the phase-C of the SEM image (Figure 4.12).

Very small intensity peaks were observed at 2θ values of 34.9°, 37.7°, 46.9°, 67.6° and 84.2°. These patterns could not be indexed with reflections from the existing PDF data files.

Hence the crystal structure for this phase could not be identified from the composition analysis. It is presumed that this is the inter-metallic phase-B (Figure 4.12) having a composition $W_4Mo_3V_{20}Cr_{19}Ta_{54}$ (Table 4.4).

4.4.3 Mechanical properties

Engineering stress vs. engineering strain plots of WMoVCrTa RHEA at various temperatures were obtained from the uniaxial compression test data. The typical engineering stress-strain plots of WMoVCrTa alloy at room temperature, 1000 °C, and 1200 °C are shown in Figure 4.15. The curve at room temperature indicates that the HEA is purely elastic in nature and fails abruptly at 6.2 ± 0.26% strain. Hence the yield stress and ultimate stress of the material are equal.

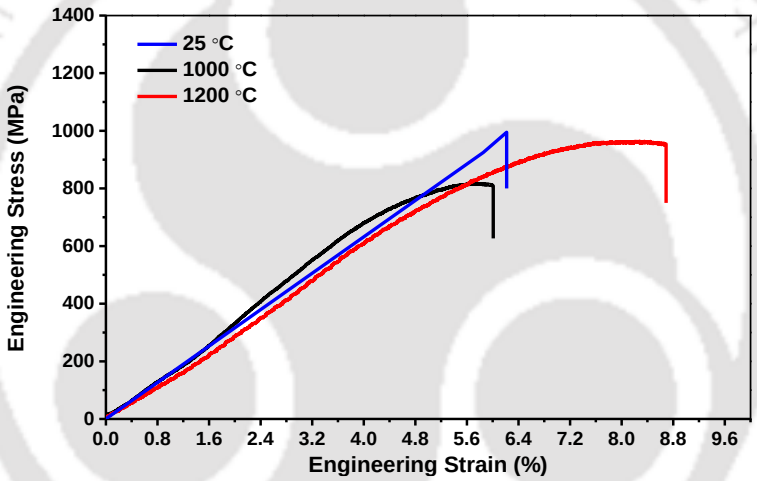

Figure 4. 15. Compressive engineering stress-strain curves of equiatomic WMoVCrTa alloy at different temperatures.

The results of the compression test of the RHEA at various temperatures are summarized in Table 4.5. The room temperature ultimate strength for this material is 995 ± 16 MPa. At 1000 °C, the yield stress (0.2% offset stress) is 785 ± 31 MPa at a strain of 5.06 ± 0.19% and the ultimate stress is 818 ± 26 MPa at a strain of 5.7 ± 0.24%. At 1200 °C, the yield stress increased to 941 ± 26 MPa at a strain of 7.25 ± 0.22% and the ultimate stress to 964 ± 21 MPa at a strain of 8.3 ± 0.18%. From the results in Table 4.5, the yield stress anomaly (YSA) is evident between 1000 °C to 1200 °C [120]. The YSA has also been reported for HEAs by other researchers [121,122,123]. The RHEA of $AlNbTiVZr_{0.5}$ shows the YSA between the temperatures of 600-

700°C [121]. The HEA of ZrNbTiVHf shows the YSA between 500-800°C [122]. The ternary alloy of $Ti_{50}Mo_{25}Al_{25}$ also shows the YSA between 1073-1273K [123]. Yield strain of WMoVCrTa alloy also increased by ~43% on increasing deformation temperature from 1000 °C to 1200 °C.

Table 4. 5 Results of compression test of WMoVCrTa RHEA.

Test Temp. (°C)	Yield stress (MPa)	Yield strain (%)	Ultimate stress (MPa)	Ultimate strain (%)
25	995 ± 16	6.20 ± 0.26	995 ± 16	6.20 ± 0.26
1000	785 ± 31	5.06 ± 0.19	818 ± 26	5.70 ± 0.24
1200	941 ± 26	7.25 ± 0.22	964 ± 21	8.30 ± 0.18

The following key points are to be noted: (i) Assuming the YS is the same as the UTS at room temperature, 78.9 % and 94.6% of the room temperature yield strength of the RHEA is retained at 1000 °C and 1200 °C, respectively, (ii) 82.2% and 96.9% of the room temperature UTS of the alloy is retained at 1000 °C and 1200 °C, respectively and (iii) an yield strength anomaly exists for this RHEA. The high compressive strength in the RHEA is attributed to the solid solution strengthening effect. Though the compressive stress of the alloy is lesser than other refractory HEAs, it is compensated by greater peak strain (6.2%) compared to other reported HEAs systems at room temperature [9, 28 and 29]. The peak strains of NbMoTaW and VNbMoTaW at room temperature were only 1.5% and 0.5% respectively [9]. The peak strains of NbNiTiCoZr and NbNiTiCoZrHf at room temperature were less than 0.5% [28]. The peak strain of HfMoTaTiZr at room temperature was 3% [29].

SEM fractograph of the failure surface of the sample tested at room temperature is shown in Figure 4.16. The fractograph indicates failure by shear as evidenced by the shear lines which was aligned almost 45° to the load axis.

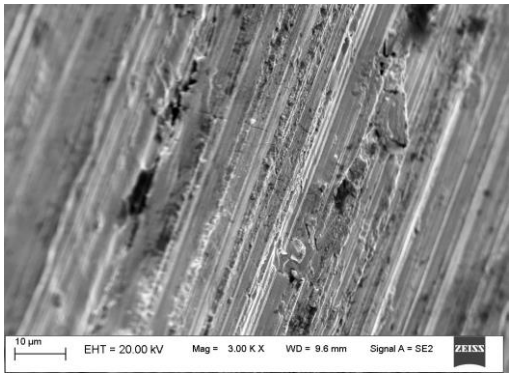

Figure 4. 16. SEM micrograph of the fracture surface of the alloy at room temperature.

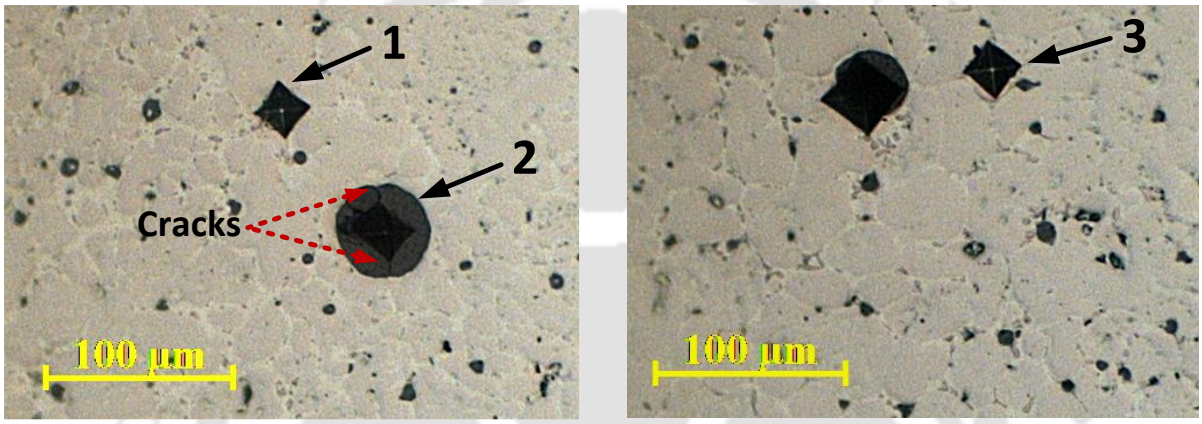

(a) (b)

Figure 4. 17. Top view of the hardness indents in (a) phase C and B (marked as 1 and 2 respectively) and (b) phase A (marked as 3).

The hardness of the ingot sample was obtained by taking the average of 10 readings with a load of 500 gram for 15 seconds. The micrographs of the indentation carried out on phases A, B and C of the alloy are shown in Figure 4. 17. Crack initiation during the indentation was not observed when tested on phase-A and Phase-C (Figure 4.17) indicating these materials exhibit good ductility or toughness. However when indentation was carried out on Phase-B, crack propagation from the corner of the indentation was observed (marked as 2 in Figure 4.17 (a)) indicating that phase-B is very brittle in nature. The measured hardness values for individual phases in the alloy are shown in Table 4.6. The hardness of phase A (BCC1) is highest due to the

presence of high atomic percentage of hard elements like W and Mo in the phase (Table 4.4). High hardness is also obtained for phase C (BCC2) as all five elements are present in near equi-atomic percentage in this phase. The overall Vickers hardness of the alloy is as 773 ± 20 HV. The high overall hardness is attributed mainly to the primary BCC1 phase present in the alloy [5]. The density of the alloy was found to be 11.52 g/cm^3.

Table 4. 6. Vickers hardness of the alloy ingot

Phases	Vickers Hardness (HV)
A (BCC1)	802 ± 16
B(Ta-rich)	396 ± 52
C (BCC2)	670 ± 32
Overall	773 ± 20

4.4.4 Tribological properties

The plots of wear vs. sliding distance of the WMoVCrTa alloy at 30 N and 40 N loads are shown in Figure 4.18 (a). The wear depth increased almost linearly with the increase in sliding distance at 30 N load. However, at the load of 40N, the wear initially increased almost linearly and then increased drastically from the sliding distance of 150 meters to 300 meters. After 300 meters of sliding, the calculated total wear volume of WMoVCrTa at 40 N is 3.2 times higher than that at 30 N. The wear coefficients of WMoVCrTa at 30 N and 40 N loads are shown in Figure 4.18 (b). The figure indicates that the wear coefficient at 40 N is 2.4 times higher compared to that at 30 N. Figure 4.18 (c) shows the plots of COF vs. sliding distance of the alloy at the loads of 30 N and 40 N. The figure indicates higher COF at higher load. The average values of COF at 30 N and 40 N are 0.20 ± 0.02 and 0.28 ± 0.04 respectively. The COF vs sliding distance curve of 30 N increased at higher rate than that of 40 N.

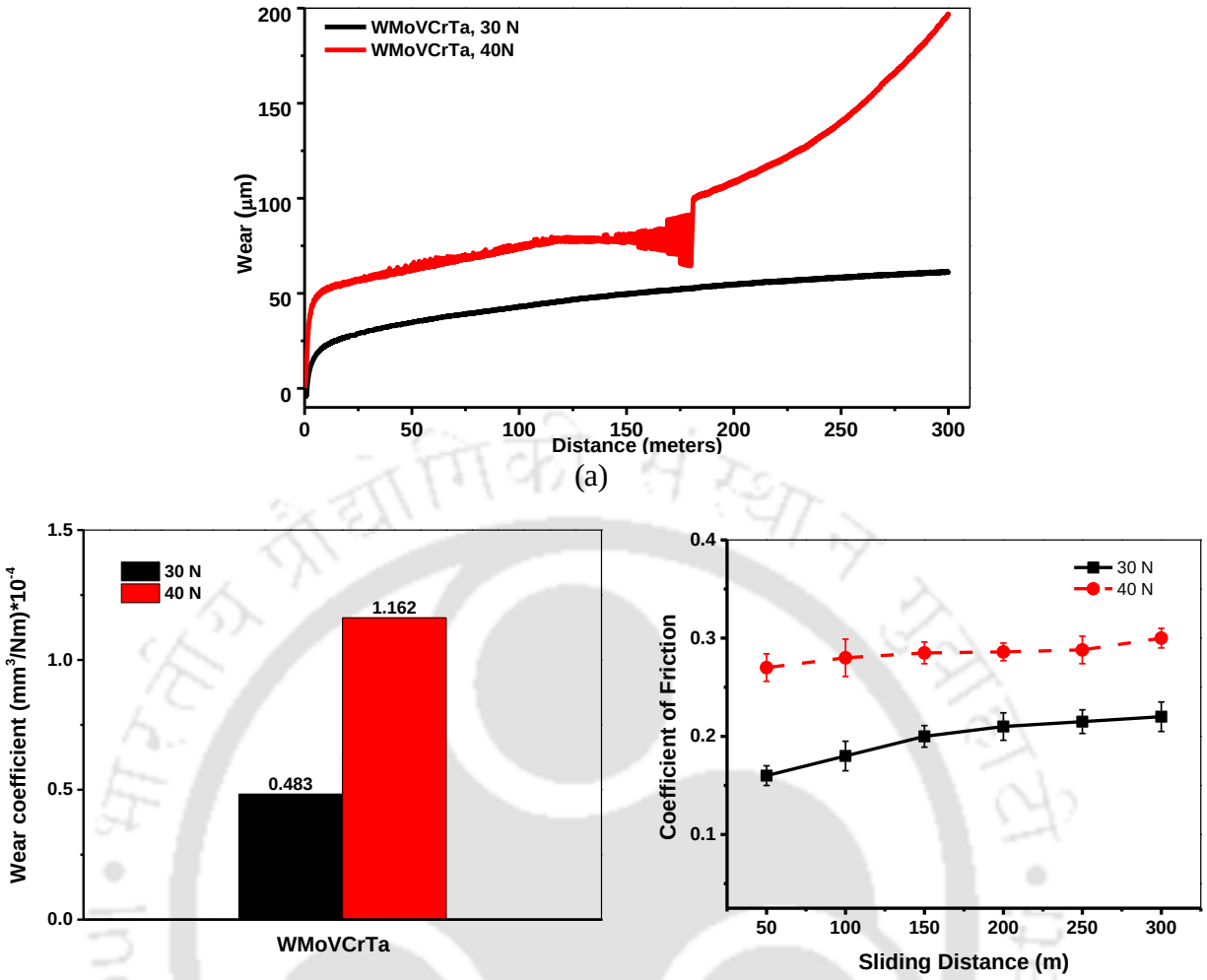

Figure 4. 18 (a) Wear vs. sliding distance, (b) Wear Coefficients and (c) Coefficient of Friction vs. sliding distance plots of the WMoVCrTa RHEA at the loads of 30N and 40 N

SEM image of the worn surface of WMoVCrTa alloy shown in Figure 4.19 reveals wear groove tracks formed due to ploughing action by the abrasives. Cracks and delamination were evident on the worn surface at 40 N load. The wear tracks were not continuous as the alloy has three different phases ($W_{38}Mo_{35}Ta_9Cr_6V_{12}$, $W_4Mo_3V_{20}Cr_{19}Ta_{54}$, and $W_9Mo_{24}V_{21}Cr_{28}Ta_{18}$) each with different hardness values [Table 4.6]. The hardness values for dendritic, Ta-rich and inter-dendritic phases are 802 ± 16 HV, 396 ± 52 HV, and 670 ± 32 HV respectively (Table 4.6). The wear directions are shown by dashed arrows in Figure 4.19

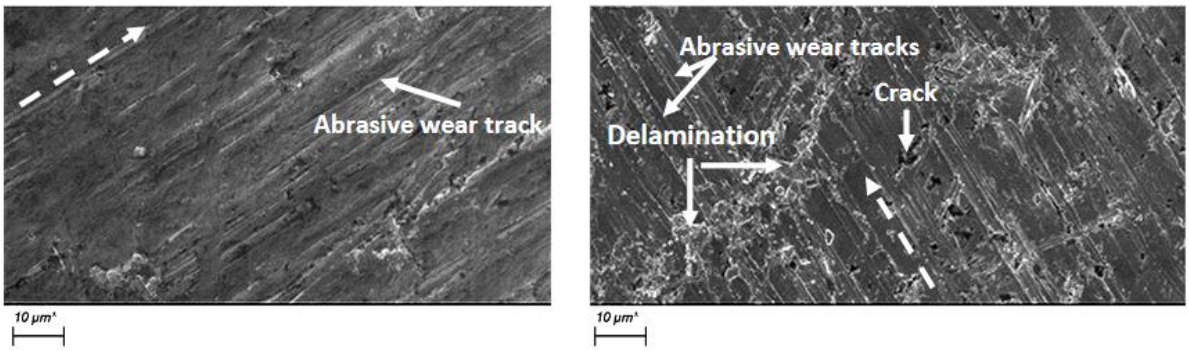

(a) 30 N (b) 40 N

Figure 4. 19. SEM images of the surface of the WMoVCrTa RHEA worn at loads of (a) 30N and (b) 40 N.

The SEM images of the debris collected after the test at different loads are shown in Figure 4.20 (a) and (b). The plate-like long and thin chip was evident and is shown by dotted arrow in the Figure 4.20 (b). The composition analysis results at the numbered regions in the images are shown in Table 4.7. The composition analysis of the debris from location 1 and 2 in Figure 4.20 reveals that they are the debris emerged from the RHEA; whereas the large debris shown at location 3 indicates that they emerged from the SiC abrasives by fracturing abrasive tips during wear test. The atomic percentage of Si in the corresponding large debris is 78% that confirms the debris emerged from the SiC abrasive.

Table 4. 7 Quantitative analysis of the marked regions on the SEM images of the wear surfaces and debris of the RHEA of WMoVCrTa.

Location	W (at. %)	Mo	V	Cr	Ta	Si
1	4 ±0.2	5 ±0.2	23 ±0.7	37 ±0.9	2 ±0.2	29 ±0.5
2	3 ±0.3	4 ±0.2	23 ±0.8	42 ±0.8	2 ±0.3	26 ±0.7
3	0	0	7 ±0.3	15 ±0.7	0	78 ±0.3

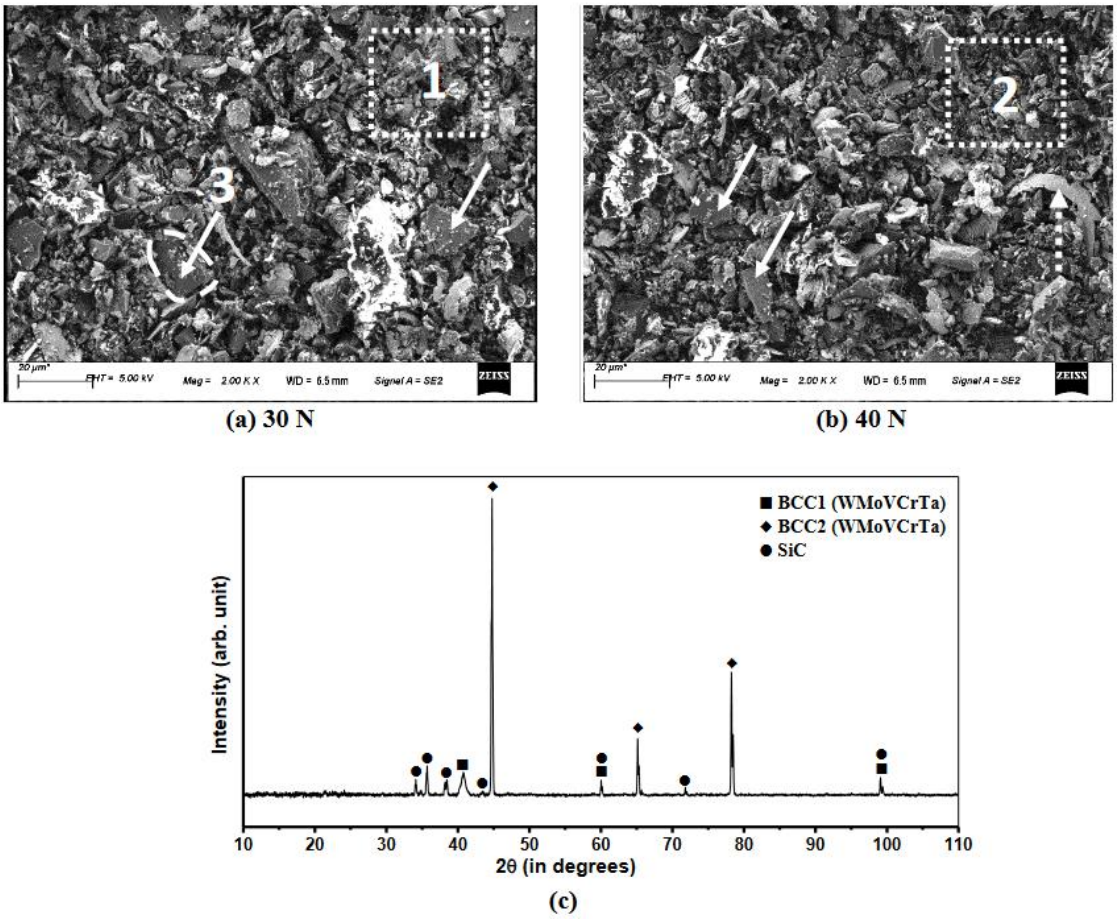

Figure 4. 20 SEM images of the wear debris of the RHEA of WMoVCrTa worn by the loads of (a) 30 N and (b) 40 N and (c) XRD patterns of the debris worn by 40 N

The X-ray elemental mapping of the Figure 4.20 (a) is shown in Figure 21. The mapping also shows the presence of Si. The XRD pattern of the debris shown in Figure 4.20 (c) confirms the presence of SiC particles as per powder diffraction file (pdf reference code 00-001-1118). The XRD pattern of the debris also reveals presence of two BCC phases: BCC1 and BCC2. These phases are confirming to the two BCC phases reported in the as cast WMoVCrTa RHEA [23]. The oxide peaks that are generally found in the XRD pattern of the wear debris were not evident for the present RHEA indicating no oxidation during the wear test. Oxidation has not taken place due to (i) the stability and high melting point of the alloy (T_m = 2849 K) determined as per Guo's criteria [6] and (ii) the low speed of 50 rpm of the disk during the test

that does not generate sufficient temperature at 30 or 40 N loads to oxidize the surface of the RHEA.

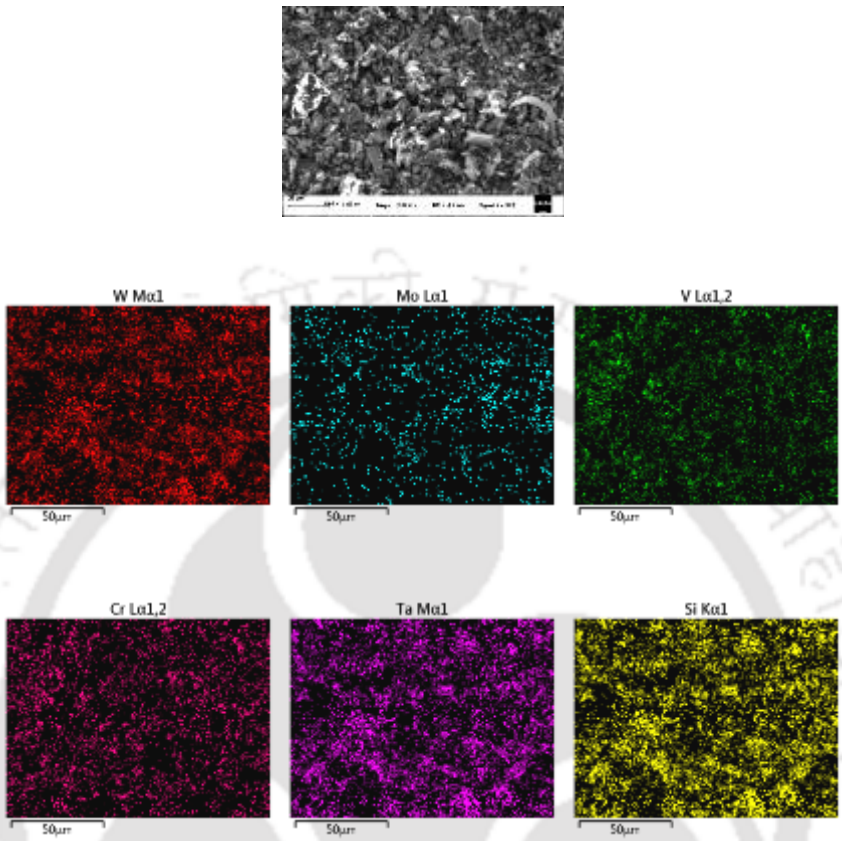

Figure 4. 21 EDS mappings of the Figure 4. 20 (a)

The three-dimensional (3-d) morphology and their corresponding top views of the surfaces worn at 30 N and 40 N are depicted in Table 4.8. The roughness profiles of the corresponding traced surfaces are shown below the top view images. The measures of roughness viz, Rp, R_v, R_z and R_a as per 'ASME B 46.1' are also presented in the table. Here Ra is the roughness average, R_p is the height of the highest profile peak, R_v is the depth of the deepest profile valley, P_t is the profile depth which is the sum of the largest profile peak height and the largest profile valley depth of the P profile within the evaluation length and R_{zi} is the single roughness depth and is determined as $R_{zi} = R_p + R_v$. Mean roughness depth R_z is the arithmetic mean value of the single roughness depths, i.e $R_z = \frac{1}{n}(R_{z1} + R_{z2} + R_{z3\ldots\ldots} R_{zn})$. The R_z values at 30 N and 40 N were 3.87 and 5.47 microns respectively. The R_a values at 30 N and 40 N were 0.549 and 0.825 microns

respectively indicating that the surface roughness average of the RHEA worn at 40N load is ~ 50% higher than that at 30N.

Table 4. 8 Profilometry of the worn surfaces of WMoVCrTa alloy at different loads.

		30 N	40 N
3-d view		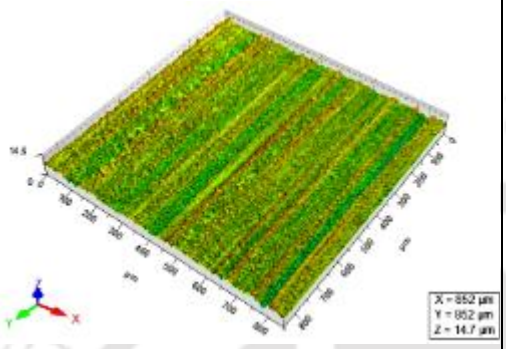	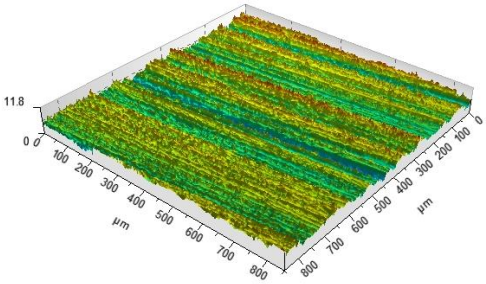
Top -view		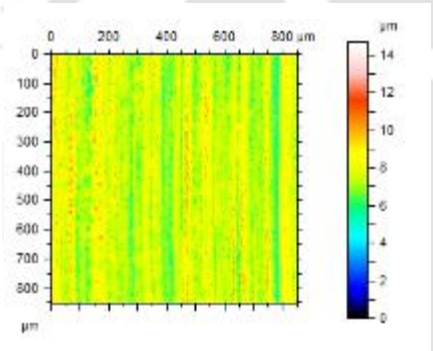	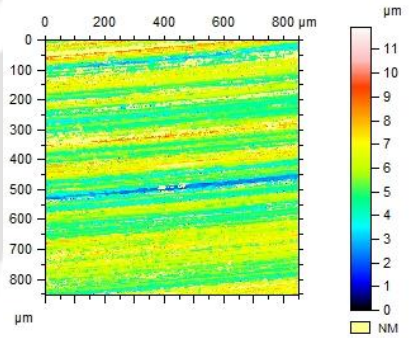
Roughness profile		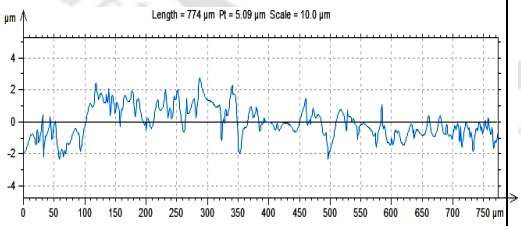	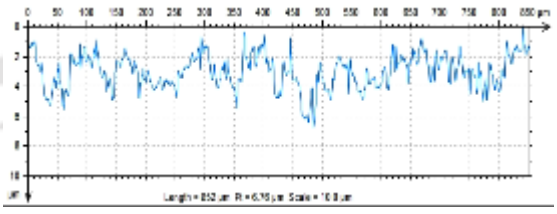
Rough-ness (unit-**µm**)	R_p	1.69	2.64
	R_v	2.18	2.83
	R_z	3.87	5.47
	R_a	0.549	0.825

4.4.5 Discussion on tribological properties

Plots of wear vs. sliding distance for the alloy shown in Figure 4.18 (a) indicate that the wear increased with increase in the normal load. This is mainly due to higher ploughing action by the abrasive particle on the pin surface. With higher load, the abrasive tips penetrate more into the surface of the pin leading to deeper ploughing. This results in higher amount of material removal in the form of debris [135]. The SEM images in Figure 4.19 revealed intense and deeper wear tracks on the surface subjected to 40 N compared to that at 30 N. Moreover, in Table 4.8 the measured mean roughness depth (R_z) value at 40 N is higher than that at 30 N indicating more wear at higher load.

The trend of drastic increase in the wear for WMoVCrTa alloy at 40 N, after 150 meters of sliding (Figure 4.18 (a)) is due to the delamination of the surface in addition to ploughing [135]. The delamination occurs due to the presence of the micro-cracks on the surface as evident in Figure 4.19 (b). The micro-cracks appear near the surface and grow parallel to the sliding direction. These cracks reach a critical length and subsequently initiate delamination by emerging thin and long plate-like debris (shown by dotted arrow in the SEM image in Figure 4.20 (b)) that lead to increase in the wear volume. The micro-cracks were not evident on the worn surface of the WMoVCrTa tested at 30N shown in Figure 4.19 (a). Figure 4.20 (a) also did not reveal any plate-like thin and long chips emerged by surface delamination. The micro-cracks were also not evident on the worn surface of the $W_{23}Mo_{23}V_{17}Cr_8Ta_7Fe_{22}$ alloy.

Figure 4.18 (c) depicts higher COF at higher load compared to that at lower load for the alloy. This is due to higher adhesion strength resulting from more contact pressure at higher load leading to increase in the surface roughness during wear [124, 125]. The COF increases on increasing the surface roughness [31]. The profilometry analysis of the alloy also revealed that the roughness average (R_a) value for 40 N is higher than that for 30 N.

Figure 4.18 (c) also revealed that the slope of the COF curves of both 30 N and 40 N increases at higher rate initially during sliding from 50 to 150 meters in the alloy. This is mainly due to the higher surface roughness at initial period [134]. The wear volume is less at initial period (from 50 to 150 meter) that indicates insufficient amount of lubricating debris. At later period (from 150 to 300 meter) sufficient amount of lubricating debris emerged that filled up the regions in between the asperities and reduced their amount resulting in reduction in the surface roughness. This slows down the rate of increase of COF at later period.

4.5 Mechanically alloyed $W_{23}Mo_{23}V_{17}Cr_8Ta_7Fe_{22}$ powder

The powder mixture of $W_{23}Mo_{23}V_{17}Cr_8Ta_7Fe_{22}$ was mechanically alloyed up to 48 hours by ball milling route to know the extent of alloying. Microstructural characterization and Crystal structure determination of the milled powders were carried out by different techniques and the results are presented and discussed in the subsequent sections.

4.5.1 Particle size analysis

The cumulative particle size distribution plots for the alloy powder of $W_{23}Mo_{23}V_{17}Cr_8Ta_7Fe_{22}$ after ball milling for various periods are shown in Figure 4.22. The median particle sizes (d (0.5)) of the powder mixtures milled for 2, 4, 8, 16, 32 and 48 hours are 26.1, 23.2, 19.3, 27.6, 25.4 and 20.4 micrometers, respectively. The plot of median particle size vs. milling time is shown in Figure 4.23. The figure indicates an initial decrease in the particle size during milling up to 8 hours. During milling, the fine powder particles get trapped between the high-energy milling balls. As a result, two phenomena occur: (a) plastic deformation with simultaneous cold welding of ductile particles and (b) fracturing of brittle particles. The size of brittle particles, *viz.* Mo and W are very coarse compared to the ductile V and Ta particles, though the sizes of the starting Cr particles are very fine (Table 3.3). During the initial milling period up to 8 hours, rate of fracturing of coarse brittle particles dominates over the rate of

plastic deformation of the ductile particles resulting in decrease in the particle size. However, milling beyond 8 hours results in extensive plastic deformation and cold welding of the constituent powder particles. This results in increase in particle size till 16 hours of milling. As the powder particles continuously deform, work hardening takes place resulting in an increase in the brittleness of these milled powders. Milling for 16 hours results in maximum brittleness for the powder mixture. With further milling, the fracture phenomenon dominates, resulting in continuous decrease in the powder particle size as evident from Figure 4.23.

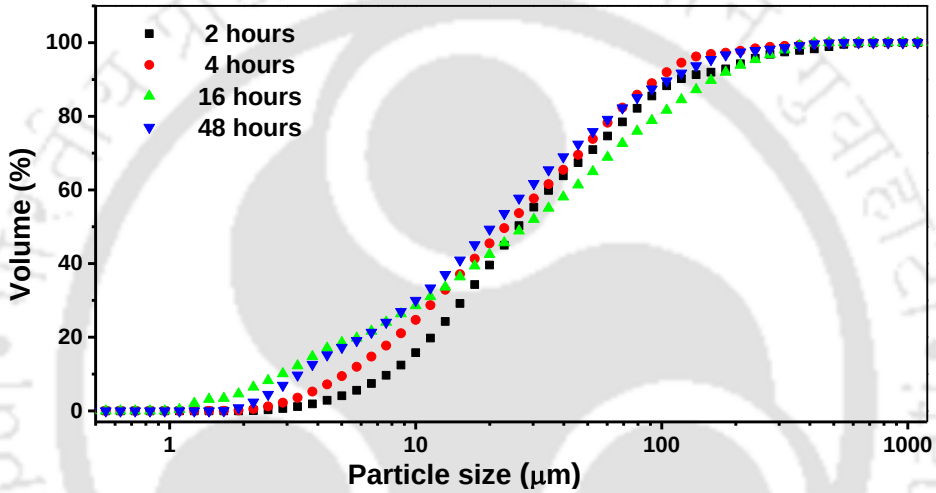

Figure 4. 22 Cumulative particle size distribution curve of the powders milled for 2, 4, 16 and 48 hours.

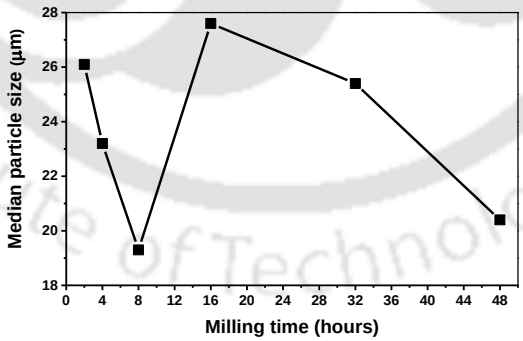

Figure 4. 23 Milling time vs. median particle size (d (0.5)) plot of the powders milled for 2, 4, 8, 16, 32 and 48 hours.

4.5.2 XRD analysis

Figure 4.24 shows the XRD patterns obtained for the powder mixture of $W_{23}Mo_{23}V_{17}Cr_8Ta_7Fe_{22}$ after milling for various periods. The XRD plot for unmilled (0 hours) powder mixture reveals very sharp peaks corresponding to reflections from planes of W, Mo,

and Ta. The intensities of reflections from the planes of Cr were very weak. The intensities of reflections from the planes of V and Fe were not visible. This is due to the low atomic weight of the above elements as compared to other elements (W, Mo, and Ta) in the powder mixture [128]. On progressive milling, the intensity of the peaks from the reflections of the planes of W, Mo, and Ta decreased continuously. The peaks corresponding to the reflections from the planes of Ta show a shift to the left after 2 hours of milling. The Ta peaks disappeared after 32 hours of milling, indicating complete solubility of Ta in solid solution. The small peaks corresponding to reflections from the planes of Cr (at 2θ = 44°) disappeared completely after milling the powder for 48 hours. Only four diffraction peaks were evident after ball milling for 32 hours.

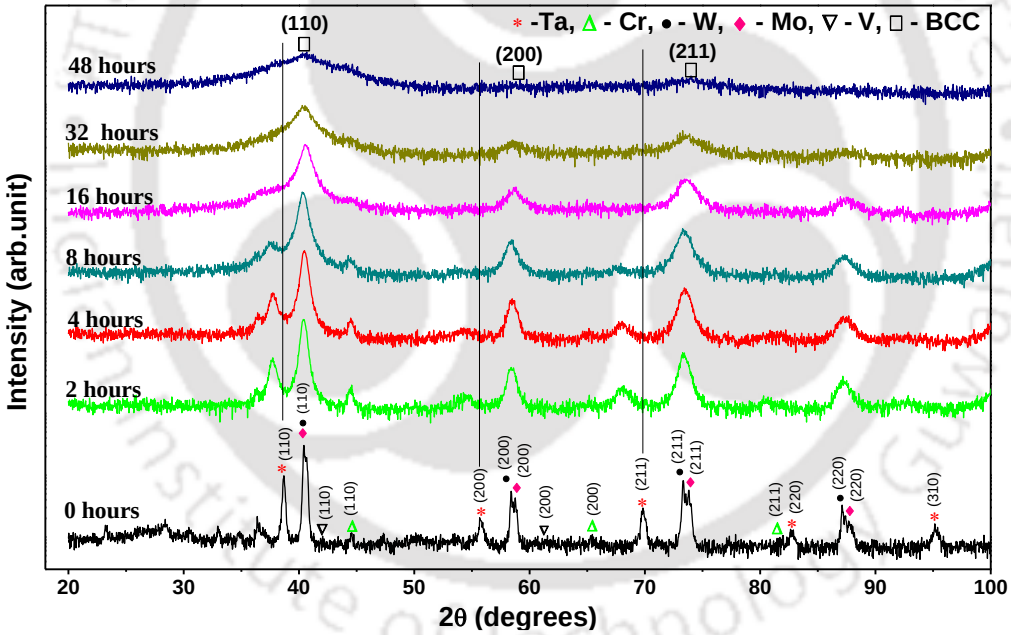

Figure 4. 24 XRD patterns of powder mixtures after various milling periods

Continuous Peak broadening was observed on progressive milling due to the crystallite size reduction and lattice strain in the milled powder [115]. Milling for 48 hours resulted in further peak broadening and disappearance of the peak corresponding to the 2θ of 87.4°, which was evident in the diffraction pattern of 32 hours milled powder. Analysis of the three diffraction peaks obtained from the 48 hours milled powder revealed that they correspond to reflections from (110), (200) and (211) planes of a BCC crystal with inter-planar spacings of 2.23 Å, 1.57

Å, and 1.28 Å, respectively. The average lattice parameter of the BCC crystal was determined as 3.143 Å.

4.5.3 TEM analysis

TEM investigation was carried out to further confirm the crystal structure of the mechanically alloyed powder mixture of $W_{23}Mo_{23}V_{17}Cr_8Ta_7Fe_{22}$. Figure 4.25 shows (a) bright-field TEM image and (b) corresponding selected area electron diffraction (SAED) patterns of the 48 hours milled powder mixture. The concentric rings, along with bright spots in the SAED pattern indicate polycrystalline structure [119]. Analysis of the SAED pattern reveals that the concentric rings correspond to reflections from (110), (200), and (211) planes of the BCC structure. The inter-planar spacing (d_{hkl} values) of the corresponding BCC planes were evaluated and are shown in Table 4.9. Results of TEM-SAED analysis revealed that milling for 48 hours results in a homogeneous single-phase alloy powder with a BCC structure having lattice parameter of 3.140 Å which is in good accordance with the XRD results.

The HRTEM image of the powder milled for 48 hours is shown in Figure 4.26 (a). For the corresponding IFFT image and line profile in Figure 4.26 (b) and (c), the inter-planar spacing (d) of (110) plane was found to be 2.54Å which is close to the values for BCC structure obtained from the XRD results.

Table 4. 9 The d_{hkl} values obtained from SAED analysis corresponding to different planes of BCC crystal of 48 hours milled powder of $W_{23}Mo_{23}V_{17}Cr_8Ta_7Fe_{22}$.

planes	2θ (°)	d_{hkl} (Å)
(110)	42.58	2.124
(200)	57.64	1.602
(211)	71.906	1.312

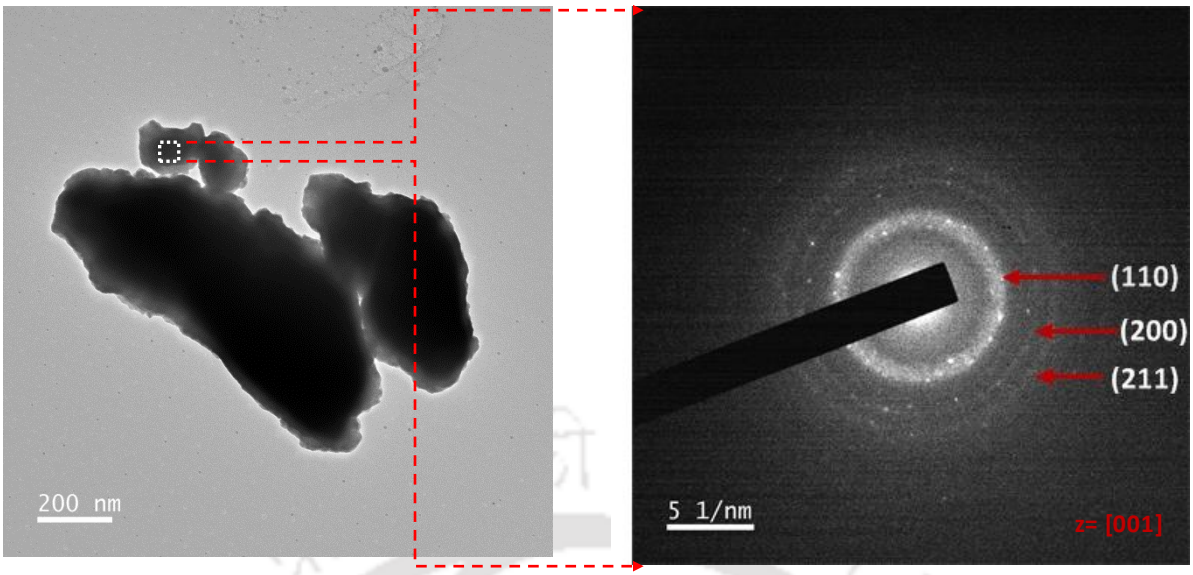

(a) (b)

Figure 4. 25 (a) Bright Field TEM image of the marked particle and (b) SAED patterns of the corresponding particle of 48 hours milled powder of $W_{23}Mo_{23}V_{17}Cr_8Ta_7Fe_{22}$.

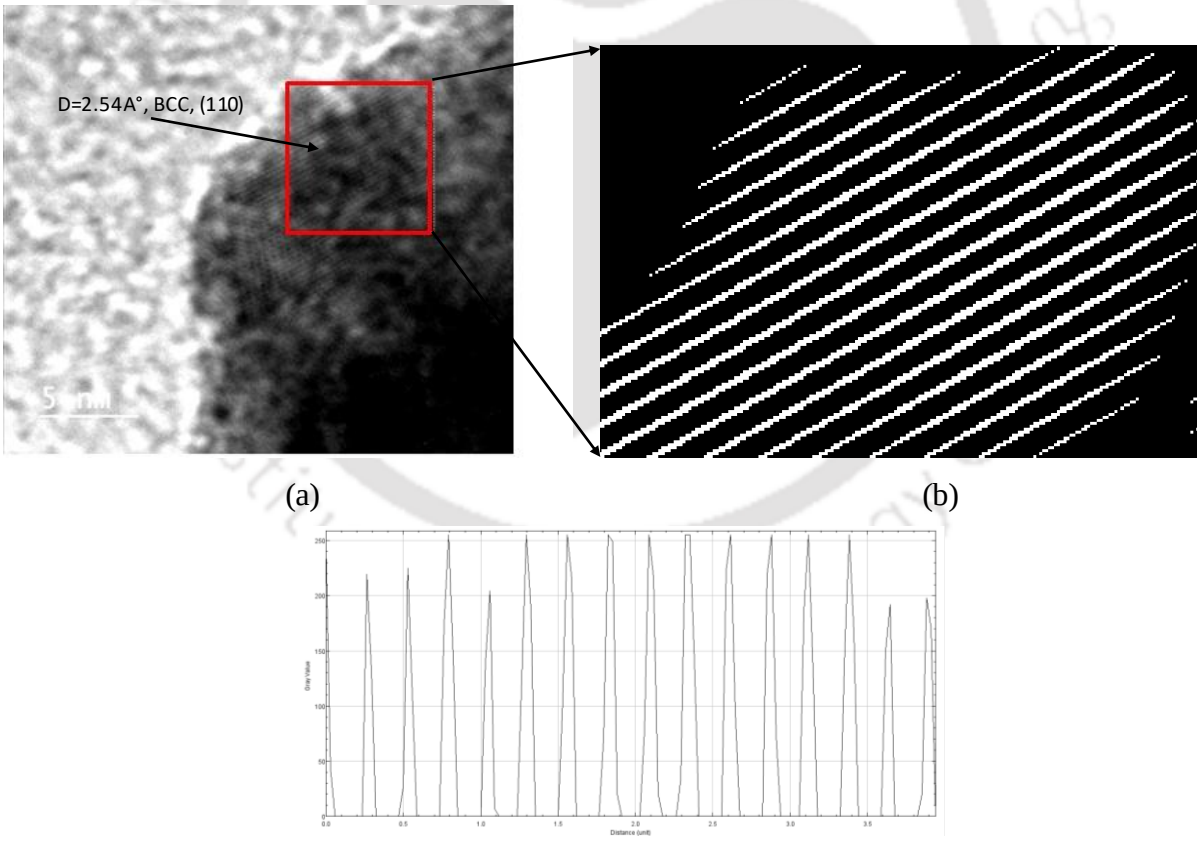

(a) (b)

(c)

Figure 4. 26 (a) HRTEM image, (b) IFFT image of the selected region in corresponding HRTEM image and (c) line profile of the IFFT image of 48 hours milled powder of $W_{23}Mo_{23}V_{17}Cr_8Ta_7Fe_{22}$.

4.5.4 SEM and EDX analysis

Field emission scanning electron (SEM) micrographs of $W_{23}Mo_{23}V_{17}Cr_8Ta_7Fe_{22}$ powder mixture after milling for various hours are shown in Figure 4.27. The powder particles undergo morphological changes during the milling process. The powder particles show irregular morphology after 2 and 4 hours of milling (Figure 4.27 (a) and (b)). After 48 hours of milling, the powder particles were very fine with morphology almost similar to equiaxed powders. The

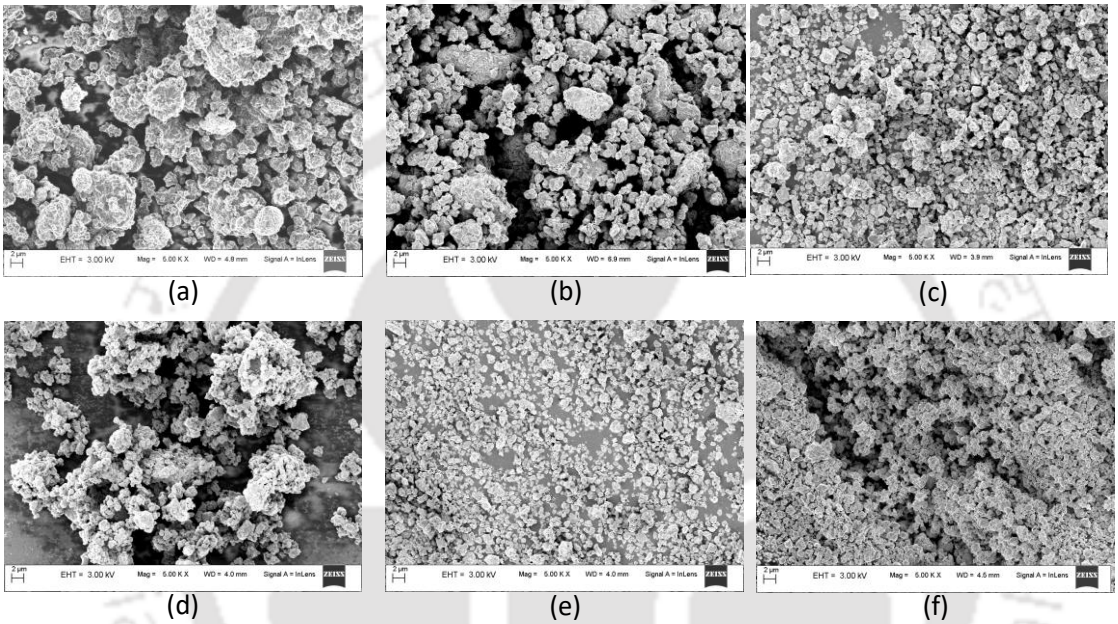

Figure 4. 27 SEM micrographs of the powder mixture of W-Mo-V-Cr-Ta-Fe after (a) 2 hours (b) 4 hours, (c) 8hours, (d) 16 hours, (e) 32 hours, and (f) 48 hours of milling.

average sizes of powder mixture milled for various hours determined from the electron micrographs show the same trend as in Figure 4.23. Observation of the morphology of 2 and 16 hours milled powder by SEM shows agglomeration of powder particles. The fracture and reduction in the size of the powder particles are evident from the micrographs of 32 and 48 hours milled powder (Figure 4.27 (e) and (f)).

EDS spectrums of the powders milled for various hours is shown in Figure 4.28. The quantitative analysis of chemical compositions determined by EDS (taking average of four different areas) of the powder mixtures milled for 4, 32, and 48 hours are depicted in Table4.10.

The atomic percentages of the elements in the 48 hours milled powder are equivalent to that of the starting powder mixture.

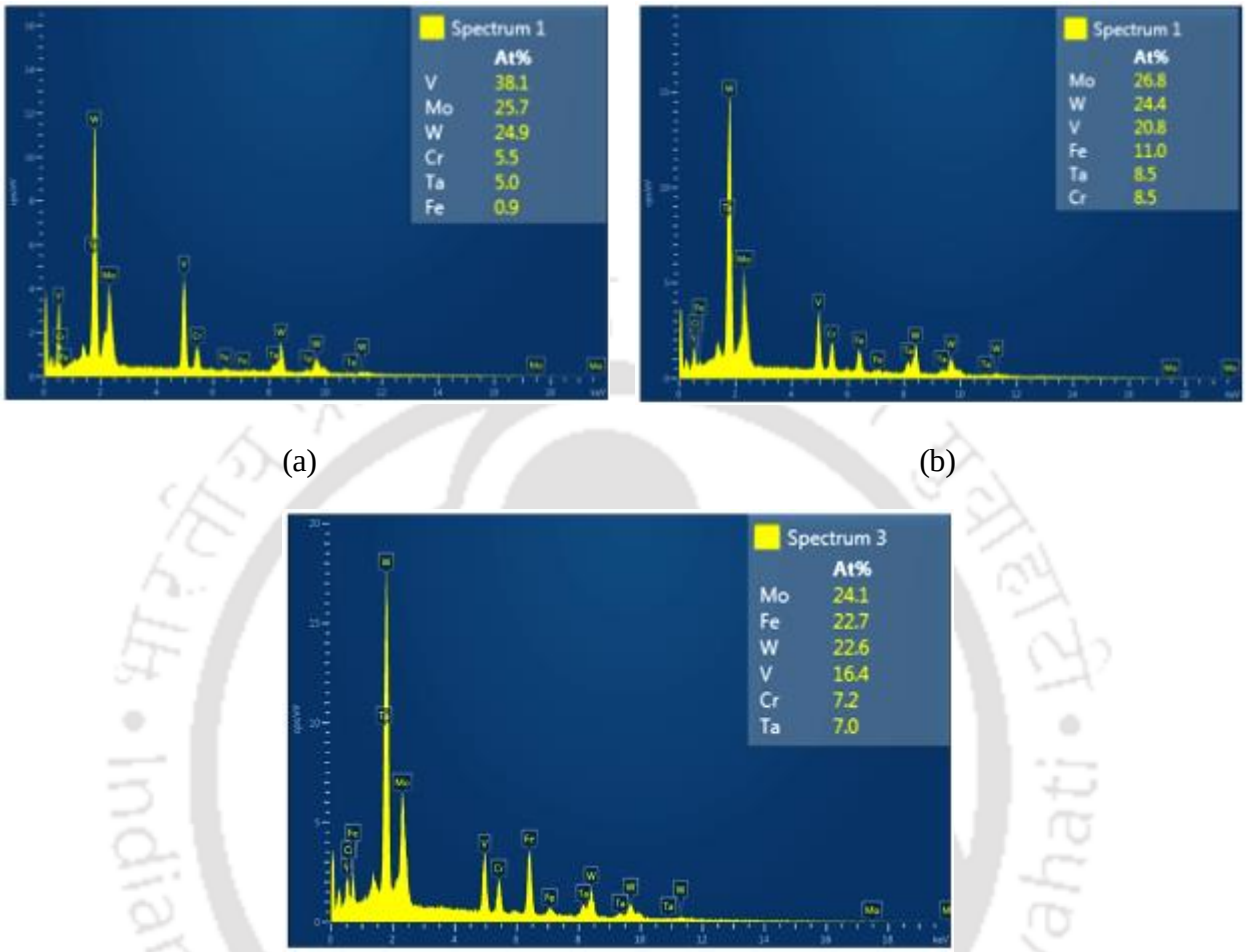

(a) (b)

(c)

Figure 4. 28 The quantitative analysis of EDS spectra of powder mixtures milled for (a) 4 hours (b) 32 hours and (c) 48 hours.

Table 4. 10 Quantitative analysis of chemical compositions in milled powder mixtures.

Mill time (hour)	W (at. %)	Mo (at. %)	V (at. %)	Cr (at. %)	Ta (at. %)	Fe (at. %)
4	23 ±0.8	27 ±0.9	37 ±0.9	6 ±0.8	6 ±0.9	1 ±0.5
32	25 ±0.7	27 ±0.8	20 ±0.8	9 ±0.7	8 ±0.9	11 ±0.5
48	23 ±0.8	23 ±0.5	17 ±0.7	8 ±0.9	7 ±0.5	22 ±0.8

4.6 Arc melted $W_{23}Mo_{23}V_{17}Cr_8Ta_7Fe_{22}$ alloy

The alloy powder of $W_{23}Mo_{23}V_{17}Cr_8Ta_7Fe_{22}$ was consolidated by cold compaction and subsequent arc melting to fabricate the alloy ingots. The following section shows the characterization of such ingots by illustrating their structure (crystal structure and microstructure) and properties (mechanical and tribological) investigated by various techniques.

4.6.1 SEM and EDX analysis

Figure 4.29 depicts the optical micrographs of the arc melted alloy of $W_{23}Mo_{23}V_{17}Cr_8Ta_7Fe_{22}$. The figure reveals three different phases labeled A, B, and C. The percentage area of phases A, B, and C are 76, 4 and 20, respectively. SEM micrograph using backscattered detector is shown in Figure 4.30 (a). The micrograph reveals dendritic grains (phase A), interdendritic segregation (Phase C), and the black spherical phase (Phase B). EDS spectra of phases marked A, B, and C in Figure 4.30 (b) are shown in Figure 4.30 (c), (d), and (e), respectively. Table 4.11 presents the result of the quantitative EDS analysis for the three phases. Hence from the table, the Phases A, B and C can be named as $W_{56}Mo_{35}V_1Fe_8$, $W_1Mo_1V_{57}Cr_{24}Ta_7Fe_{10}$ and $W_{12}Mo_{30}Cr_2Fe_{56}$ phases. From Equation 4 in Section 2.3, the melting temperatures of phases A, B and C were determined as 3227°C, 2294°C, and 2216°C, respectively. During cooling from the molten state, the first part to solidify is Phase A followed by Phase B. The final stage of solidification is formation of Phase C at the interdendritic regions. Molybdenum and Tungsten have almost same atomic size (1.39 Å) and excellent chemical affinity [129, 130]. Thus, they prefer to form substitutional solid solution that makes phase A rich in W and Mo (Table 4.11). The formation of early Phase A resulted in the consumption of major amounts of W and Mo.

W and Mo were almost negligible in Phase B whereas the fraction of V, Cr, and Ta in phase C was marginal. From Midemma's table of binary enthalpy of mixing shown in Table 2.3, V-Cr has a higher negative binary enthalpy of mixing. In addition, the melting points of these

elements are almost similar and the atomic size difference is very small. All the above reasons enable V and Cr to form phase B. The binary enthalpy of mixing of V-Mo, V-W, Cr-Mo and Cr-W are more positive that makes phase B (rich in V and Cr) depleted in W and Mo and phase A (rich in W and Mo) depleted in V and Cr. The elements Ta and Fe are present in small quantities in phase B as the binary enthalpy of mixing of Cr-Ta and V-Fe are more negative (Table 2.3).

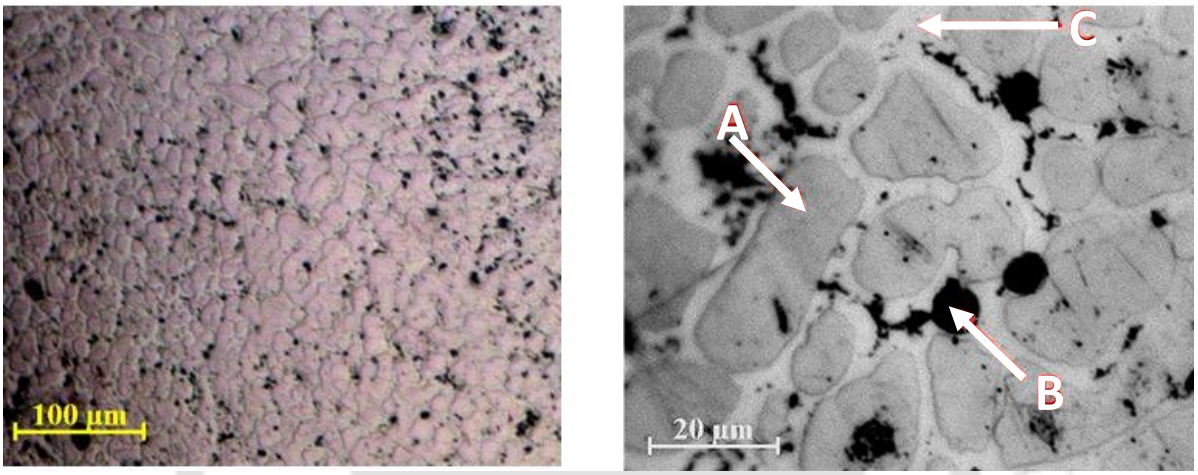

(a) (b)

Figure 4. 29 Microstructure of the arc melted RHEA of $W_{23}Mo_{23}V_{17}Cr_8Ta_7Fe_{22}$ by Light microscope at magnification of (a) 20x and (b) 100x.

Phase C was found to be rich in Fe (56 atomic %) with 12 atomic % of W and 30 atomic % of Mo. Though Ta has large negative binary enthalpies of mixing with all other constituents except W, it is absent in Phase A and C due to its large atomic size compared with other elements. The density for the alloy was obtained as 12.54 g/cm.

Table 4. 11 Chemical compositions of various phases in the cast RHEA of $W_{23}Mo_{23}V_{17}Cr_8Ta_7Fe_{22}$

Elements	W (at.%)	Mo (at.%)	V (at.%)	Cr (at.%)	Ta (at.%)	Fe (at.%)
Phase A	56 ±0.8	35 ±0.6	1 ±0.7	0 ±0.7	0	8 ±0.8
Phase B	1 ±0.9	1 ±0.8	57 ±0.8	24 ±0.8	7 ±0.2	10 ±0.8
Phase C	12 ±0.8	30 ±0.9	0 ±0.9	2 ±0.6	0	56 ±0.9

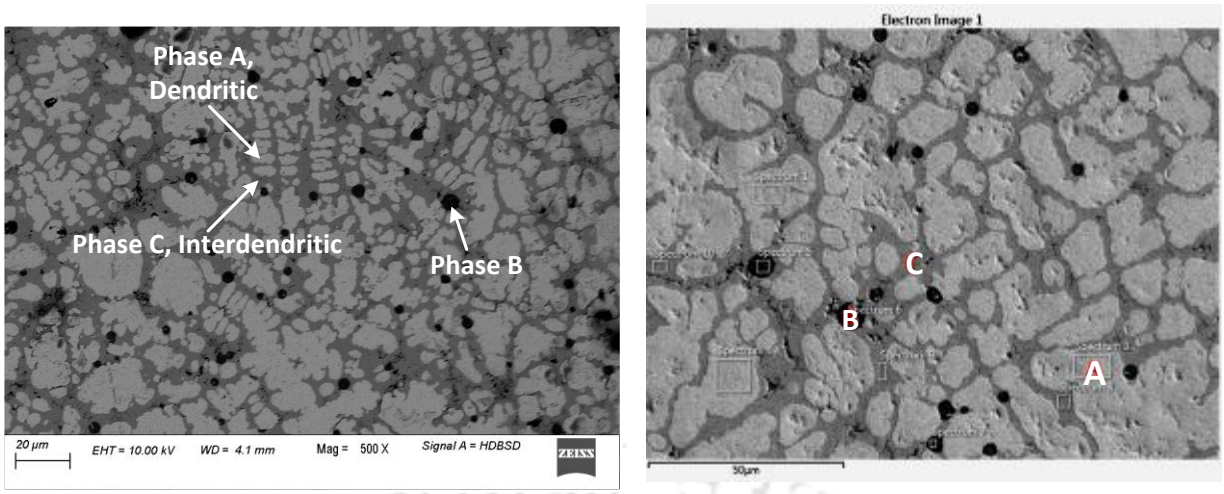

Figure 4. 30 Micrograph of the arc melted RHEA of $W_{23}Mo_{23}V_{17}Cr_8Ta_7Fe_{22}$ by SEM in (a) HDBSD mode and (b) INLENS mode for chemical composition analysis and (c), (d), (e) are EDX spectra of phase A, phase C and phase B respectively marked in the micrograph in (b).

4.6.2 XRD analysis

The XRD patterns of 48 hours milled powder and arc melted alloy of $W_{23}Mo_{23}V_{17}Cr_8Ta_7Fe_{22}$ are presented in Figure 4.31. Analysis revealed the formation of three different phases in the arc melted sample where two correspond to BCC structure and the third to an intermetallic phase. From the XRD patterns, the peaks at 2θ of 40.6°, 58.6°, 73.9°, 88.0° were identified as corresponding to reflections from body-centered cubic structure (BCC1 phase). The above 2θ values are similar to that of the elemental W and/or Mo with the small peak shift. Hence these reflections are emerging from planes of Phase A of the alloy which contains W and Mo in major

proportions (Table 4.11). Similar BCC phases were also observed in HEAs with W and Mo [9, 116 and 117]. The reflections from the planes of (110), (200), (211), and (220) for the corresponding BCC1 phase are labeled in Figure 4.31. The BCC1 peak positions of the arc melted sample were found to be shifted to the right compared to the BCC peak positions of the 48 hours milled powder. The lattice parameter for the BCC1 phase of the arc melted alloy was determined as 3.135 Å whereas the corresponding value for the BCC phase of the 48 hours milled powder was 3.143 Å indicating a lattice contraction of 0.25%.

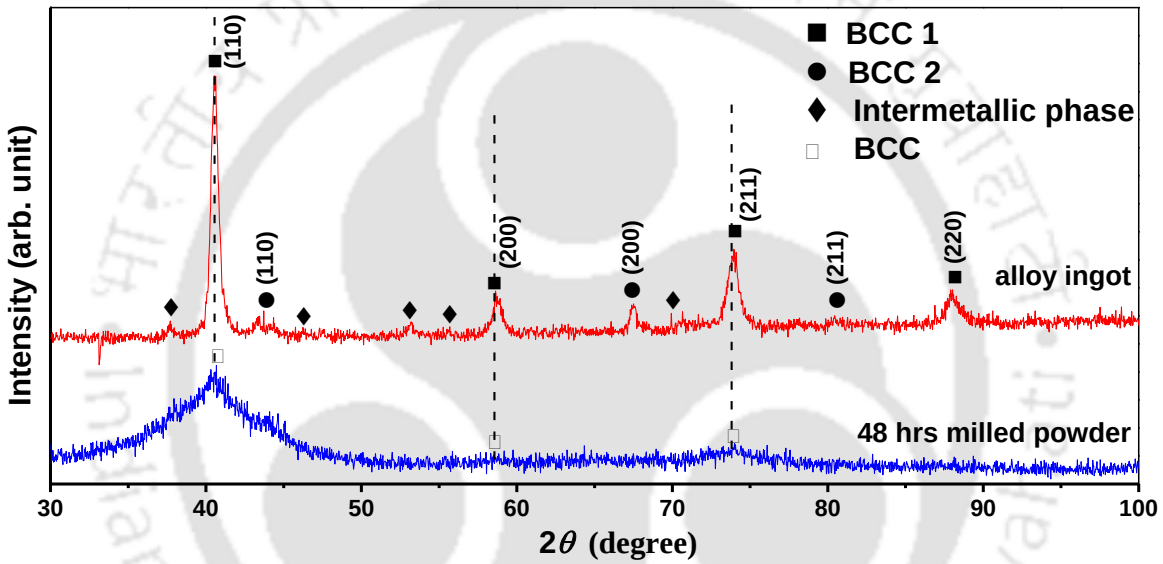

Figure 4. 31 XRD patterns of the 48 hours milled powder and the arc melted RHEA of $W_{23}Mo_{23}V_{17}Cr_8Ta_7Fe_{22}$

Analysis of XRD peaks at 2θ values of 43.7°, 67.3°, and 80.4° of the arc melted alloy revealed a second body-centered cubic phase (BCC2 phase). The corresponding peak patterns are similar to that of the elemental Fe and thus they are regarded as the reflections emerging from different planes of Phase C in Figure 4.30 (a) as Fe is the major element of this phase (Table 4.11). The lattice parameter of the BCC2 phase was determined as 2.860 Å.

Few residual peaks with very small intensity found at 2θ = 37.7°, 46.5°, 53.2°, 55.6°, and 69.9° were unable to match with the standard BCC, FCC or HCP patterns; hence they are

presumed to be of an intermetallic phase. From the EDS analysis in Figure 4.30 (d), this intermetallic phase is regarded as Phase B containing Cr and V as major elements with small amount of Ta and Fe. Since the peak intensities from this phase are very weak, proper indexing and crystal structure determination could not be carried out.

4.6.3 Mechanical properties

Engineering stress vs engineering strain plots of $W_{23}Mo_{23}V_{17}Cr_8Ta_7Fe_{22}$ RHEA at various temperatures were obtained from the uniaxial compression test data. The typical engineering stress-strain plots of $W_{23}Mo_{23}V_{17}Cr_8Ta_7Fe_{22}$ alloy at four different temperatures are shown in Figure 4.32. The plot results are shown in Table 4.12. At 25° C, the yield stress of the alloy was 1688 ± 31 MPa at a strain of 7.1 ± 0.27%. The ultimate compressive stress at this temperature was 1708 ± 28 MPa at a strain of 7.3 ± 0.22 %. At 800° C, the yield stress of the alloy was 1041 ± 29 MPa at a strain of 9.1 ± 0.34 %. At this temperature the alloy fractures immediately after reaching the yield point indicating only a very small amount of plastic deformation due to small strain hardening region. At 1000° C, the yield stress of the alloy increased drastically to 1514 ± 24 MPa at a strain of 8.3 ± 0.14 %. The corresponding ultimate compressive stress was 1749 ± 26 MPa at 10.6 ± 0.17 % strain. It is to be noted that 89.7 % of the room temperature yield strength of the RHEA is retained at 1000 °C. The yield stress and the yield strain of the present alloy at high temperatures are higher than the values reported for other RHEAs [9, 29]. It can be observed that the yield stress of $W_{23}Mo_{23}V_{17}Cr_8Ta_7Fe_{22}$ alloy increases with an increase in temperature between 800° C to 1000° C showing a yield stress anomaly (YSA) [120, 121, 122, 123].

The high compressive strengths at temperatures up to 1000° C are attributed to (a) presence of strong BCC solid solution phase A consisting of high melting point elements such as W and Mo as major constituents with a small amount of Fe, (b) presence of intermetallic phase B at grain boundary regions that impede deformation, and (c) severe lattice distortion effect [5]

in the alloy. Though room temperature compressive yield strength of the present alloy is lower than some RHEAs [29 and 131], the superior yield strain exhibited by this alloy than those RHEAs at elevated temperatures is advantageous for high-temperature applications [29 and 131]. The alloy softens drastically when exposed to 1200° C resulting in very low ultimate compressive strength (57 ± 11 MPa). The softening occurred due to the phase C containing high amount of Fe. But this phase is also responsible for good strain values obtained for the alloy. Hence tailoring the Fe content may increase the temperature range of the corresponding alloy with high strength and good strain.

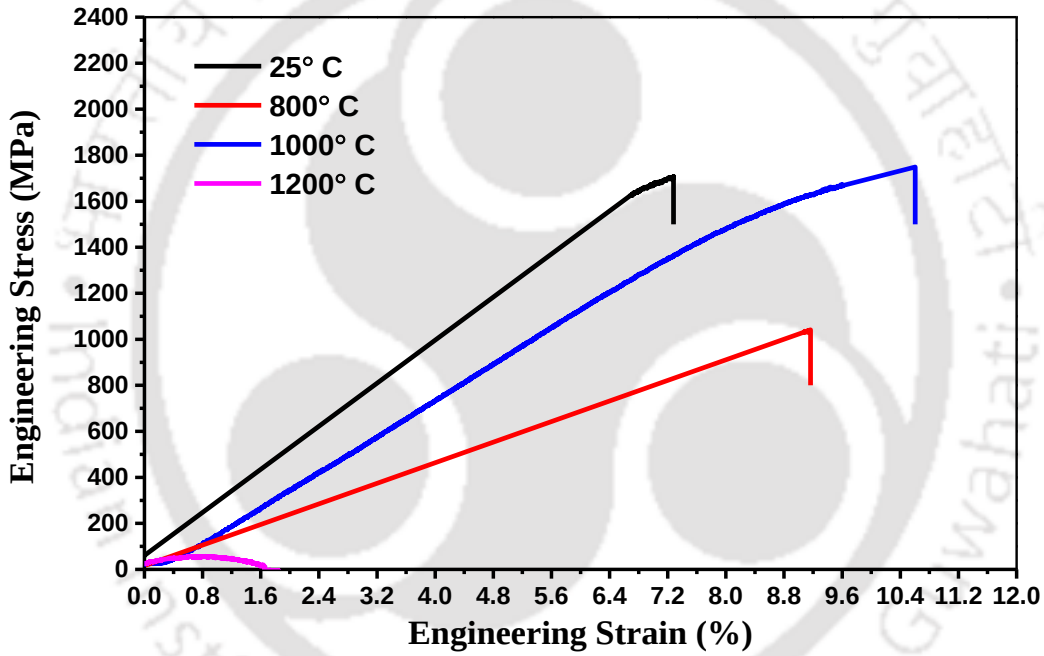

Figure 4. 32 Compressive engineering stress-strain curves of the $W_{23}Mo_{23}V_{17}Cr_8Ta_7Fe_{22}$ alloy at different temperatures.

By comparing with the equiatomic WMoVCrTa alloy, the yield strength and yield strain of the $W_{23}Mo_{23}V_{17}Cr_8Ta_7Fe_{22}$ alloy at 1000 °C, are respectively about 1.9 and 1.6 times higher than that of the WMoVCrTa alloy. The results indicate that the equiatomic WMoVCrTa alloy can be utilized for applications till 1200 °C whereas the $W_{23}Mo_{23}V_{17}Cr_8Ta_7Fe_{22}$ alloy can be used up to 1000 °C. SEM fractographs of the $W_{23}Mo_{23}V_{17}Cr_8Ta_7Fe_{22}$ alloy after testing at room temperature and 1000 °C are shown in Figure 4.33 (a) and (b), respectively. The features of the

Table 4. 12 Results of compression test of $W_{23}Mo_{23}V_{17}Cr_8Ta_7Fe_{22}$ RHEA.

Test Temp.(°C)	Yield stress (MPa)	Yield strain (%)	Ultimate stress (MPa)	Ultimate strain (%)
25	1688 ± 31	7.1 ± 0.27	1708 ± 28	7.3 ± 0.22
800	1041 ± 29	9.1 ± 0.34	1041 ± 20	9.1 ± 0.30
1000	1514 ± 24	8.3 ± 0.14	1749 ± 26	10.6 ± 0.17
1200	----	----	57 ± 11	0.8 ± 0.12

sample tested at room temperature show intergranular failure. From the fracture features of the sample tested at 1000 °C, it appears that the sample has deformed plastically before failure.

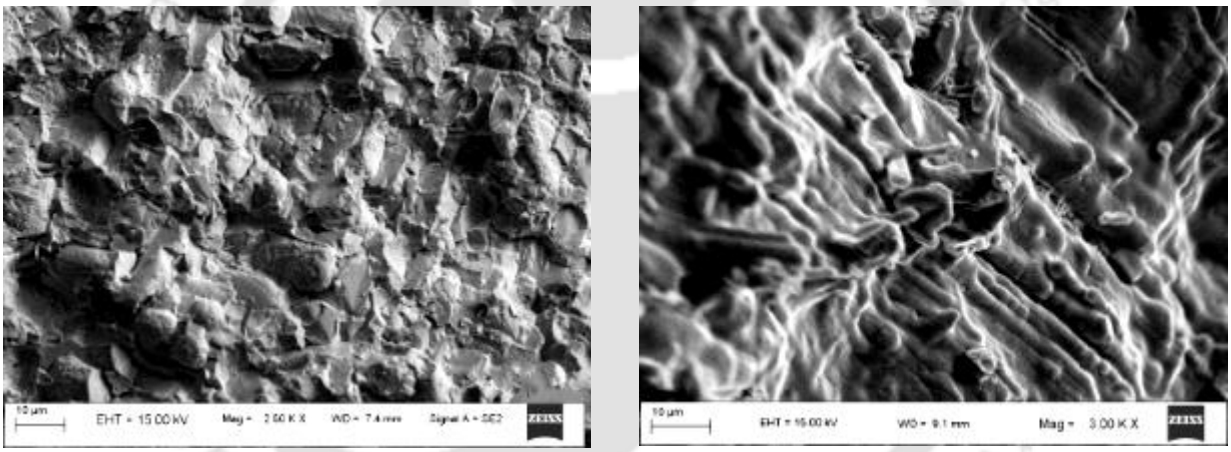

(a) (b)

Figure 4. 33 SEM micrographs of fracture surfaces of the $W_{23}Mo_{23}V_{17}Cr_8Ta_7Fe_{22}$ alloy at (a) room temperature and (b) 1000° C.

The hardness of the alloy was determined by Vickers Hardness Tester and the top view of the hardness indent is shown in Figure 4.34. The overall room temperature hardness of the $W_{23}Mo_{23}V_{17}Cr_8Ta_7Fe_{22}$ alloy is 800 ± 20 HV. However, the overall room temperature hardness of the WMoVCrTa alloy ingot was 773 ± 20 HV [23]. The results of compression and hardness tests reveal that alloying with Fe increases the strength and hardness of W-Mo-V-Cr-Ta HEA.

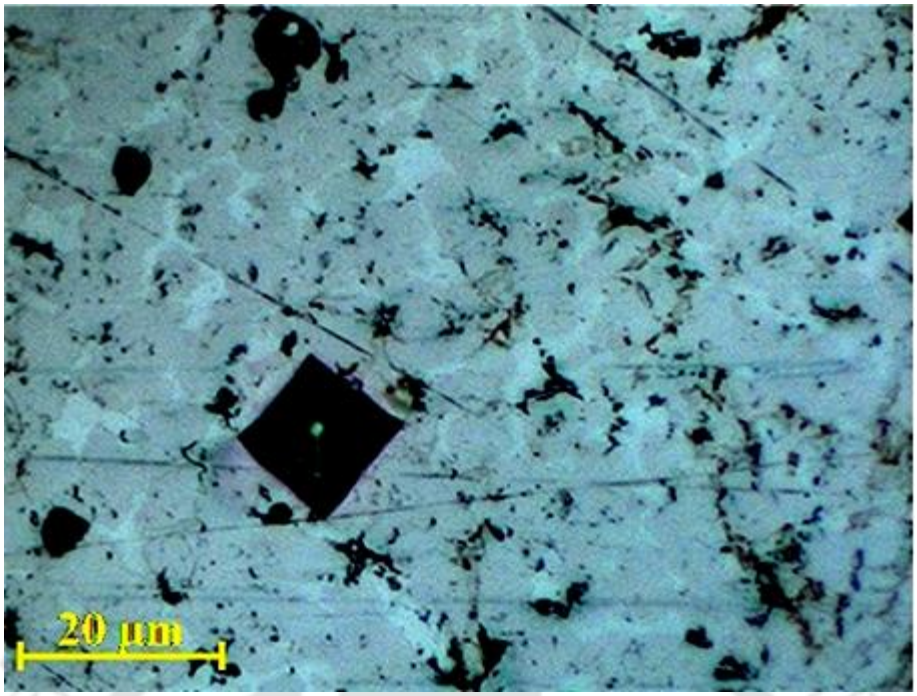

Figure 4. 34 Top view of the hardness indent of $W_{23}Mo_{23}V_{17}Cr_8Ta_7Fe_{22}$ alloy.

4.6.4 Tribological properties

The plots of wear vs. sliding distance of the $W_{23}Mo_{23}V_{17}Cr_8Ta_7Fe_{22}$ alloy at 30 N and 40 N loads are shown in Figure 4. 35 (a). The wear depth increased almost linearly with the increase in sliding distance at both the loads. However, at the load of 40N, the wear increased at higher rate than that at 30 N. After 300 meters of sliding, the calculated total wear volume of $W_{23}Mo_{23}V_{17}Cr_8Ta_7Fe_{22}$ at 40 N is 1.5 times higher than that at 30 N. The wear coefficients of $W_{23}Mo_{23}V_{17}Cr_8Ta_7Fe_{22}$ at 30 N and 40 N loads are shown in Figure 4.35 (b). The figure indicates that the wear coefficient at 40 N is 1.1 times higher compared to that at 30 N. Figure 4. 35 (c) shows the plots of COF vs. sliding distance of the alloy at the loads of 30 N and 40 N. The figure indicates higher COF at higher load. The average values of COF at 30 N and 40 N are 0.32 ± 0.02 and 0.37 ± 0.02, respectively. The COF vs sliding distance curve of 30 N increased at higher rate than that of 40 N.

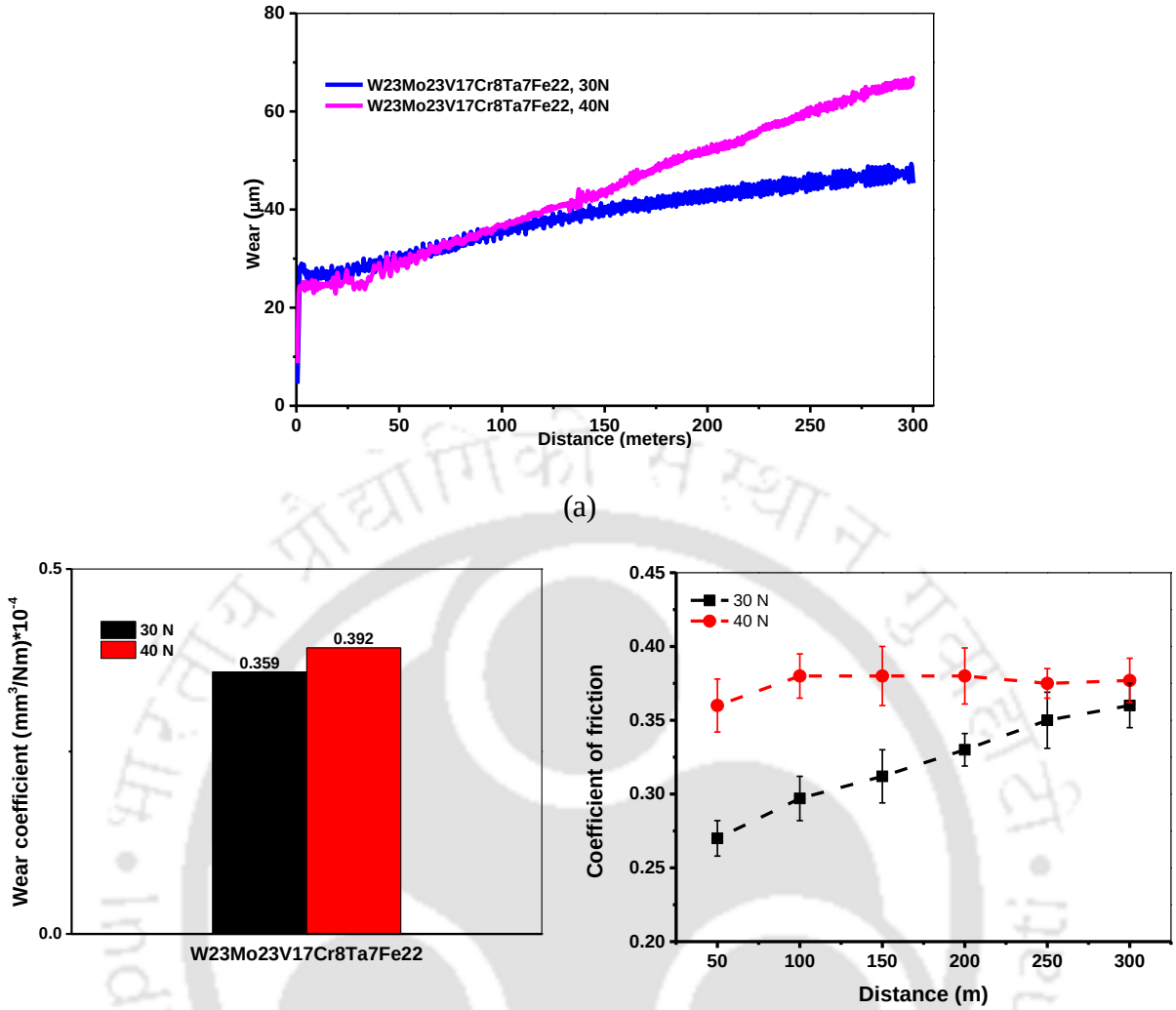

Figure 4. 35 (a) Wear vs. sliding distance, (b) Wear Coefficient and (c) Coefficient of Friction vs. sliding distance plots of the $W_{23}Mo_{23}V_{17}Cr_8Ta_7Fe_{22}$ RHEA at the loads of 30N and 40 N.

SEM image of the worn surface of the alloy shown in Figure 4.36 reveals wear grooves formed due to ploughing action by the abrasives. The wear tracks were not continuous as the alloy has three different phases ($W_{56}Mo_{35}V_1Fe_8$, $W_1Mo_1V_{57}Cr_{24}Ta_7Fe_{10}$ and $W_{12}Mo_{30}Cr_2Fe_{56}$). The wear directions are shown by dashed arrows in Figure 4.36. The micro-cracks were not evident on the worn surface of the alloy.

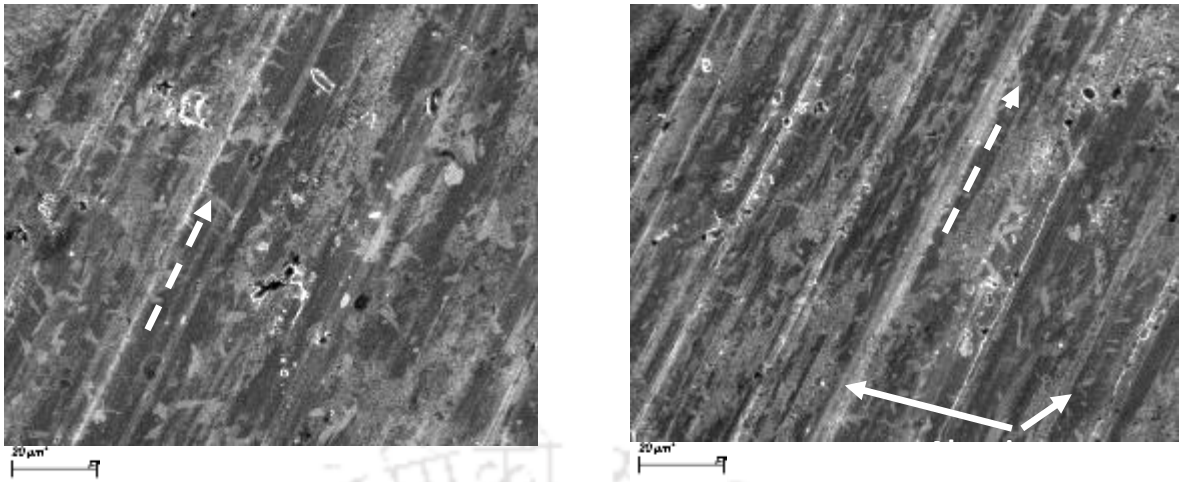

(a) 30 N (b) 40 N

Figure 4. 36 SEM images of the surface of the $W_{23}Mo_{23}V_{17}Cr_8Ta_7Fe_{22}$ alloy after wear by the loads of (a) 30N and (b) 40 N.

The SEM images of the debris collected after the test at different loads are shown in Figure 4.37 (a) and (b) and their composition analysis results at the numbered regions are shown in Table 4.13. The composition analysis at location 1 and 2 in Figure 4.37 revealed that they are the debris that emerged from the RHEA. The large debris shown by solid arrows in the images were identified as SiC. The X-ray elemental mapping of the Figure 4.37 (a) is shown in Figure 4.38. The mapping also shows the presence of Si. The XRD pattern of the debris shown in Figure 4.37 (c) confirms the presence of SiC particles. The XRD pattern of the debris also reveals presence of two BCC phases: BCC1 and BCC2. These phases are confirming to the two BCC phases reported in the as cast $W_{23}Mo_{23}V_{17}Cr_8Ta_7Fe_{22}$ RHEA [132]. Oxide peaks were absent in the XRD pattern of the debris.

The three-dimensional (3-d) morphology and their corresponding top views of the surfaces worn at 30 N and 40 N loads are depicted in Table 4.14. The roughness profiles of the corresponding traced surfaces are shown below the top view images. The measurement of the roughness profiles determines that the R_z values for 30 N and 40 N are 3.87 and 5.11 microns respectively. The R_a values at 30 N and 40 N were 0.444 and 0.614 microns respectively

indicating that the surface roughness average of the RHEA worn at 40N load is ~ 38% higher than that at 30N.

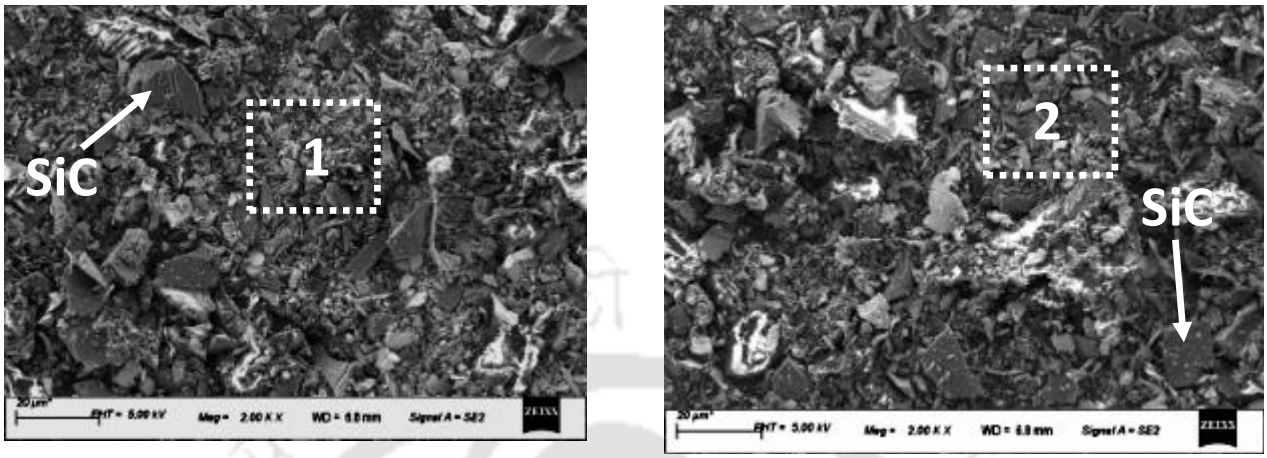

(a) 30 N (b) 40 N

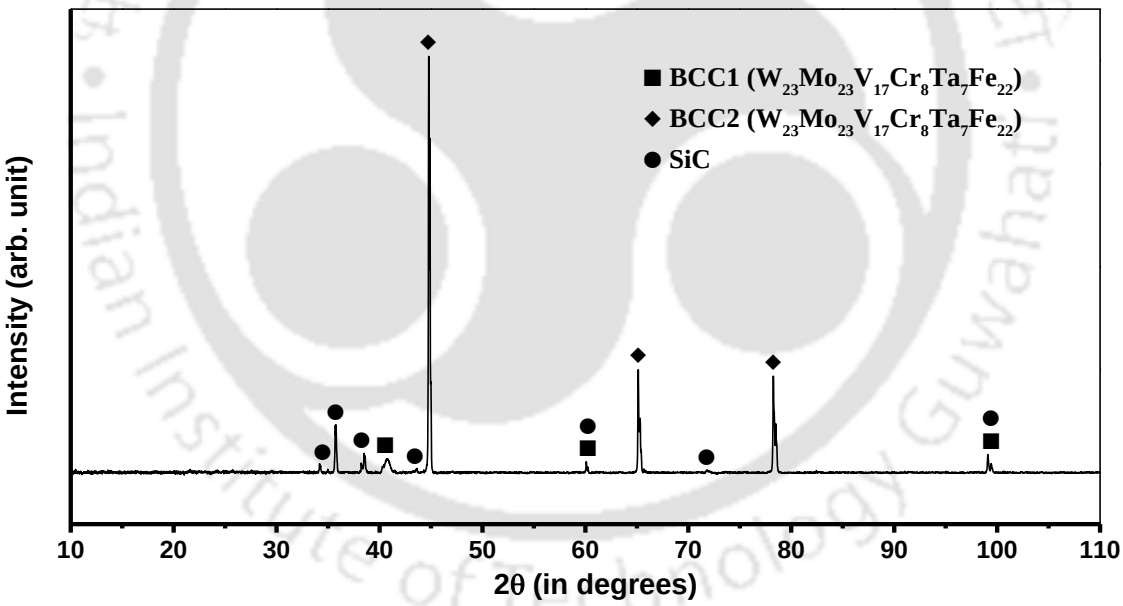

(c)

Figure 4. 37 SEM images of the wear debris of the RHEA of $W_{23}Mo_{23}V_{17}Cr_8Ta_7Fe_{22}$ after wear by the loads of (a) 30 N and (b) 40 N and (c) XRD patterns of the debris worn by 40 N

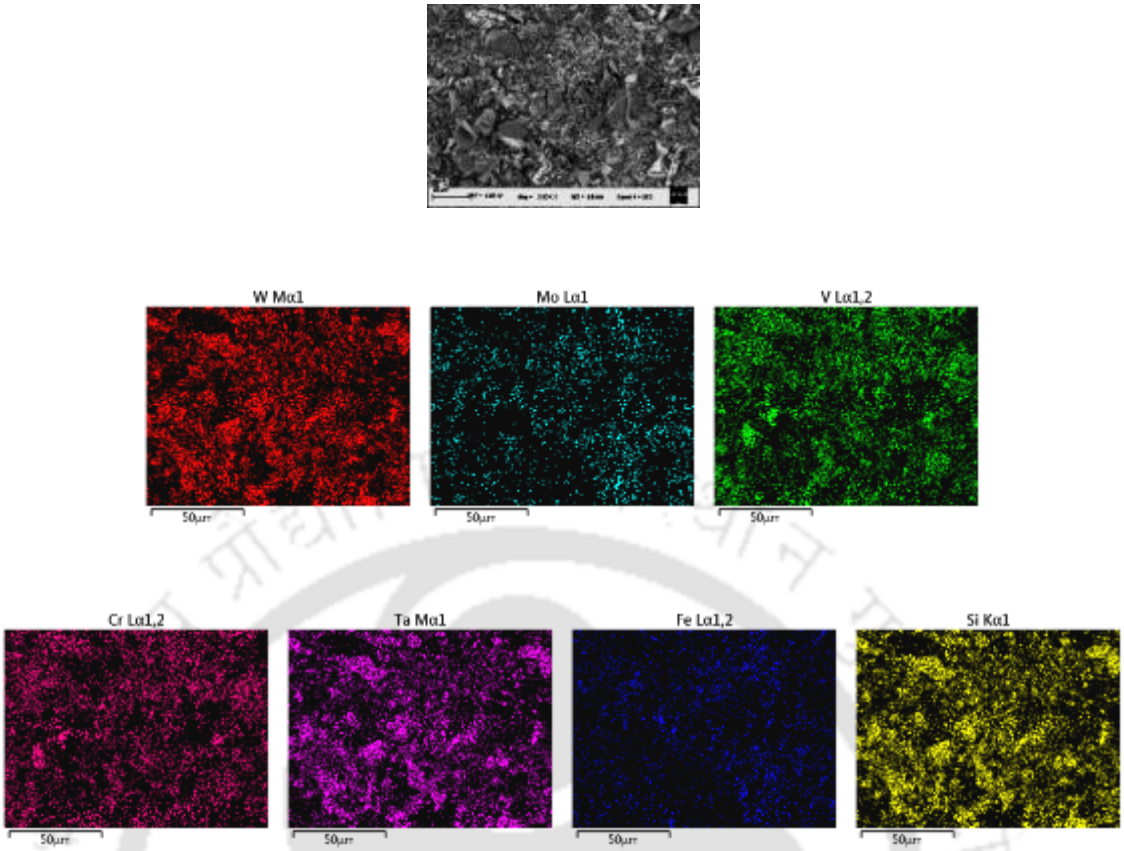

Figure 4. 38 EDS mappings of Figure 4. 1 (a)

Table 4. 13 Quantitative analysis of the marked regions on the SEM images of the wear surfaces and debris of the RHEA of $W_{23}Mo_{23}V_{17}Cr_8Ta_7Fe_{22}$.

Location	W (at. %)	Mo	V	Cr	Ta	Fe	Si
1	5 ±0.3	4 ±0.8	22 ±0.7	49 ±0.5	1 ± 0.3	13 ±0.6	6 ±0.8
2	9 ±0.4	7 ±0.7	21 ±0.6	38 ±0.8	0	12 ±0.5	13 ±0.7

Table 4. 14. Profilometry of the surface of the $W_{23}Mo_{23}V_{17}Cr_8Ta_7Fe_{22}$ alloy after wear by different loads.

		30 N	40 N
3-d view		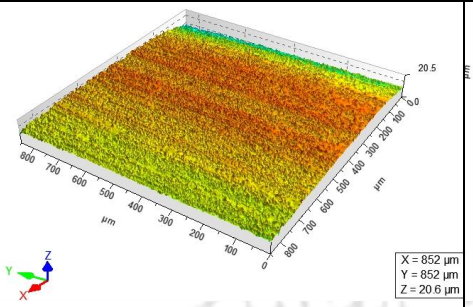	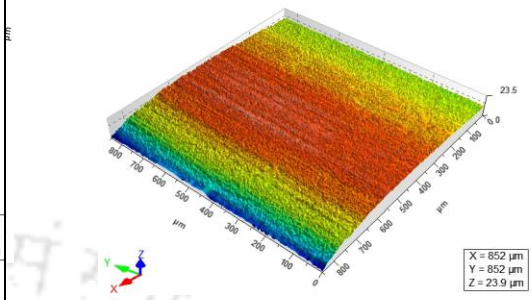
Top -view		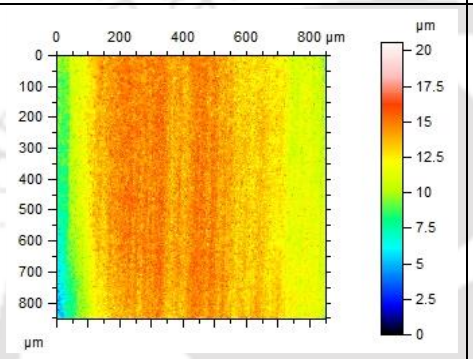	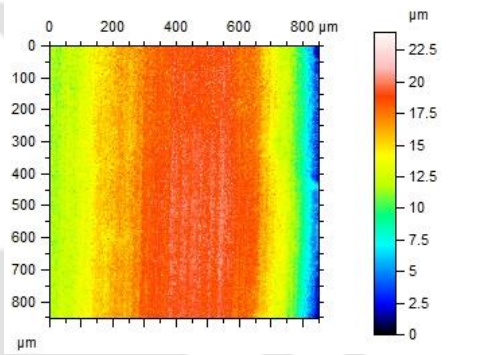
Roughness profile		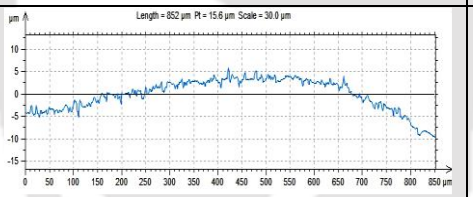	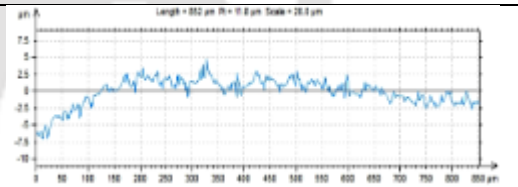
Rough-ness (unit-**µm**)	R_p	1.86	2.66
	R_v	2.00	2.44
	R_z	3.87	5.11
	R_a	0.444	0.614

4.7 Mechanically alloyed $Al_{10}(FeCoNiCu)_{90}$ powder

The powder mixture of $Al_{10}(FeCoNiCu)_{90}$ was mechanically alloyed up to 80 hours by ball milling route to know the extent of alloying. Microstructural characterization and Crystal structure determination of the milled powders were carried out by different techniques and the results are presented and discussed in the subsequent sections.

4.7.1 Particle size analysis

The powder mixtures milled after different hours were analyzed for particle size by Laser particle size analyzer and their cumulative particle size distribution curves are shown in Figure 4.39 (a). From these curves the median particle size (d (0.5)) values were obtained. The median particle size of powders milled for 4, 8, 16, 32 and 80 hours were obtained as 53.6 µm, 45.7 µm, 28.9 µm, 20.3 µm, and 20.6 µm respectively. The milling time vs. median particle size plot is shown in Figure 4.39 (b). The plot shows that the size of the powder particles decreases rapidly till 16 hours of milling. This is due to the high rate of fragmentation of the powder particles at the initial stage of milling [133]. Later the rate of fragmentation was slower from 16 to 32 hours of milling. Small variation in the particle size was observed between 32 hours and 80 hours milled powders due to the saturation of the milling process [133].

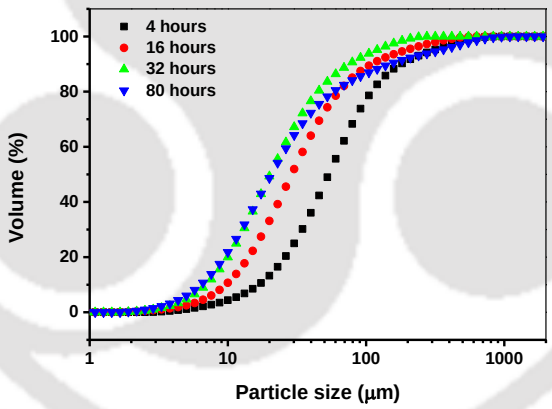

Figure 4. 39. (a) Cumulative Particle size distribution curves of 4, 16, 32 and 80 hours milled $Al_{10}(FeCoNiCu)_{90}$ powder mixtures and (b) Milling time vs median particle size plot of the $Al_{10}(FeCoNiCu)_{90}$ powder mixtures milled after 4, 8, 16, 32 and 80 hours.

4.7.2 SEM analysis

Figure 4.40 shows the SEM micrographs and corresponding EDS analysis of $Al_{10}(FeCoNiCu)_{90}$ powder mixture for (a) 8 hours, (b) 32 hours and (c) 80 hours of milling.

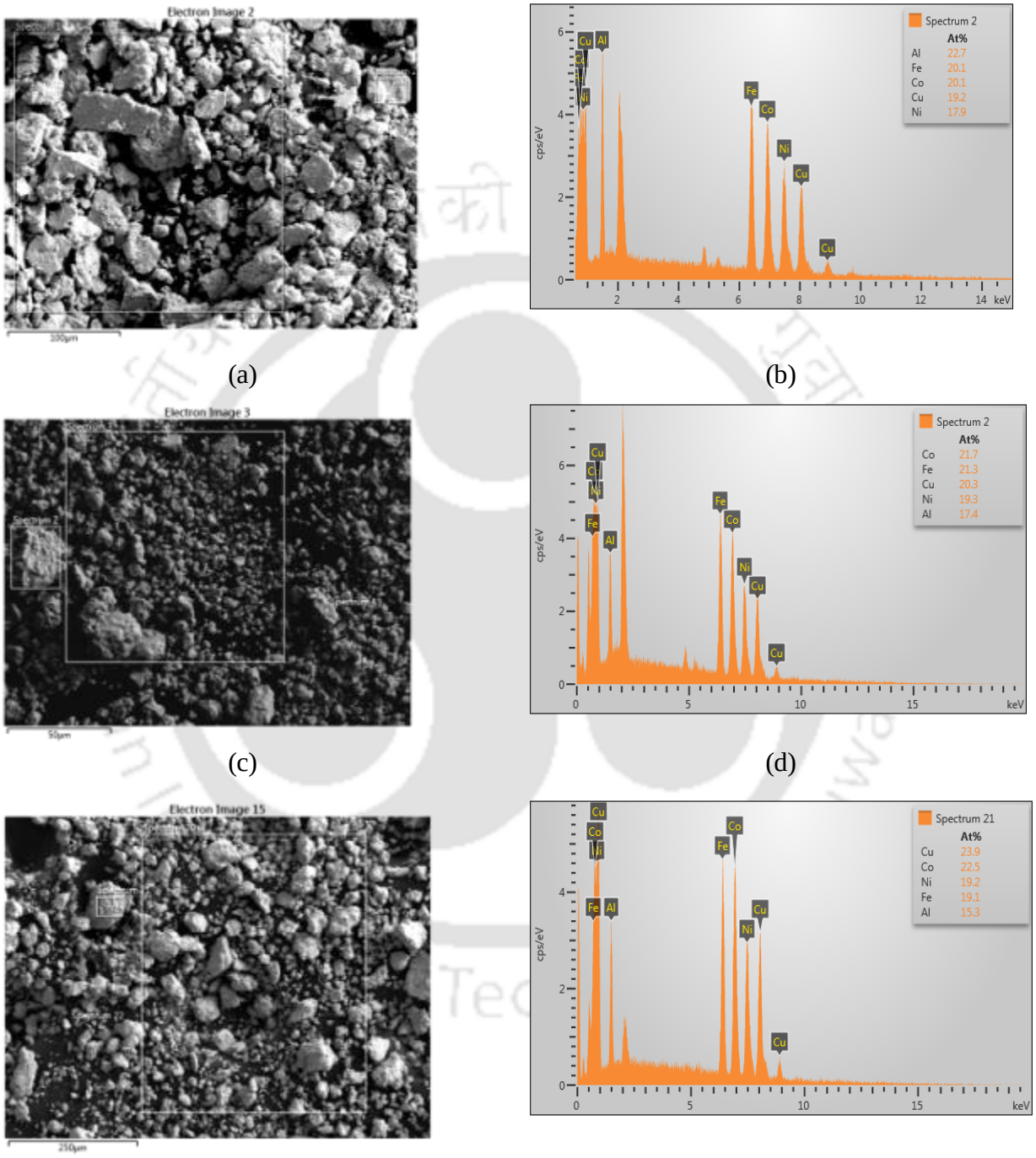

Figure 4. 40. SEM micrographs and corresponding EDS analysis of $Al_{10}(FeCoNiCu)_{90}$ powder mixture for (a) 8 hours, (b) 32 hours and (c) 80 hours of milling.

The EDS result indicates that the atomic percentages of the elements in the 80 hours milled powder mixture are nearly equal to that of the starting powder mixture. The EDS mapping result of the powder mixture after milling for 80 hours is shown in Figure 4.41. The result indicates a homogeneous distribution of all the constituent elements in the powder mixture. The concentration of Al in the mapping result is seen to be lesser than other elements due to the less addition of the Al powder (10 at.%) in the starting powder mixture.

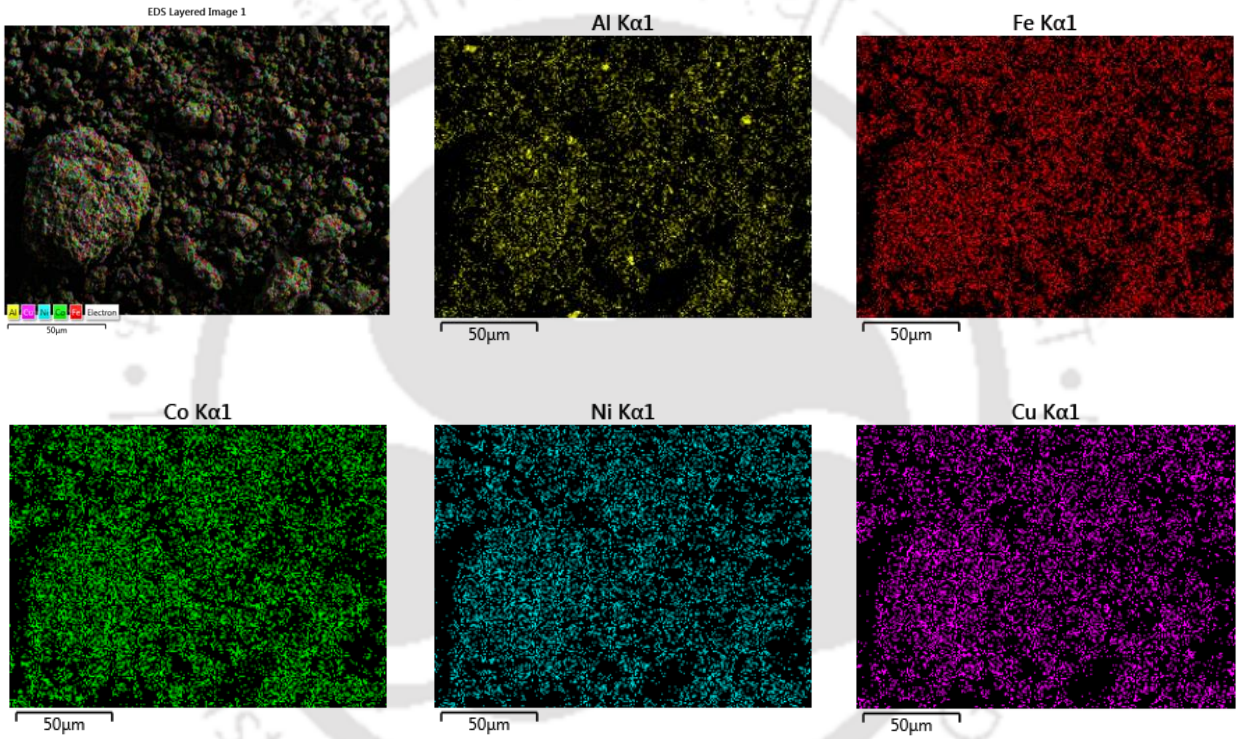

Figure 4. 41. Energy Dispersive Spectroscopy (EDS) map of 80 hours milled $Al_{10}(FeCoNiCu)_{90}$ powder.

4.7.3 XRD analysis

The powder mixtures milled for various hours were analyzed for crystal structure by XRD technique and their patterns are shown in Figure 4.42. The XRD patterns for the starting powder mixture (0 hours milled) show sharp peak intensities corresponding to the reflections from the planes of Al, Fe, Co, Ni and Cu. At the initial stage of milling, from 4 hours to 16 hours, the peak intensity of Ni was increased and all other elemental peak intensity were decreased which indicates that the elemental peaks merge into Ni peaks. After 32 hours of milling, the Ni peaks

shifted to the lower angle indicating lattice expansion in Ni. Due to progressive milling, more elements accommodate into basic Ni lattice which has close packed FCC structure, hence causing lattice expansion.

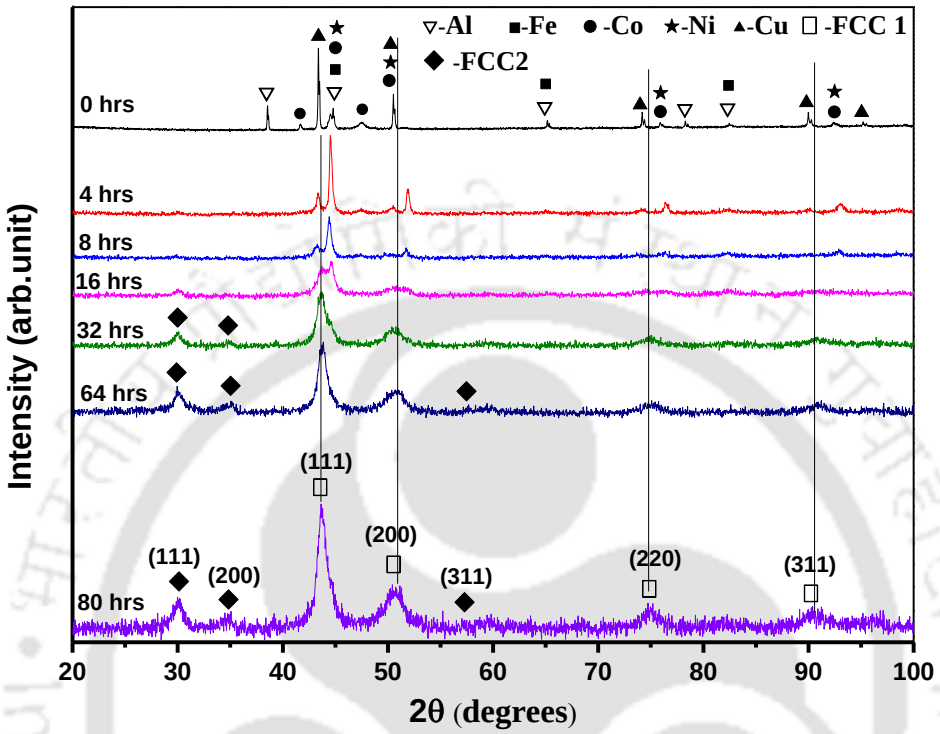

Figure 4. 42. XRD patterns of the $Al_{10}(FeCoNiCu)_{90}$ powder.

The XRD peak position analysis of 32 hours milled powder confirms two different FCC phases as their peak patterns are in accordance with the standard FCC peak pattern. The two phases are named as FCC1 and FCC2 shown in Figure 4.42. FCC phases were formed in the milled powder due to the quantity of Al added, i.e. 10 atomic % in the starting powder mixture [5]. Milling duration was extended up to 80 hours to get more homogeneous and single phase mixture but FCC2 phase was still retained after 80 hours of milling and became more prominent. The phase fractions of FCC1 and FCC2 phases from the XRD pattern of 80 hours milled powder were calculated to be 72% and 18% respectively. After 64 hours and 80 hours of milling, only peak broadening was observed in FCC peaks without any peak shift. After 80 hours of milling, the inter-planar spacings determined for the FCC1 phase corresponding to the reflection from the

planes of (111), (200), (220) and (311) were 2.06 Å, 1.81 Å, 1.27 Å and 1.09 Å respectively. The lattice parameter of the FCC1 phase was obtained as 3.60 Å. The inter-planar spacings obtained after milling for 80 hours for the FCC2 phase corresponding to the reflection from the planes of (111), (200) and (311) were 2.98 Å, 2.58 Å and 1.60 Å respectively. The lattice parameter of the FCC2 phase was obtained as 5.21 Å.

4.7.4 TEM analysis

Figure 4.43 shows (a) Bright Field TEM image, (b) Dark Field TEM image and (c) SAED patterns of the marked particle in bright and dark field images (d) HRTEM image, and (e) IFFT image and corresponding line profile of the selected region in HRTEM image in 80 hours milled $Al_{10}(FeCoNiCu)_{90}$ powder. In the bright field TEM image the regions with heavier atoms were seen darker as the heavier atoms scatter electrons more intensely than lighter atoms. In the dark field TEM image the regions with heavier atoms were brighter. The powder samples were strongly diffracted as they appear darker in the bright field mode and brighter in the dark field mode; hence the milled powders are more crystalline. The bright spots in the concentric rings of the SAED patterns also indicate that the powder is polycrystalline. The SAED patterns were analyzed using ImageJ software for indexing the rings. Two FCC phases were confirmed from SAED analysis. Four rings were identified as corresponding to the (111), (200), (220) and (311) planes of the FCC1 phase. Two rings were also identified as (111), (200) planes of the FCC2 phase whose d values are given in next paragraph. The inter-planar spacings for (111), (200), (220) and (311) planes of FCC1 phase obtained by TEM analysis are 2.10Å, 1.76Å, 1.27Å and 1.11Å respectively. The corresponding inter-planar spacings for (111), (200), (220) and (311) planes of FCC1 phase obtained from XRD analysis were 2.06Å, 1.81Å, 1.27Å and 1.09Å respectively. SAED analysis revealed the lattice parameter of the FCC1 phase as 3.589Å of the 80 hours milled powder. Similar lattice parameter (3.60 Å) for the FCC1 phase was also obtained from XRD analysis. The HRTEM image in Figure 4.43 (d) shows that the inter-planar

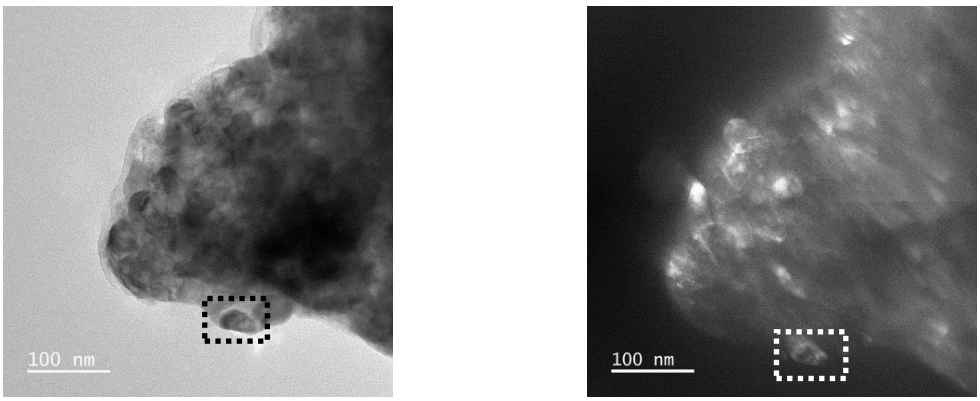

(a) (b)

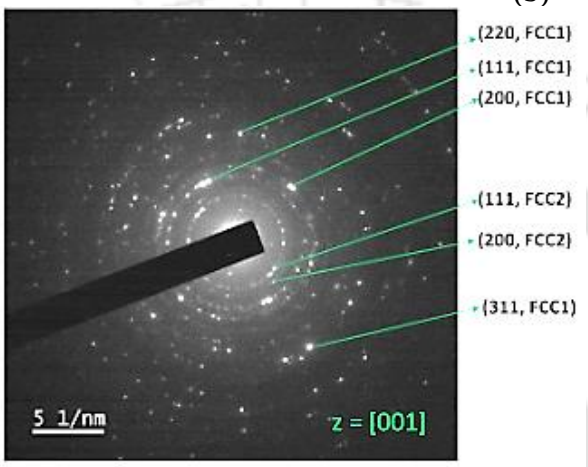

(c)

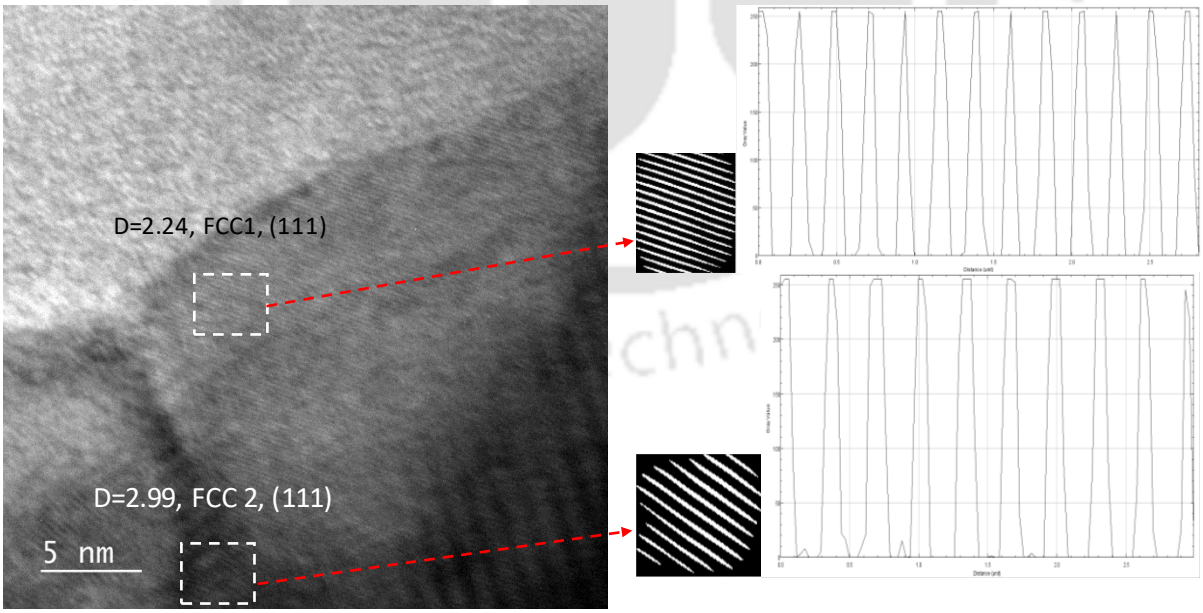

(d) (e)

Figure 4.43 (a) Bright Field TEM image, (b) Dark Field TEM image and (c) SAED patterns of the marked particle in bright and dark field images (d) HRTEM image, and (e) IFFT image and corresponding line profile of the selected region in HRTEM image in 80 hours milled $Al_{10}(FeCoNiCu)_{90}$ powder.

spacing is 2.24 Å, hence it corresponds to (111) plane of the FCC1 phase as the result is coincident with above SAED results.

The inter-planar spacings for (111) and (200) planes of the FCC2 phase obtained by SAED analysis are 3.02Å and 2.61Å respectively. The corresponding inter-planar spacings for (111) and (200) planes of the FCC2 phase obtained from XRD analysis were 2.98Å and 2.58Å respectively. SAED analysis revealed the lattice parameter of the FCC2 phase as 5.22Å for 80 hours milled powder. Similar lattice parameter (5.21 Å) for the FCC2 phase was also obtained from XRD analysis. Hence the XRD results are in well agreement with the TEM results. The HRTEM image in Figure 4.43 (d) shows that the inter-planar spacing is 2.99 Å, hence it corresponds to (111) plane of the FCC2 phase as the result is coincident with above SAED results. The above results confirm that both FCC1 and FCC2 crystals are adjacently present in a single nanoparticle.

4.8 Arc melted $Al_{10}(FeCoNiCu)_{90}$ alloy

The alloy powder of $Al_{10}(FeCoNiCu)_{90}$ was consolidated by cold compaction and subsequent sintering to fabricate the alloy ingots. The following section shows the characterization of such ingots by illustrating their structure (crystal structure and microstructure) and properties (mechanical and tribological) investigated by various techniques.

4.8.1 SEM and EDX analysis

The SEM micrograph of the $Al_{10}(FeCoNiCu)_{90}$ alloy ingot is shown in Figure 4.44 (a). The magnified image of the rectangular portion in the SEM micrograph is shown in Figure 4.44 (b) that indicates the spinodal decomposition (white) on the parent phase (black). The figure also shows that the spinodal decomposition is appeared evenly in entire region of the alloy ingot. The spinodal phase is regarded as the phase with small difference in composition but must contain similar crystal structure as that of the parent phase [93].

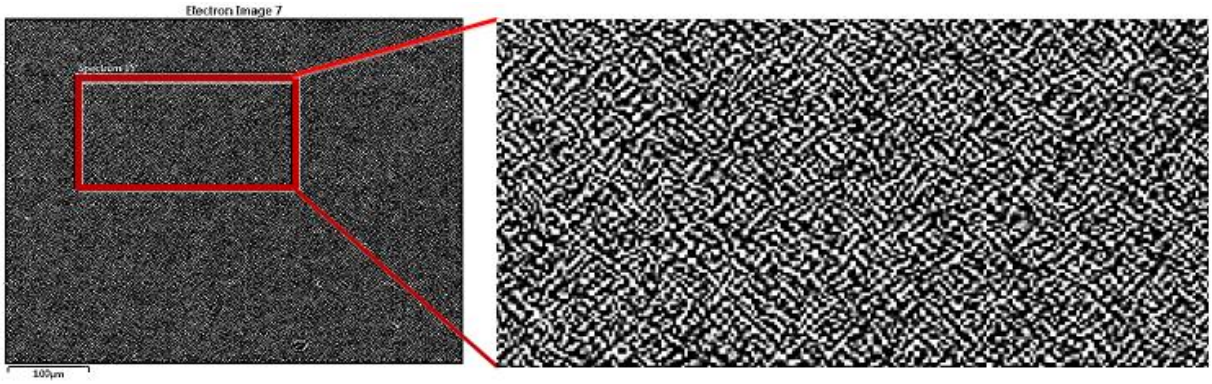

(a) (b)

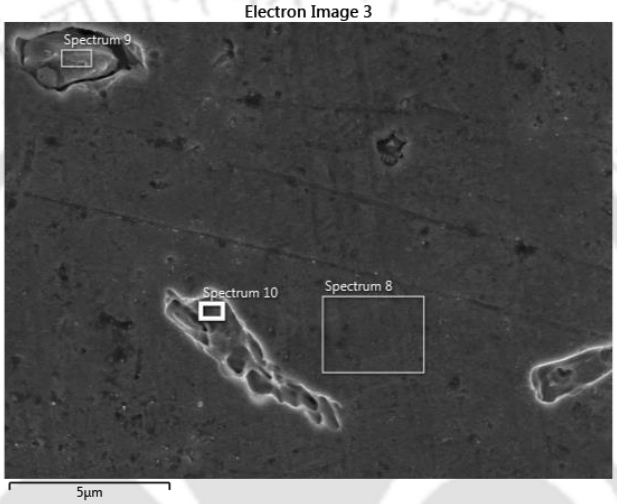

(c)

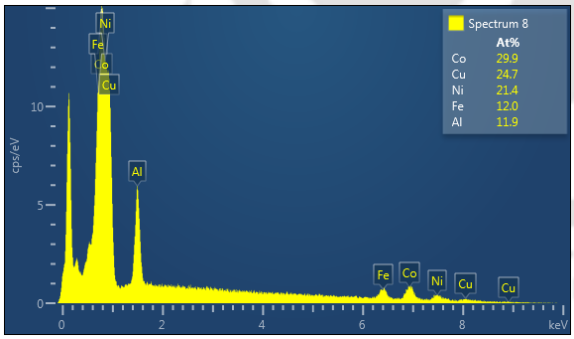

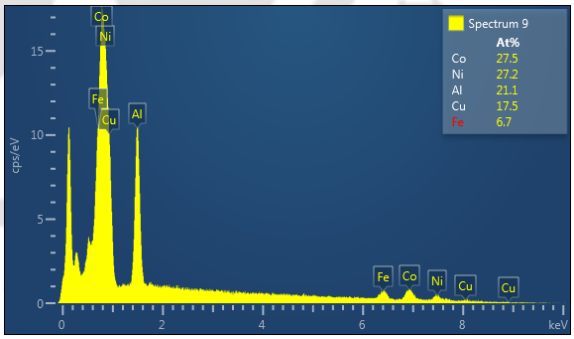

(d) (e)

Figure 4. 44. (a) SEM micrograph by SE2 mode, (b) magnified image of the rectangle portion in the SEM micrograph, (c) High magnification SEM micrograph by In-Lens mode, and (d and e) EDS analysis of the high magnification SEM micrograph of the alloy ingot.

The high magnification SEM image is shown in Figure 4. 44 (c) and the corresponding EDS analysis are shown in Figure 4.44 (d) and (e) that determines the composition of the spinodal and parent phases. The chemical compositions of those phases (by taking average of 5 readings) in the alloy ingot of $Al_{10}(FeCoNiCu)_{90}$ are shown in the Table 4.15. The atomic % of Co in the spinodal and the parent phases are almost equal. The atomic % of Fe in the spinodal phase is quite lower than that of the parent phase.

Table 4. 15. Chemical composition of different phases in the alloy ingot.

Phases	Co (at. %)	Cu (at. %)	Ni (at. %)	Fe (at. %)	Al (at. %)
Parent	30 ±0.7	25 ±0.8	21 ±0.5	12 ±0.7	12 ±0.9
Spinodal	28 ±0.5	18 ±0.7	27 ±0.7	6 ±0.2	21 ±1.1

4.8.2 XRD analysis

XRD pattern of the $Al_{10}(FeCoNiCu)_{90}$ alloy ingot is shown in Figure 4.45. XRD analysis could reveal only a single FCC crystal structure for the alloy ingot. This is due to the spinodal decomposition on the parent phase. The spinodal phase mostly possesses analogous crystal structure as that of the parent phase [93]. The lattice parameter of the spinodal phase may be very similar to the parent phase for which the peaks get overlapped and could not be distinguished in XRD analysis. A similar result was also seen in $Al_{0.4}CoCrCuFeNi$ HEA where the cast alloy revealed two FCC phases with very similar lattice parameters [24]. In the present alloy, except Cu-based binary pairs, all other constituent binary pairs have small enthalpy of mixing and excellent mutual solid solubility [31]. Hence initial ball milling led to the preliminary diffusion of Cu with other powder particles by maximizing the contact and diffusion areas between particles and enhanced the solid solubility of Cu with other elements that aided to

form FCC phase in the alloy ingot without forming any elemental rich (example: Cu-rich or Al-rich) intermetallic or compound phases [22, 93, 134].

Five apparent FCC peaks were obtained in the XRD pattern of the alloy ingot shown in Figure 4.45. The inter-planar spacings corresponding to the reflections from the planes of (111), (200), (220) (311) and (222) of the FCC lattice are 2.09Å, 1.81Å, 1.28Å, 1.09Å and 1.04Å respectively. The lattice parameter of the corresponding FCC phase was found to be 3.66 Å. However, the lattice parameter of the FCC1 phase of the 80 hours milled powder obtained from the XRD analysis was 3.60 Å. Hence slight lattice expansion was evident in the alloy ingot due to the internal stress release of the crystal lattice of the milled powder after sintering [5, 93].

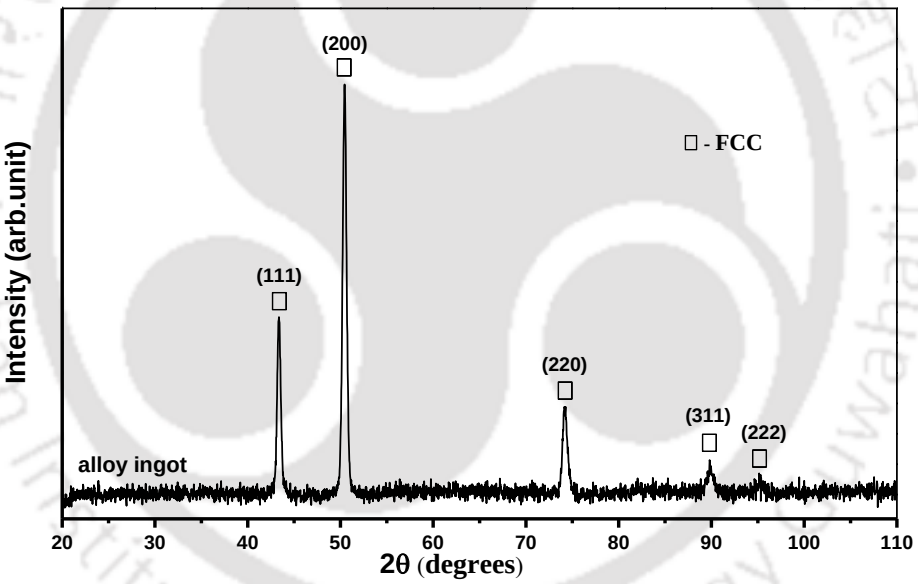

Figure 4. 45. XRD analysis of the $Al_{10}(FeCoNiCu)_{90}$ alloy ingot.

4.8.3 Mechanical properties

The uni-axial compression test of the cylindrical samples cut from the alloy ingots were performed at room temperature. The engineering compressive stress-strain graph is shown in Figure 4.46. From the graph, the 0.2% offset yield stress of the sample was achieved as high as 308 ± 17 MPa. The compressive stress at 40% strain of the sample was obtained as 1406 ± 38 MPa. During fabrication of the alloy ingot, atoms of each constituent elements act as solute

which randomly acquires different lattice sites in a crystal lattice. Different atoms in a lattice have different sizes and thus lattice are strained which results in the lattice distortion [5]. The Al atom has the largest atomic diameter among all the constituent atoms in the present alloy ingot that makes the lattice of the alloy severely distorted. Different bonding energies among atoms of different constituents also add distortion in the crystal lattice of the HEA [5]. High strength is hence due to solid solution strengthening as severe distortion occurs in alloy lattice due to big Al atoms (metallic radii is highest= 143pm), which as a result inhibits dislocation movement [5]. During compression test, the sample finally turned to a coin shape without any failure, indicating high ductility.

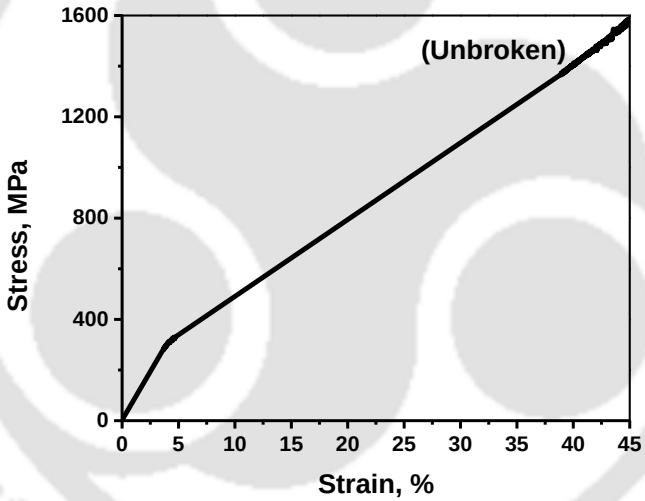

Figure 4. 46 Engineering compressive stress-strain curve of the $Al_{10}(FeCoNiCu)_{90}$ alloy.

The overall hardness of the alloy ingot was obtained by taking the average Vickers hardness result of 10 readings with a load of 500 gram-force for 15 seconds and the corresponding value is 160 ± 14 $HV_{0.5}$. The density of the alloy ingot was measured by the Archimedes principle by taking water as a medium and the corresponding value is 7.7 g/cm^3.

4.8.4 Tribological properties

The plots of wear vs. sliding distance of the $(Al)_{10}(FeCoNiCu)_{90}$ at 30 N and 40 N loads are shown in Figure 4.47 (a). The wear depth of the alloy increased almost linearly with the

increase in sliding distance for both loading conditions. After 300 meters of sliding, the calculated total wear volume of the alloy at 40 N load was nearly 2 times higher than that at 30 N. The wear coefficients of the alloy at 30 N and 40 N loads are shown in Figure 4.47 (b). The figure indicates that the wear coefficient at 40 N is 1.07 times higher compared to that at 30 N.

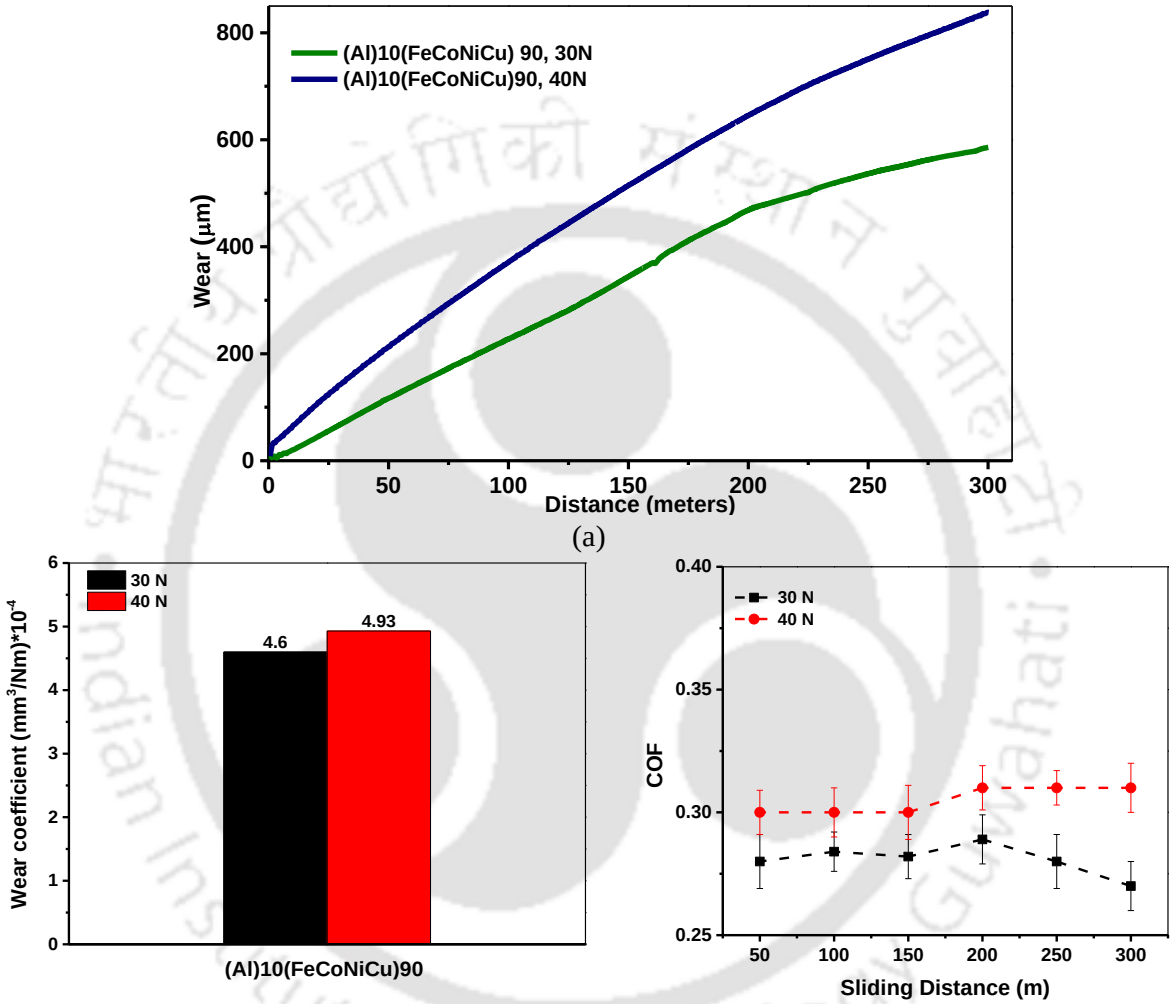

Figure 4. 47 (a) Wear vs. sliding distance, (b) Wear Coefficient and (c) Coefficient of Friction vs. sliding distance plots of the $(Al)_{10}(FeCoNiCu)_{90}$ RHEA at the loads of 30N and 40 N.

Figure 4.47 (c) shows the plots of COF vs. sliding distance of the alloy at the loads of 30 N and 40 N. The figure indicates higher COF at higher load. The average values of COF at 30 N and 40 N are 0.28 ± 0.009 and 0.31 ± 0.010 respectively. The slope of the C.o.F curve of the HEA at 30 N load decreased continuously after the sliding distance of 200 meters. This decrease in slope occurs due to the decrease in the surface roughness on progressive sliding [134]. Hence,

the surface became smoother on sliding after 200 meters. This smoothening is due the sufficient amount of the formation of lubricating debris at that period. The debris acts as solid lubricant by sticking on the abrasive surface that passivate the contact surfaces and reduce the friction [134]. This enhances the smoothening of the alloy surface. At 40 N the slope of the COF curve of HEA almost remained constant after 200 meters. Hence though the smoothening of the alloy was not occurred after 200 meters due to high load, the roughening of the alloy was hindered. This is also due to the sufficient amount of the formation of lubricating debris.

SEM image of the worn surface of $(Al)_{10}(FeCoNiCu)_{90}$ alloy shown in Figure 4.48 reveals wear groove tracks formed by the ploughing action by the abrasives. Wear grooves were more intense on the surface worn by 40 N than that by 30 N indicating more wear on that surface. The wear tracks are shown by dashed arrows in the figures. The tracks were mostly continuous due to low hardness of the alloy [93] as compared to SiC. The wear directions are shown by solid arrow lines in the figure. The EDX image of spectrum 29 is shown in Figure 4.48 (c). The image indicates that the oxygen spectrums are not evident hence the alloy surface was not oxidized after wear.

The SEM images of the debris collected after the test at different loads are shown in Figure 4.49 (a) and (b). The EDX analysis at spectrum 6 in Figure 4.49 (b) is shown in Figure 4.49 (c). The figure indicates that the five elements of $(Al)_{10}(FeCoNiCu)_{90}$ alloy are present in the debris with high amount of Si. The Si was identified due to the presence of SiC particles in the debris. These SiC particles emerged from the SiC abrasive by fracturing abrasive tips during wear test. The X-ray elemental mapping of the Figure 4.49 (b) is shown in Figure 4.50. The mapping also shows the presence of Si.

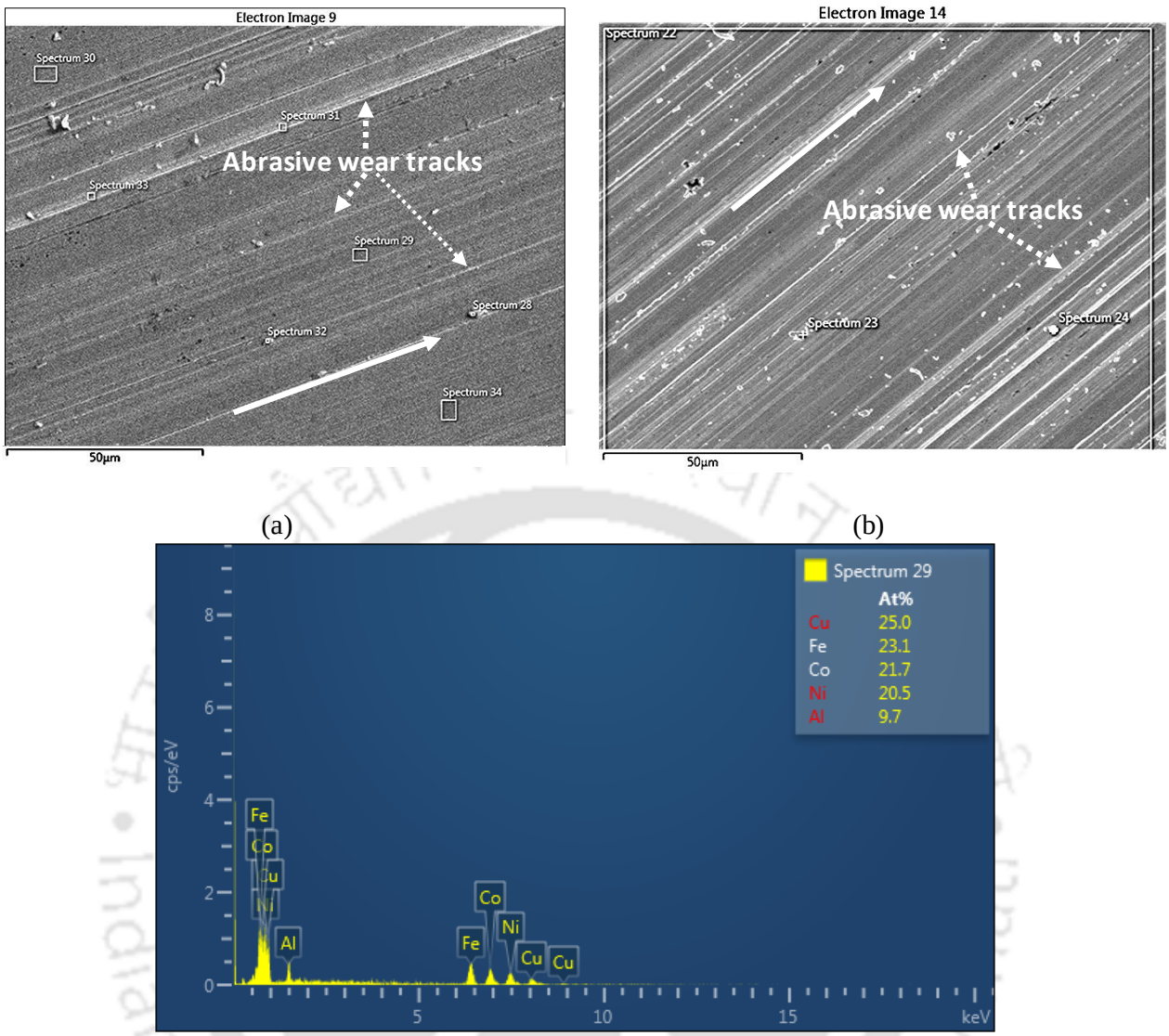

Figure 4. 48 SEM micrographs of the $(Al)_{10}(FeCoNiCu)_{90}$ alloy worn by (a) 30 N and (b) 40 N loads; (c) EDX image of spectrum 29 in Figure 4.48 (a)

The three-dimensional (3-d) morphology and their corresponding top views of the surfaces worn at 30 N and 40 N are depicted in Table 4.16. The roughness profiles of the corresponding traced surfaces are shown below the top view images. The measures of roughness viz, R_p, R_v, R_z and R_a as per 'ASME B 46.1' are also presented in the table. Here Ra is the roughness average, R_p is the height of the highest profile peak, R_v is the depth of the deepest profile valley, P_t is the profile depth which is the sum of the largest profile peak height and the largest profile valley depth of the P profile within the evaluation length and R_{zi} is the single roughness depth and is determined as $R_{zi} = R_p + R_v$. Mean roughness depth R_z is the arithmetic

mean value of the single roughness depths, i.e $R_z = \frac{1}{n}(R_{z1} + R_{z2} + R_{z3}\ldots\ldots R_{zn})$. The R_z values at 30 N and 40 N were 5.02 microns and 5.40 microns respectively. The R_a values at 30 N and 40 N were 0.676 and 0.766 microns respectively indicating that the surface roughness average of the RHEA worn at 40N load is ~ 13% higher than that at 30N.

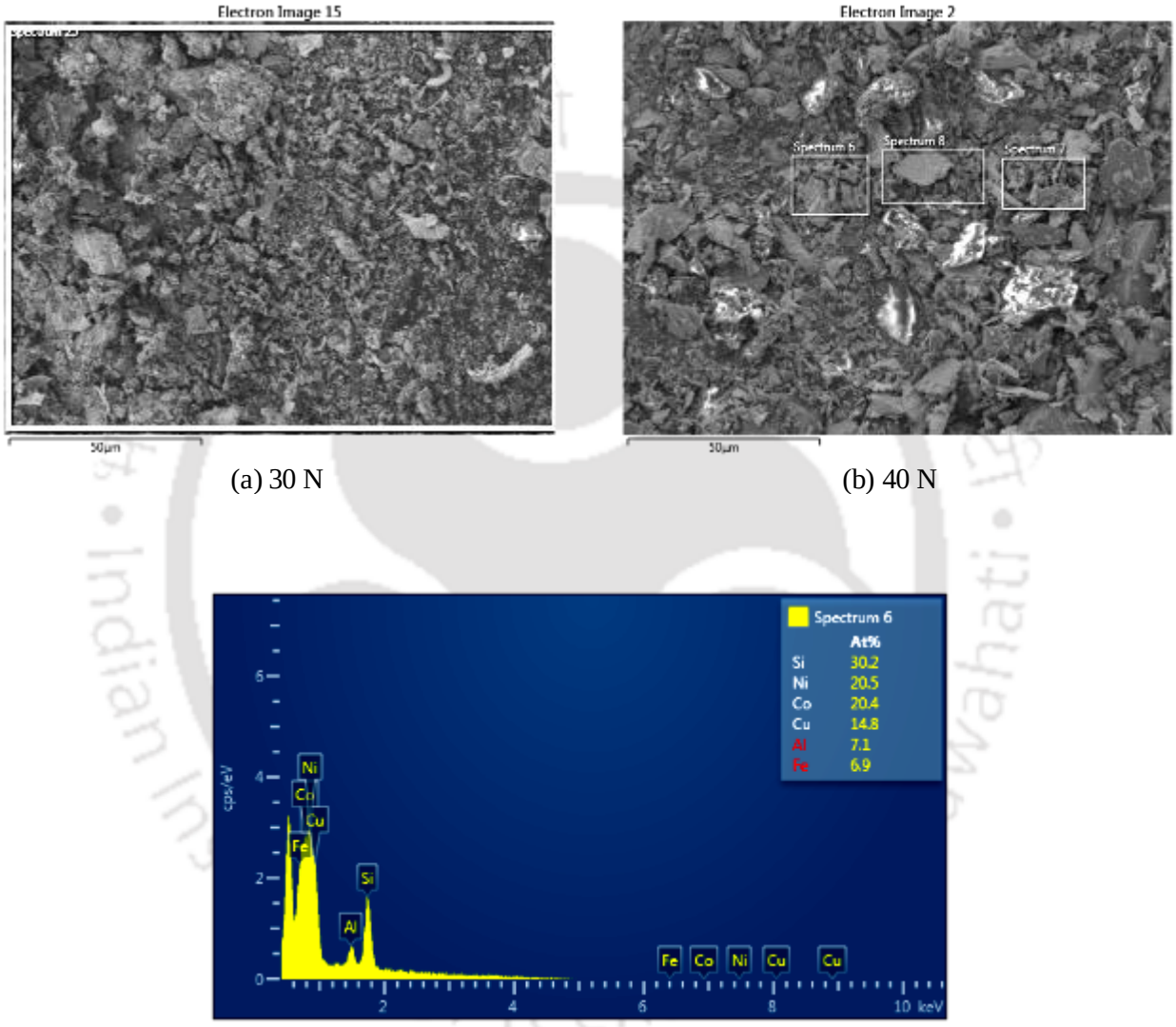

(a) 30 N (b) 40 N

(c)

Figure 4. 49 SEM images of the debris of the $(Al)_{10}(FeCoNiCu)_{90}$ worn by loads of (a) 30 N and (b) 40 N and (c) EDX image of spectrum 6 in the SEM image

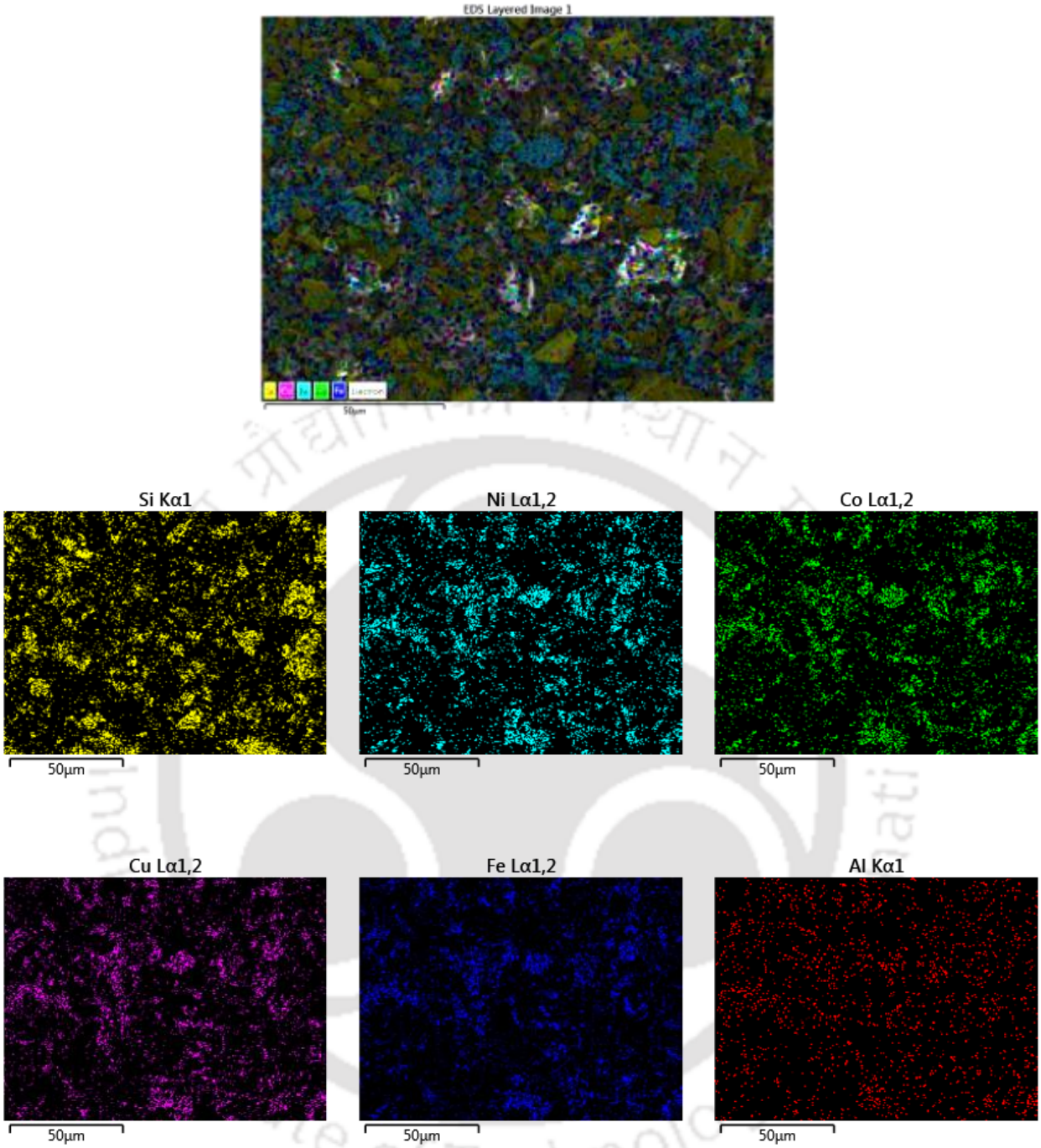

Figure 4. 50 EDX mapping of Figure 4. 2 (b)

Table 4. 16 Topography of the surface of the $(Al)_{10}(FeCoNiCu)_{90}$ worn by various loads.

		30 N	40 N
3-d view		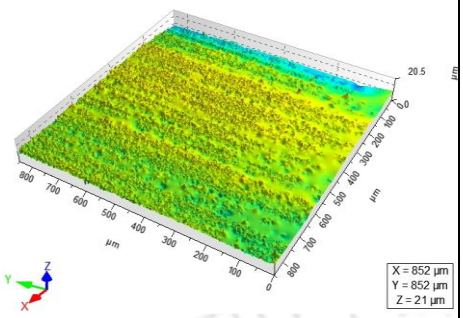	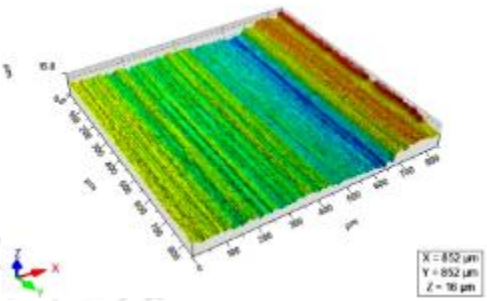
Top -view		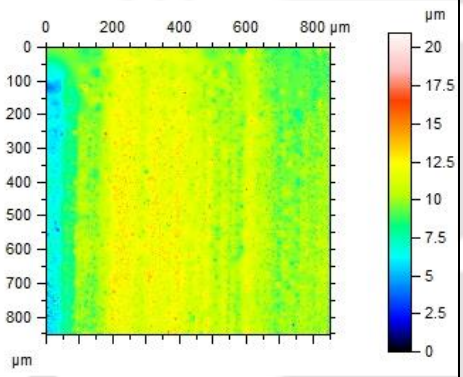	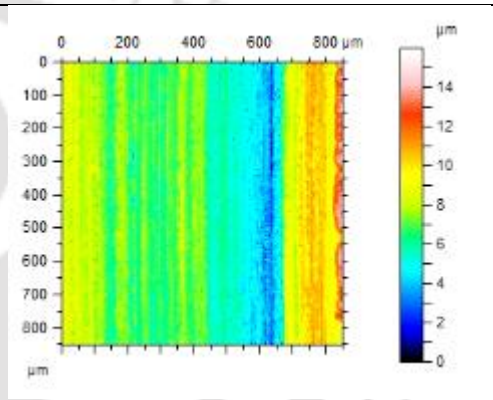
Roughness profile		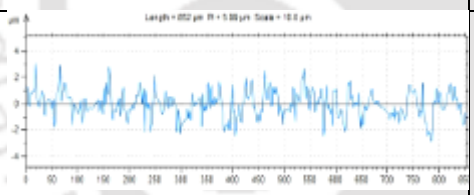	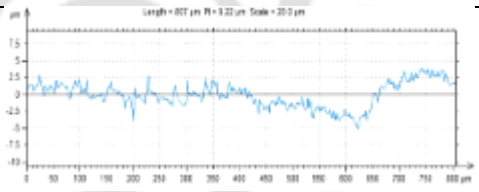
Rough-ness Table (unit-µm)	R_p	2.66	2.36
	R_v	2.35	3.13
	R_z	5.02	5.40
	R_a	0.676	0.766

4.9 Comparison of tribological properties between HEAs and HSS

Figure 4.51 shows (a) Wear vs. Sliding distance plots of RHEAs and HSS, (b) Wear vs. Sliding distance plots of all HEAs and HSS, (c) Wear Volume vs. Sliding distance plots of All HEAs and HSS, (d) Wear volume vs. Sliding Distance plots of RHEAs and HSS, and (e) COF vs. Sliding Distance plots of all HEAs and HSS. The average values of COF at 30

N and 40 N for HSS are determined as 0.34 ± 0.009 and 0.31 ± 0.010 respectively. The wear coefficients of HSS at 30 N and 40 N are determined as 0.917 and 0.835 respectively.

In WMoVCrTa, for 40 N, COF plot is in lower zone (Figure 4. 51 (e)) but Wear Volume is in upper zone (Figure 4. 51 (d)). This means though COF for the HEA is less, the wear is high. COF is the inherent property of the alloy. It is directly proportional to wear mostly. But it also depends on surface morphology such as delamination of the surface due to micro cracks, surface roughness, holes, defects etc. The micro cracks were detected in microscopy of the alloy surface worn at 40 N load which caused the high wear.

But in WMoVCrTa, for 30 N, both COF and Wear Volume plots are in lower zone. This is due to (a) high hardness of the HEA and (b) no crack surface formation while wear at 30 N load. The second reason is more vital for reducing the wear of the HEA.

In W23Mo23V17Cr8Ta7Fe22, for both 30 N and 40 N, COF plot is in upper zone but Wear Volume is in lower zone. This means there should be more wear as COF is higher. But this has not happened which is attributed to the highest hardness and strength of the corresponding HEA among all the three HEAs. The more the hardness and strength, the more is the wear resistance of the material. Also, no cracks were found for this HEA after wear at both the loads which aids in less wear.

COF vs. distance plots for RHEAs also revealed that the initial slopes of COF curves at both 30 N and 40 N are higher than that at later stage. This is mainly due to the higher surface roughness at initial stage which is due to insufficient formation of lubricating debris. The wear volume is less at initial period that results in small and insufficient amount of lubricating debris. Sufficient amount of lubricating debris fills up the regions in between the asperities and reduce their amount resulting in reduction in the surface roughness. This slows down the rate of increase of COF at later stages in the continuous wear process.

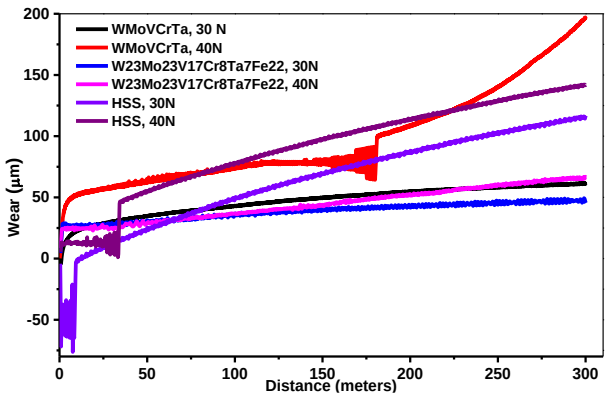

(a)

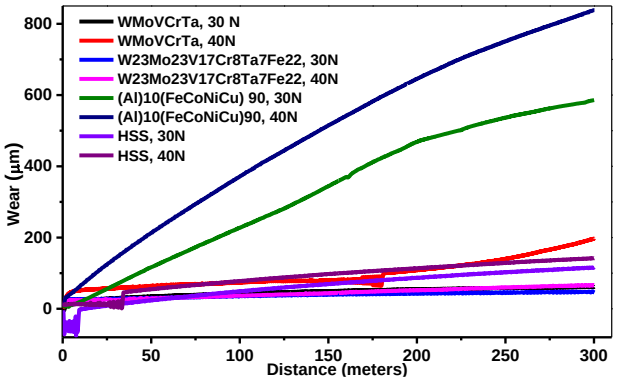

(b)

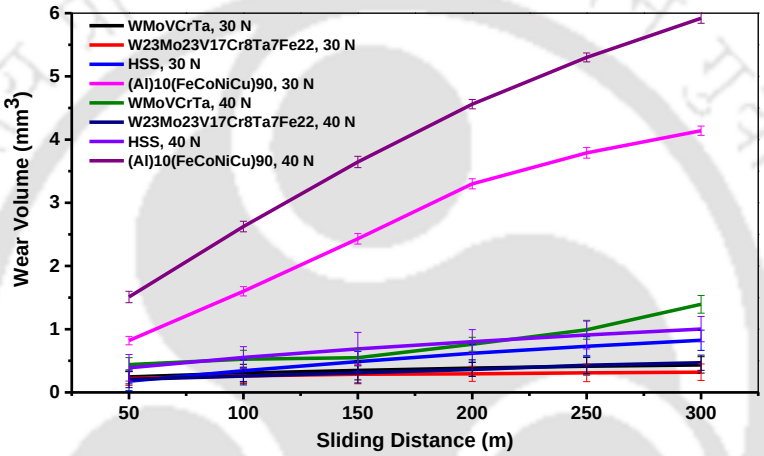

(c)

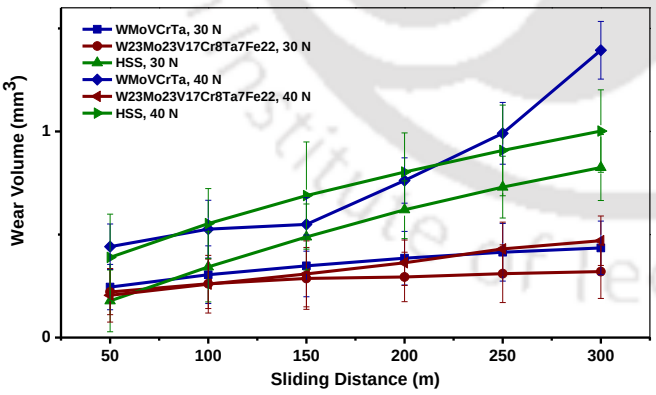

(d)

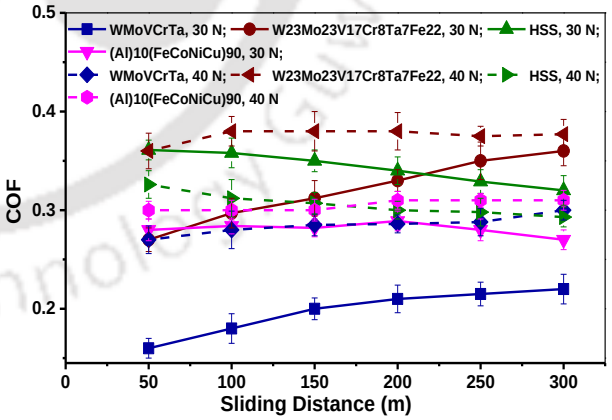

(e)

Figure 4. 51 (a) Wear vs. Sliding distance plots of RHEAs and HSS, (b) Wear vs. Sliding distance plots of all HEAs and HSS, (c) Wear Volume vs. Sliding distance plots of All HEAs and HSS, (d) Wear volume vs. Sliding Distance plots of RHEAs and HSS, and (e) COF vs. Sliding Distance plots of all HEAs and HSS

The wear coefficients of WMoVCrTa, $W_{23}Mo_{23}V_{17}Cr_8Ta_7Fe_{22}$, $(Al)_{10}(FeCoNiCu)_{90}$ and HSS at 30 N and 40 N loads are shown in Figure 4.52. The figure indicates higher wear coefficients at 40 N compared to that at 30 N for the three HEAs. The wear coefficient of WMoVCrTa is 1.9 times less than that of HSS at 30 N load. The wear coefficients of $W_{23}Mo_{23}V_{17}Cr_8Ta_7Fe_{22}$ are 2.5 and 2.1 times less than that of HSS at 30 N and 40 N load respectively. Hence, the two RHEAs have higher wear resistance than that of HSS as their wear coefficients are less as compared to HSS. However, the wear coefficients of $(Al)_{10}(FeCoNiCu)_{90}$ are 5.1 and 5.9 times higher than that of HSS at 30 N and 40 N load respectively. The wear coefficients of $W_{23}Mo_{23}V_{17}Cr_8Ta_7Fe_{22}$ are also lower than that of WMoVCrTa at respective loads indicating that the $W_{23}Mo_{23}V_{17}Cr_8Ta_7Fe_{22}$ has better wear resistance as compared to WMoVCrTa. This is due to the higher hardness of $W_{23}Mo_{23}V_{17}Cr_8Ta_7Fe_{22}$ (800 ± 20 HV) than that of WMoVCrTa (773 ± 20 HV) [23, 132] and crack free surfaces. The $W_{23}Mo_{23}V_{17}Cr_8Ta_7Fe_{22}$ RHEA also exhibited better compressive strength than that of the WMoVCrTa [23, 132]. The more the hardness and strength, the more is the wear resistance of the material [127].

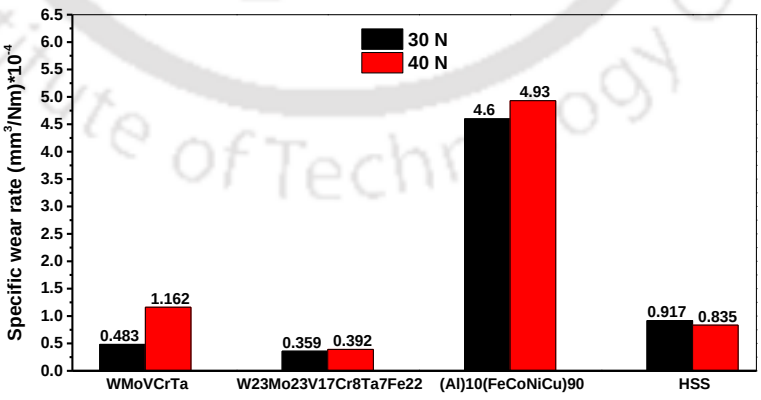

Figure 4. 52 Comparison of wear coefficients between HEAs and HSS at the loads of (a) 30N and (b) 40 N

Chapter 5

Conclusions and Future Scope of the Work

5.1 Conclusions

In this research work, two types of alloys were designed and fabricated. They are:

- Two refractory HEAs : WMoVCrTa and $W_{23}Mo_{23}V_{17}Cr_8Ta_7Fe_{22}$
- One transition metal HEA : $Al_{10}(FeCoNiCu)_{90}$

The RHEAs were fabricated by ball milling + arc melting + heat treatment techniques. The transition metal HEA was prepared by ball milling + sintering techniques. The extent of milling of three alloy powders was determined. The structure and mechanical properties of the alloy ingots were investigated. The tribological properties of the alloys were also determined. The main findings obtained from the work are as follows:

- The combination of five refractory elements in equiatomic ratio, i.e. the WMoVCrTa alloy satisfies the Guo et al.'s criteria, and all three above alloy combinations satisfy Takeuchi et al.'s criteria to form solid solution phases by inhibiting the formation of BMGs.
- A major BCC1, a minor BCC2 and an intermetallic phase were identified in the WMoVCrTa powder mixture after 64 hours of milling and heat treatment. The lattice parameter of those BCC1 and BCC2 phases were 3.162 Å and 2.90 Å respectively.
- The arc melted alloy (ingot) of WMoVCrTa resulted in three different phases such as $W_{38}Mo_{35}Ta_9Cr_6V_{12}$, $W_4Mo_3V_{20}Cr_{19}Ta_{54}$ and $W_9Mo_{24}V_{21}Cr_{28}Ta_{18}$ with phase fractions of 86%, 4% and 9% respectively.
- XRD analysis of the WMoVCrTa alloy ingot reveals the above phases as major BCC1 ($W_{38}Mo_{35}Ta_9Cr_6V_{12}$), minor BCC2 ($W_9Mo_{24}V_{21}Cr_{28}Ta_{18}$) and minor intermetallic

($W_4Mo_3V_{20}Cr_{19}Ta_{54}$) phase. The lattice parameters of these BCC1 and BCC2 phases were 3.05 Å and 2.85 Å respectively.

- The WMoVCrTa alloy exhibited high strength and good yield strain at room and elevated temperatures. The alloy has the room temperature compressive yield stress of 995 MPa at a yield strain of 6.2 %. Yield strength retention at 1000 °C is ~79% of the room temperature value in the alloy.
- At 1200 °C, a yield stress anomaly was observed in WMoVCrTa with ~ 20% increase in the yield strength compared to the corresponding value at 1000 °C.
- The alloy possesses very high overall Vickers hardness of 773 HV. The density of the alloy was 11.52 gm/cm^3.
- The $W_{23}Mo_{23}V_{17}Cr_8Ta_7Fe_{22}$ powder mixture, after 48 hours of milling, exhibits a single BCC phase having the lattice parameter of 3.143 Å.
- The arc-melted alloy of $W_{23}Mo_{23}V_{17}Cr_8Ta_7Fe_{22}$ exhibits two BCC phases and a minor intermetallic phase. The lattice parameter of those two BCC phases such as BCC1 and BCC2 were determined as 3.135 Å and 2.860 Å respectively.
- $W_{23}Mo_{23}V_{17}Cr_8Ta_7Fe_{22}$ alloy exhibited very high room temperature compressive yield stress of 1688 MPa at a strain of 7.1 %. It exhibited yield strength retention of ~90% of the room temperature value at 1000 °C.
- At 1000 °C, a yield stress anomaly was observed in $W_{23}Mo_{23}V_{17}Cr_8Ta_7Fe_{22}$ with ~ 45% increase in the yield strength compared to the corresponding value at 800 °C.
- The overall room temperature Vickers hardness of the $W_{23}Mo_{23}V_{17}Cr_8Ta_7Fe_{22}$ alloy is 800 HV and the density of the alloy is 11.52 gm/cm^3.
- The yield strength and yield strain of the $W_{23}Mo_{23}V_{17}Cr_8Ta_7Fe_{22}$ at 1000 °C, are respectively about 1.9 and 1.6 times higher than that of the WMoVCrTa.

- The $Al_{10}(FeCoNiCu)_{90}$ milled powder crystallized in a major FCC1 and a minor FCC2 phases having the lattice parameters of 3.60 Å and 5.21 Å, respectively.
- The $Al_{10}(FeCoNiCu)_{90}$ alloy ingot has spinodal decomposition on the parent phase. The alloy crystallizes in FCC phase having the lattice parameter of 3.66 Å.
- The yield stress of the $Al_{10}(FeCoNiCu)_{90}$ alloy is as high as 308 MPa. The compressive stress at 40% strain of the HEA is 1406 MPa. The overall Vickers hardness and density of the alloy ingot are 160 $HV_{0.5}$ and 7.7 g/cm^3, respectively.
- The major wear mechanism in three alloys is ploughing by abrasive particles. However, wear in WMoVCrTa alloy is also assisted by delamination at 40 N load leading to increase in wear.
- The three RHEAs of WMoVCrTa and $W_{23}Mo_{23}V_{17}Cr_8Ta_7Fe_{22}$ have higher wear resistance than HSS.
- The $W_{23}Mo_{23}V_{17}Cr_8Ta_7Fe_{22}$ is a better wear resistant alloy than WMoVCrTa and HSS as its wear coefficient values are considerably lower than that of WMoVCrTa and HSS.
- The COF increases on increasing the load on the HEAs during wear test. Emergence of high amount of debris slows down the rate of increase of COF of HEAs on progressive sliding.
- The two RHEAs of WMoVCrTa and $W_{23}Mo_{23}V_{17}Cr_8Ta_7Fe_{22}$, though consist of expensive elements, appear to be viable materials for high-temperature coating applications like on gas turbine blades, cutting tools, combustion chamber lining, nuclear reactor wall, etc., due to their combination of high hardness, high strength and yield strain at elevated temperatures and good wear resistance properties.
- The $Al_{10}(FeCoNiCu)_{90}$ can be a potential material for cutting tools, turbine blades and other structural applications due to its combination of excellent stress–strain, good hardness and wear resistance properties.

5.2 Future Scope of the work

The research work though yielded some interesting results on WMoVCrTa, $W_{23}Mo_{23}V_{17}Cr_8Ta_7Fe_{22}$ and $Al_{10}(FeCoNiCu)_{90}$ HEAs; far more results can be explored for these alloys by investigating in different research approaches. Such possible approaches listed below are:

- The high temperature compressive properties of WMoVCrTa can be investigated beyond 1200°C.
- The Fe content in $W_{23}Mo_{23}V_{17}Cr_8Ta_7Fe_{22}$ can be tailored to achieve high compressive strength beyond 1000°C.
- The high temperature compressive properties of the $Al_{10}(FeCoNiCu)_{90}$ HEA can be investigated.
- The $Al_{10}(FeCoNiCu)_{90}$ HEA can be explored for biomedical applications by tailoring the concentration of Copper and Aluminum.
- The tensile, creep and fatigue properties of the HEAs can be explored.
- The oxidation and corrosion resistance of the HEAs can be investigated.

References

[1] J. W. Yeh, S. K. Chen, S. J. Lin, J. Y. Gan, T. S. Chin, T. T. Shun, C. H. Tsau and S. Y. Chang, Nanostructured High-Entropy Alloys with Multiple Principal Elements:Novel Alloy Design Concepts and Outcomes, Advanced Engineering Materials, 6 (2004) 299-303.

[2] B. Cantor, I. T. H. Chang, P. Knight, A. J. B. Vincent: Microstructural development in equiatomic multicomponent alloys. Material Science and Engineering A, 375–377 (2004) 213–218.

[3] W. Li, Di Xie, D. Li, Y. Zhang, Y. Gao, P. K. Liaw, Mechanical behavior of high-entropy alloys, Progress in Materials Science,118 (2021) 100777

[4] J. L. Qu, Z. N. Bi, J. H. Du, M. Q. Wang, Q. Z. Wang, J, Zhang, Hot deformation behavior of Nickel-based superalloy GH4720Li, Journal of Iron and Steel Research International, 18 (2011) 59-65

[5] B. S. Murty, J. W. Yeh and S. Ranganathan, High-Entropy Alloys: Elsevier, ISBN: 978-0-12-800251-3, 2014

[6] S. Guo and C. T. Liu, Phase stability in high entropy alloys: Formation of solid-solution phase or amorphous phase, Progress in Natural Science: Materials International, 21 (2011) 433-446.

[7] O.A. Waseem, J. Lee, H.M. Lee, H. J. Ryu, The effect of Ti on the sintering and mechanical properties of refractory-high entropy alloy TixWTaVCr fabricated via spark plasma sintering for fusion plasma-facing materials, Materials Chemistry and Physics, 210

(2018) 87-94.

[8] H. Kim, S. Nam, A. Roh, M. Son, M-Ho Ham, J-Hun Kim and H. Choi, Mechanical andelectrical properties of NbMoTaW refractory high-entropy alloy thin films, International Journal of Refractory Metals and Hard Materials, 80 (2019) 286-291.

[9] O. N. Senkov, G. B. Wilks, J. M. Scott and D. B. Miracle, Mechanical properties of Nb25Mo25Ta25W25 and V20Nb20Mo20Ta20W20 refractory high entropy alloys, Intermetallics, 19 (2011) 698-706.

[10] N. N. Guo, L. Wang, L. S. Luo, X. Z. Li, Y. Q. Su, J. J. Guo and H. Z. Fu, Microstructure and mechanical properties of refractory MoNbHfZrTi high-entropy alloy, Materials and Design, 81 (2015) 87–94.

[11] C. Chen, S. Pang, Y. Cheng and T. Zhang, Microstructure and mechanical properties of Al20-xCr20+0.5xFe20Co20Ni20+0.5x high entropy alloys, Journal of Alloys and Compounds, 659 (2016) 279-287.

[12] P. Zhang, Z. Li, H. Liu, Y. Zhang, H. Li, C. Shi, P. Liu, D. Yan, Recent progress on the microstructure and properties of high entropy alloy coatings prepared by laser processing technology: A review, Journal of Manufacturing Processes, 76 (2022) 397–411

[13] Y. Liu, C. Cheng, J. Shang, R.Wang, P. Li, J. Zhao, Oxidation behavior of high-entropy alloys AlxCoCrFeNi (x=0.15, 0.4) in supercritical water and comparison with HR3C steel, Transactions of Nonferrous Metals Society of China, 25 (2015) 1341–1351.

[14] J. Chen, P. Niu, T. Wei, L. Hao, Y. Liu, X. Wang and Y. Peng, Fabrication and mechanical properties of AlCoNiCrFe high-entropy alloy particle reinforced Cu matrix

composites, Journal of Alloys and Compounds, 649 (2015) 630-634.

[15] L. H. Wen, H. C. Kou, J. S. Li, H. Chang, X. Y. Xue and L. Zhou, Effect of aging temperature on microstructure and properties of AlCoCrCuFeNi high-entropy alloy, Intermetallics, 17 (2009) 266–269.

[16] S. G. Ma, J. W. Qiao, Z. H. Wang, H. J. Yang and Y. Zhang, Microstructural features and tensile behaviors of the Al0.5CrCuFeNi2 high-entropy alloys by cold rolling and subsequent annealing, Materials and Design, 88 (2015) 1057–1062.

[17] B. Schuh, F. Mendez-Martin, B. Volker, E. P. George, H. Clemens, R. Pippan and A. Hohenwarter, Mechanical properties, microstructure and thermal stability of a nanocrystalline CoCrFeMnNi high-entropy alloy after severe plastic deformation, Acta Materialia, 96 (2015) 258-268.

[18] C. Chen, S. Pang, Y. Cheng and T. Zhang, Microstructure and mechanical properties of Al20-xCr20+0.5xFe20Co20Ni20+0.5x high entropy alloys, Journal of Alloys and Compounds, 659 (2016) 279-287.

[19] A. Verma, P. Tarate, A. C. Abhyankar, M. R. Mohape, D. S. Gowtam, V. P. Deshmukh, T. Shanmugasundaram, High temperature wear in $CoCrFeNiCu_x$ high entropy alloys: The role of Cu, Scripta Materialia, 161 (2019) 28-31

[20] A. K. Mishra, S. Samal, K. Biswas, Solidification behaviour of Ti-Cu-Fe-Co-Ni high entropy alloys. Transactions of the Indian Institute of Metals, 65 (2012) 725-730.

[21] S. Mridha, S. Samal, P. Y. Khan, K. Biswas, K, Govind, Processing and consolidation of nanocrystalline Cu-Zn-Ti-Fe-Cr high-entropy alloys via mechanical alloying,

Metallurgical and Materials Transactions A, 44 (2013) 4532-4541.

[22] Y. Yu, N. Xu, S. Zhu, Z. Qiao, J. Zhang, J. Yang, W. Liu, A novel Cu-doped high entropy alloy with excellent comprehensive perfomances for marine application, Journal of Materials Science & Technology, 69 (2021) 48-59

[23] S. Das and P. S. Robi, A novel refractory WMoVCrTa high-entropy alloy possessing fine combination of compressive stress-strain and high hardness properties, Advanced Powder Technology, Doi- 10.1016/j.apt.2020.10.008

[24] E. Zhou, D. Qiao, Y. Yang, D. Xu, Y. Lu, J. Wang, J. A. Smith, H. Li, H. Zhao, P. K. Liaw, F. Wang, A novel Cu-bearing high-entropy alloy with significant antibacterial behavior against corrosive marine biofilms, 46 (2020) 201-210

[25] J. M. Sanchez, I. Vicario, J. Albizuri, T. Guraya, E. M. Acuna, Design, Microstructure and Mechanical Properties of Cast Medium Entropy Aluminium Alloys, Scientific Reports, 9 (2019) 6792

[26] C-C. Juan, M-H. Tsai, C-W. Tsai, W-L. Hsu, C-M. Lin, S-K. Chen, S-J. Lin, J-W. Yeh, Simultaneously increasing the strength and ductility of a refractory high-entropy alloy via grain refining, Materials Letters, 184 (2016), 200-203

[27] H. Chen, A. Kauffmann, B. Gorr, D. Schliephake, C. Seemüller, J.N. Wagner, H.-J. Christ, M. Heilmaier, Microstructure and mechanical properties at elevated temperatures of a new Al-containing refractory high-entropy alloy Nb-Mo-Cr-Ti-Al, Journal of Alloys and Compounds, 661 (2016) 206-215

[28] Z. Han, X. Liu, S. Zhao, Y. Shao, J. Li, K. Yao, Microstructure, phase stability and mechanical properties of Nb–Ni–Ti–Co–Zr and Nb–Ni–Ti–Co–Zr–Hf high entropy alloys, Progress in Natural Science: Materials International, 25 (2015), 365-369

[29] C-C. Juan, M-H. Tsai, C-W. Tsai, C-M. Lin, W-R. Wang, C-C. Yang, S-K. Chen, S-J. Lin, J-W. Yeh, Enhanced mechanical properties of HfMoTaTiZr and HfMoNbTaTiZr refractory high-entropy alloys, Intermetallics, 62 (2015) 76-83

[30] L. Lu and M. O. Lai, Mechanical Alloying, Boston: Kluwer Academics, 1998.

[31] A. Takeuchi and A. Inoue, Classification of Bulk Metallic Glasses by Atomic Size Difference, Heat of Mixing and Period of Constituent Elements and Its Application to Characterization of the Main Alloying Element, Materials Transactions, 46 (2005) 2817-2829.

[32] A. Takeuchi and A. Inoue, Calculations of Mixing enthalpy and Mismatch entropy for terenary amorphous alloys, Materials Transactions, JIM, 41 (2000) 1372-1378.

[33] J. W. Yeh, Recent progress in high-entropy alloys, Annales de Chimie - Science des Matériaux, 31 (2006) 633-648.

[34] D. B. Miracle, O. N. Senkov, A critical review of high entropy alloys and related concepts, Acta Materialia, 122 (2017) 448-511

[35] H. P. Chou, Y. S. Chang, S. K. Chen, J. W. Yeh, Microstructure, thermophysical and electrical properties in AlxCoCrFeNi (0 < x < 2) high-entropy alloys, Material Science Engineering B 163 (2009) 184-189.

[36] Y.-F. Kao, T.-J. Chen, S.-K. Chen, J.-W. Yeh, Microstructure and mechanical property of as-cast, -homogenized, and -deformed AlxCoCrFeNi ($0 \leq x \leq 2$) high-entropy alloys, Journal of Alloys and Compounds, 488 (2009) 57-64.

[37] C. Li, J.C. Li, M. Zhao, Q. Jiang, Effect of aluminum contents on microstructure and properties of AlxCoCrFeNi alloys, Journal of Alloys and Compounds, 504 (2010) S515-S518.

[38] C.-M. Lin, H.-L. Tsai, Effect of annealing treatment on microstructure and properties of high-entropy FeCoNiCrCu0.5 alloy, Materials Chemistry and Physics, 128 (2011) 50-56.

[39] C. Li, J.C. Li, M. Zhao, Q. Jiang, Effect of alloying elements on microstructure and properties of multiprincipal elements high-entropy alloys, Journal of Alloys and Compounds, 475 (2009) 752-757.

[40] H.B. Cui, L.F. Zheng, J.Y. Wang, Microstructure evolution and corrosion behavior of directionally solidified FeCoNiCrCu high entropy alloy, Appl.Mech. Mater 66-68 (2011) 146-149.

[41] Y. Zhang, Y.J. Zhou, J.P. Lin, G.L. Chen, P.K. Liaw, Solid-solution phase formation rules for multi-component alloys, Adv. Eng. Mater. 10 (2008) 534-538.

[42] X. Wang, H. Xie, L. Jia, Z.L. Lu, Effect of Ti, Al and Cu addition on structural evolution and phase constitution of FeCoNi system equimolar alloys, Mater. Sci. Forum 724 (2012) 335-338.

[43] B. Cantor, Multicomponent and high entropy alloys, Entropy 16 (2014) 4749-4768.

[44] A. Gali, E.P. George, Tensile properties of high- and medium-entropy alloys, Intermetallics 39 (2013) 74-78.

[45] R. Kozak, A. Sologubenko, W. Steurer, Single-phase high-entropy alloys – an overview, Z. Krist. 230 (2015) 55-68.

[46] F.Y. Tian, L.K. Varga, N. Chen, J. Shen, L. Vitos, Empirical design of single phase high-

entropy alloys with high hardness, Intermetallics 58 (2015) 1-6.

[47] O.N. Senkov, G.B. Wilks, D.B. Miracle, C.P. Chuang, P.K. Liaw, Refractory high entropy alloys, Intermetallics 18 (2010) 1758-1765.

[48] O.N. Senkov, S.V. Senkova, C. Woodward, D.B. Miracle, Low-density, refractory multi-principal element alloys of the Cr-Nb-Ti-V-Zr system: Microstructure and phase analysis, Acta Mater 61 (2013) 1545-1557.

[49] Y.D. Wu, Y.H. Cai, T. Wang, J.J. Si, J. Zhu, Y.D. Wang, X.D. Hui, A refractory Hf25Nb25Ti25Zr25 high-entropy alloy with excellent structural stability and tensile properties, Mater. Lett. 130 (2014) 277-280.

[50] S. Maiti, W. Steurer, Structure and properties of refractory high-entropy alloys, in: 143rd Annual Meeting and Exhibition, TMS 2014, February 16, 2014-February 20, 2014. San Diego, CA, United states, Minerals, Metals and Materials Society, 2014, pp. 1093-1097.

[51] N.D. Stepanov, D.G. Shaysultanov, G.A. Salishchev, M.A. Tikhonovsky, Structure and mechanical properties of a light-weight AlNbTiV high entropy alloy, Mater. Lett. 142 (2015) 153-155.

[52] C.-J. Tong, Y.-L. Chen, S.-K. Chen, J.-W. Yeh, T.-T. Shun, C.-H. Tsau, S.-J. Lin, S.- Y. Chang, Microstructure characterization of AlxCoCrCuFeNi high-entropy alloy system with multiprincipal elements, Metall. Mater. Trans. A 36A (2005) 881-893.

[53] Y. Zhang, G. L. Chen, C. L. Gan, Phase change and mechanical behaviors of $Ti_xCoCrFeNiCu_{1-y}Al_y$ high entropy alloys, J. ASTM International, 7(5) (2010) 102527.

[54] V. Vitek, T. Egami, Atomic level stresses in solids and liquids, Physica Status Solidi B, 144 (1987) 145–56.

[55] T. Egami, Atomic level stresses, Progress in Materials Science, 56 (2011) 637–653.

[56] C. Ng, S. Guo, J. Luan, S. Shi, C. T, Liu, Entropy driven phase stability and slow diffusion kinetics in an Al0.5CoCrCuFeNi high entropy alloy, Intermetallics, 31 (2012) 165–172.

[57] W.P. Chen, Z.Q. Fu, S.C. Fang, H.Q. Xiao, D.Z. Zhu, Alloying behavior, microstructure

and mechanical properties in a FeNiCrCo0.3Al0.7 high entropy alloy, Mater. Des. 51 (2013) 854-860.

[58] Y. Dong, K.Y. Zhou, Y. Lu, X.X. Gao, T.M. Wang, T.J. Li, Effect of vanadium addition on the microstructure and properties of AlCoCrFeNi high entropy alloy, Mater. Des. 57 (2014) 67-72.

[59] S. Varalakshmi, M. Kamaraj, B.S. Murty, Formation and stability of equiatomic and nonequiatomic nanocrystalline CuNiCoZnAlTi high-entropy alloys by mechanical alloying, Metall. Mater. Trans. A 41A (2010) 2703-2709.

[60] C. Wang, W. Ji, Z.Y. Fu, Mechanical alloying and spark plasma sintering of CoCrFeNiMnAl high-entropy alloy, Adv. Powder Technol. 25 (2014) 1334-1338.

[61] W. Ji, Z. Fu, W. Wang, H. Wang, J. Zhang, Y. Wang, F. Zhang, Mechanical alloying synthesis and spark plasma sintering of CoCrFeNiAl high-entropy alloy, J. Alloys Compd. 589 (2014) 61-66.

[62] S. Fang, W. Chen, Z. Fu, Microstructure and mechanical properties of twinned Al0.5CrFeNiCo0.3C0.2 high entropy alloy processed by mechanical alloying and spark plasma sintering, Mater. Des. 54 (2014) 973-979.

[63] P. Jinhong, P. Ye, Z. Hui, Z. Lu, Microstructure and properties of AlCrFeCuNix (0.6<x<1.4) high-entropy alloys, Mater. Sci. Eng. A 534 (2012) 228-233.

[64] X.-W. Qiu, Microstructure and properties of AlCrFeNiCoCu high entropy alloy prepared by powder metallurgy, J. Alloys Compd. 555 (2013) 246-249.

[65] J.-H. Pi, Y. Pan, L. Zhang, H. Zhang, Microstructure and property of AlTiCrFeNiCu high-entropy alloy, J. Alloys Compd. 509 (2011) 5641-5645.

[66] S. Varalakshmi, M. Kamaraj, B.S. Murty, Processing and properties of nanocrystalline CuNiCoZnAlTi high entropy alloys by mechanical alloying, Mater. Sci. Eng. A 527

(2010) 1027-1030.

[67] W. Chen, Z. Fu, S. Fang, Y. Wang, H. Xiao, D. Zhu, Processing, microstructure and properties of Al0.6CoNiFeTi0.4 high entropy alloy with nanoscale twins, Mater. Sci. Eng. A 565 (2013) 439-444.

[68] C.-C. Tung, J.-W. Yeh, T.-T. Shun, S.-K. Chen, Y.-S. Huang, H.-C. Chen, On the elemental effect of AlCoCrCuFeNi high-entropy alloy system, Materials Letters, 61 (2007) 1-5.

[69] M.V. Ivchenko, V.G. Pushin, N. Wanderka, High-entropy equiatomic AlCrFeCoNiCu alloy: hypotheses and experimental data, Tech. Phys. 59 (2014) 211-223.

[70] B.A. Welk, R.E.A. Williams, G.B. Viswanathan, M.A. Gibson, P.K. Liaw, H.L. Fraser, Nature of the interfaces between the constituent phases in the high entropy alloy CoCrCuFeNiAl, Ultramicroscopy 134 (2013) 193-199.

[71] N.D. Stepanov, D.G. Shaysultanov, G.A. Salishchev, M.A. Tikhonovsky, E.E. Oleynik, A.S. Tortika, O.N. Senkov, Effect of V content on microstructure and mechanical properties of the CoCrFeMnNiVx high entropy alloys, J. Alloys Compd. 628 (2015) 170-185.

[72] C.-Y. Hsu, W.-R. Wang, W.-Y. Tang, S.-K. Chen, J.-W. Yeh, Microstructure and mechanical properties of new AlCoxCrFeMo0.5Ni high-entropy alloys, Adv. Eng. Mater. 12 (2010) 44-49.

[73] M.-R. Chen, S.-J. Lin, J.-W. Yeh, S.-K. Chen, Y.-S. Huang, M.-H. Chuang, Effect of vanadium addition on the microstructure, hardness, and wear resistance of Al0.5CoCrCuFeNi high-entropy alloy, Metall. Mater. Trans. A 37 (2006) 1363-1369.

[74] T. T. Shun, L. Y. Chang, M. H. Shiu, Microstructure and mechanical properties of multiprincipal component CoCrFeNiMo*x* alloys, Materials Characterization, 70 (2012)

63–67.

[75] M. R. Chen, S. J. Lin, J. W. Yeh, S. K. Chen, Y. S. Huang, C.P. Tu. Microstructure and properties of Al0.5CoCrCuFeNiTix (x = 0–2.0) high-entropy alloys. Mater Trans. 47 (2006) 1395–1401.

[76] M.H. Chuang, M.H. Tsai, W.R. Wang, S.J. Lin, J.W. Yeh, Microstructure and wear behavior of Al*x*Co1.5CrFeNi1.5 Ti*y* high-entropy alloys. Acta Materialia 59 (2011) 6308–6317.

[77] M.H. Tsai, H. Yuan, G. Cheng, W. Xu, W.W. Jian, M.H. Chuang, C.C. Juan, A.C. Yeh, S.J. Lin, Y. Zhu, Significant hardening due to the formation of a sigma phase matrix in a high entropy alloy, Intermetallics, 33 (2013) 81–86

[78] S. Liu, M.C. Gao, P.K. Liaw, Y. Zhang, Microstructures and mechanical properties of AlxCrFeNiTi0.25 alloys, J. Alloys Compd. 619 (2015) 610-615.

[79] G.A. Salishchev, M.A. Tikhonovsky, D.G. Shaysultanov, N.D. Stepanov, A.V. Kuznetsov, I.V. Kolodiy, A.S. Tortika, O.N. Senkov, Effect of Mn and V on structure and mechanical properties of high-entropy alloys based on CoCrFeNi system, J. Alloys Compd, 591 (2014) 11-21.

[80] Y.X. Zhuang, H.D. Xue, Z.Y. Chen, Z.Y. Hu, J.C. He, Effect of annealing treatment on microstructures and mechanical properties of FeCoNiCuAl high entropy alloys, Mater. Sci. Eng. A 572 (2013) 30-35.

[81] F. Otto, A. Dlouhy, C. Somsen, H. Bei, G. Eggler, E.P. George, The influences of temperature and microstructure on the tensile properties of a CoCrFeMnNi high-entropy alloy, Acta Mater 61 (2013) 5743-5755.

[82] N. Stepanov, M. Tikhonovsky, N. Yurchenko, D. Zyabkin, M. Klimova, S. Zherebtsov, A. Efimov, G. Salishchev, Effect of cryo-deformation on structure and properties of

CoCrFeNiMn high-entropy alloy, Intermetallics 59 (2015) 8-17.

[83] D.G. Shaysultanov, N.D. Stepanov, A.V. Kuznetsov, G.A. Salishchev, O.N. Senkov, Phase composition and superplastic behavior of a wrought AlCoCrCuFeNi high-entropy alloy, JOM 65 (2013) 1815-1828.

[84] A.V. Kuznetsov, D.G. Shaysultanov, N.D. Stepanov, G.A. Salishchev, O.N. Senkov, Tensile properties of an AlCrCuNiFeCo high-entropy alloy in as-cast and wrought conditions, Mater. Sci. Eng. A 533 (2012) 107-118.

[85] A.V. Kuznetsov, D.G. Shaysultanov, N.D. Stepanov, G.A. Salishchev, O.N. Senkov, Superplasticity of AlCoCrCuFeNi high entropy alloy, Mater. Sci. Forum 735 (2013) 146-151.

[86] L. Liu, J.B. Zhu, L. Li, J.C. Li, Q. Jiang, Microstructure and tensile properties of FeMnNiCuCoSnx high entropy alloys, Mater. Des. 44 (2013) 223-227.

[87] L. Liu, J.B. Zhu, C. Zhang, J.C. Li, Q. Jiang, Microstructure and the properties of FeCoCuNiSnx high entropy alloys, Mater. Sci. Eng. A 548 (2012) 64-68.

[88] S.G. Ma, S.F. Zhang, J.W. Qiao, Z.H. Wang, M.C. Gao, Z.M. Jiao, H.J. Yang, Y. Zhang, Superior high tensile elongation of a single-crystal CoCrFeNiAl0.3 high-entropy alloy by Bridgman solidification, Intermetallics 54 (2014) 104-109.

[89] N. Stepanov, M. Tikhonovsky, N. Yurchenko, D. Zyabkin, M. Klimova, S. Zherebtsov, A. Efimov, G. Salishchev, Effect of cryo-deformation on structure and properties of CoCrFeNiMn high-entropy alloy, Inter-metallics, 2015, 59, 8-17.

[90] J. W. Qiao, S. G. Ma, E. W. Huang, C. P. Chuang, P. K. Liaw and Y. Zhang, Microstructural characteristics and mechanical behaviors of AlCoCrFeNi high-entropy alloys at ambient and cryogenic Temperatures, Materials Science Forum, 2011, 688, 419-425.

[91] M. H. Chuang, M. H. Tsai, W. R. Wang , S. J. Lin , J. W. Yeh, Microstructure and wear behavior of AlxCo1.5CrFeNi1.5Tiy high-entropy alloys, ActaMaterialia, 2011, 59, 6308-6317.

[92] J. M. Wu, S. J. Lin, J. W. Yeh , S. k. Chen, Y. S Huang, H. C Chen, Adhesive wear behavior of Al*x*CoCrCuFeNi high-entropy alloys as a function of aluminum content, Wear, 2006, 261, 513-519.

[93] S. Das, S. K. Nishad and P. S. Robi, A New High-Entropy Alloy of Al-Fe-Co-Ni-Cu Possessing Single FCC Crystal Structure and Excellent Mechanical Properties at Room Temperature, Physica status solidi A, 218 (2021) 2000825

[94] M.A. Hemphill, T. Yuan, A.M. Wang, J.-W. Yeh, C.-W. Tsai, A. Chuang, P.K. Liaw, Fatigue behavior of Al0.5CoCrCuFeNi high entropy alloys, Acta Materialia 60 (2012) 5723-5734.

[95] U. Roy, H. Roy, H. Daoud, U. Glatzel, K.K. Ray, Fracture toughness and fracture micromechanism in a cast AlCoCrCuFeNi high entropy alloy system, Mater. Lett. 132 (2014) 186-189.

[96] B. Gludovatz, A. Hohenwarter, D. Catoor, E.H. Chang, E.P. George, R.O. Ritchie, A fracture-resistant high-entropy alloy for cryogenic applications, Science 345 (2014) 1153-1158.

[97] A.J. Zaddach, R.O. Scattergood, C.C. Koch, Tensile properties of low-stacking fault energy high-entropy alloys, Mat. Sci. Eng. A 636 (2015) 373-378.

[98] Z. Wu, H. Bei, G.M. Pharr, E.P. George, Temperature dependence of the mechanical properties of equiatomic solid solution alloys with face-centered cubic crystal structures, Acta Mater 81 (2014) 428-441.

[99] O.N. Senkov, S.V. Senkova, D.M. Dimiduk, C. Woodward, D.B. Miracle, Oxidation

behavior of a refractory NbCrMo0.5Ta0.5TiZr alloy, J. Mater. Sci. 47 (2012) 6522e6534.

[100] O.N. Senkov, S.V. Senkova, C. Woodward, Effect of aluminum on the microstructure and properties of two refractory high entropy alloys, Acta Materialia 68 (2014) 214-228.

[101] O. N. Senkov, G. B. Wilks, D.B. Miracle, C.P. Chuang, P.K. Liaw. Refractory high-entropy alloys. Intermetallics 2010;18:1758–65.

[102] O. N. Senkov, J.M. Scott, S.V. Senkova, D.B. Miracle, C.F. Woodward. Microstructure and room temperature properties of a high-entropy TaNbHfZrTi alloy. Journal of Alloys and Compounds, 509 (2011) 6043–6048.

[103] E. Fazakas, V. Zadorozhnyy, L.K. Varga, A. Inoue, D.V. Louzguine-Luzgin, F. Tian, L. Vitos, Experimental and theoretical study of Ti20Zr20Hf20Nb20X20 (X ¼ V or Cr) refractory high-entropy alloys, Int. J. Refract. Met. Hard Mater 47 (2014) 131-138.

[104] O.N. Senkov, C.F. Woodward, Microstructure and properties of a refractory NbCrMo0.5Ta0.5TiZr alloy, Mater. Sci. Eng. A 529 (2011) 311-320.

[105] Y. Zou, S. Maiti, W. Steurer, R. Spolenak, Size-dependent plasticity in an Nb25Mo25Ta25W25 refractory high-entropy alloy, Acta Materialia 65 (2014) 85-97.

[106] O.N. Senkov, C. Woodward, D.B. Miracle, Microstructure and properties of aluminum-containing refractory high-entropy alloys, JOM 66 (2014) 2030-2042.

[107] O.N. Senkov, S.V. Senkova, D.B. Miracle, C. Woodward, Mechanical properties of low-density, refractory multi-principal element alloys of the Cr-Nb-Ti-V-Zr system, Mater. Sci. Eng. A 565 (2013) 51-62.

[108] O.N. Senkov, S.L. Semiatin, Microstructure and properties of a refractory high-entropy alloy after cold working, J. Alloys Compd. 649 (2015) 1110-1123.

[109] C.M. Liu, H.M. Wang, S.Q. Zhang, H.B. Tang, A.L. Zhang, Microstructure and oxidation behavior of new refractory high entropy alloys, J. Alloys Compd, 583 (2014) 162-169.

[110] A. Poulia, E. Georgatis, A. Lekatou, A. E. Karantzalis, Microstructure and wear behavior of a refractory high entropy alloy, International Journal of Refractory Metals and Hard Materials, 57 (2016) 50-63

[111] V. Bhardwaj, Q. Zhou, F. Zhang, W. Han, Y. Du, K. Hua, H. Wang, Effect of Al addition on the microstructure, mechanical and wear properties of TiZrNbHf refractory high entropy alloys, Tribology International, 160 (2021) 107031

[112] M. Sadeghilaridjani, M. Pole , S. Jha , S. Muskeri , N. Ghodki , S. Mukherjee, Deformation and tribological behavior of ductile refractory high-entropy alloys, Wear, 478-479 (2021) 203916

[113] M. Pole, M. Sadeghilaridjani, J. Shittu , A. Ayyagari , S. Mukherjee, High temperature wear behavior of refractory high entropy alloys based on 4-5-6 elemental palette, Journal of Alloys and Compounds, 843 (2020) 156004

[114] D. Yim, M.J. Jang, J.W. Bae, J. Moon, C.-H. Lee, S.-J. Hong, S.I. Hong, H.S. Kim, Compaction behaviour of water-atomized CoCrFeMnNi high-entropy alloy powders, Mater. Chem. Phys. xxx (2017) 1–8.

[115] K.B. Zhang, Z.Y. Fu, J.Y. Zhang, W.M. Wang, S.W. Lee, K. Niihara, Characterization of nanocrystalline CoCrFeNiTiAl high-entropy solid solution processed by mechanical alloying, J. Alloy. Compd. 495 (2010) 33–38.

[116] H. Jiang, H. Zhang, T. Huang, Y. Lu, T. Wang, T. Li, Microstructures and mechanical properties of Co2MoxNi2VWx eutectic high entropy alloys, Materials & Design, 109 (2016) 539–546.

[117] Y.D. Wu, Y.H. Cai, X.H. Chen, T. Wang, J.J. Si, L. Wang, Y.D. Wang, X.D. Hui, Phase composition and solid solution strengthening effect in TiZrNbMoV highentropy alloys, Mater. Des. 83 (2015) 651–660.

[118] A. Dwivedi, C.C. Koch, K.V. Rajulapati, Powder metallurgy processing of ruthenium aluminium alloys, J. Mater. Process. Technol. 153–154 (2004) 952– 957.

[119] A. Dwivedi, C.C. Koch, K.V. Rajulapati, On the single phase fcc solid solution in nanocrystalline Cr-Nb-Ti-V-Zn high-entropy alloy, Mater. Lett. 183 (2016) 44–47.

[120] D. Caillard, Yield-stress anomalies and high-temperature mechanical properties of intermetallics and disordered alloys, Mater. Sci. Eng. A 319–321 (2001) 74–83.

[121] N.Yurchenko, E.Panina, A.Belyakov, G.Salishchev, S.Zherebtsov, N.Stepanov, On the yield stress anomaly in a B2-ordered refractory AlNbTiVZr0.25 high-entropy alloy, Materials Letters, 311 (2022) 13154

[122] T. Lienig, C. Thomas, M. Feuerbacher ,Yield-stress anomaly in equiatomic ZrNbTiVHf high-entropy alloys, Condensed matter>materials science, arXiv:1911.01887v1, Doi-https://doi.org/10.48550/arXiv.1911.01887

[123] Y.Lu, J.Yamada, R.Miyata, H.Kato, K.Yoshimia, High-temperature mechanical behavior of B2-ordered Ti–Mo–Al alloys, Intermetallics, 117 (2020) 106675

[124] D. M. Nuruzzaman, M. A. Chowdhury, Effect of Normal Load and Sliding Velocity on Friction Coefficient of Aluminum Sliding Against Different Pin Materials, American Journal of Materials Science 2 (2012) 26-31

[125] E. Rabinowicz, Friction and Wear of Materials, 2nd Edition, Wiley, New York (1995)

[126] M. W. Glasscott, Classifying and benchmarking high-entropy alloys and associated materials for electrocatalysis: A brief, Current Opinion in Electrochemistry, 34 (2022) 100976

[127] I.M. Hutchings, Tribology-Friction and Wear of Engineering Materials, Butterworth-Heinemann, 1992.

[128] B.D. Cullity, S.R. Stock, Elements of X-Ray Diffraction, 3rd ed., Pearson, 2001, ISBN : 0201610914.

[129] L. B¨ornstein, Binary Systems Form Mn–Mo to Y–Zr. Phase Diagrams, Phase Transition Data, Integral and Partial Quantities of Alloys, Springer, Berlin, Heidelberg, 2006 (Part 4).

[130] B. Gorr, M. Azim, H.-J. Christ, T. Mueller, D. Schliephake, M. Heilmaier, Phase equilibria, microstructure and high temperature oxidation resistance of novel refractory high-entropy alloys, J. Alloys Compd. 624 (2015) 270–278.

[131] Z. Han, X. Liu, S. Zhao, Y. Shao, J. Li, K. Yao, Microstructure, phase stability and mechanical properties of Nb–Ni–Ti–Co–Zr and Nb–Ni–Ti–Co–Zr–Hf high entropy alloys, Prog. NaT. ScI. Mater. Int. 25 (2015) 365–369.

[132] S. Das and P. S. Robi, Processing and Characterization of $W_{23}Mo_{23}V_{17}Cr_8Ta_7Fe_{22}$ and WMoVCrTa Refractory High Entropy Alloys, International Journal of Refractory Metals and Hard Materials, 100 (2021) 105656

[133] C. Suryanarayana, Mechanical alloying and milling, Progress in Materials Science, 46 (2001) 1.

[134] Friction, Lubrication, and Wear Technology, ASM Handbook, Volume 18, 1992

[135] S. E. Sunbul, K. Icin, F. Z. Seren, O. Sahin, D. D. Kakil, R. Sezer, S. Ozturk, Determination of structural, tribological, isothermal oxidation and corrosion properties of Al–Co–Cr–Fe–Ni–Ti–Cu high-entropy alloy, Vacuum 187 (2021) 110072

[136] K. V. Acker, D. Vanhoyweghen, R. Persoons and J. Vangrunderbeek, Influence of tungsten carbide particle size and distribution on the wear resistance of laser clad WC/Ni coatings , WEAR, 258 (2005) 194–202

List of Publications

1. S. Das and P. S. Robi, A novel refractory WMoVCrTa high-entropy alloy possessing fine combination of compressive stress-strain and high hardness properties, Advanced Powder Technology, 31 (2020) 4619-4631
2. S. Das, S. K. Nishad and P. S. Robi, A New High-Entropy Alloy of Al-Fe-Co-Ni-Cu Possessing Single FCC Crystal Structure and Excellent Mechanical Properties at Room Temperature, Physica status solidi A, 218 (2021) 2000825
3. S. Das and P. S. Robi, Processing and Characterization of $W_{23}Mo_{23}V_{17}Cr_8Ta_7Fe_{22}$ and WMoVCrTa Refractory High Entropy Alloys, International Journal of Refractory Metals and Hard Materials, 100 (2021) 105656
4. Sujit Das, P. S Robi, Tribological Properties of $(Al)_{10}(FeCoNiCu)_{90}$ High Entropy Alloy, Tribology- Materials, Surfaces & Interfaces, doi:10.1080/17515831.2023.2168771
5. S. Das and P. S. Robi, Processing and Characterizations of Powder of the AlCoCuFeNi High Entropy Alloy, Emergent Materials, doi: 10.1007/s42247-023-00466-3
6. Sujit Das, P. S Robi, Mechanical Alloying of W-Mo-V-Cr-Ta High Entropy Alloys, IOP Conference Series: Materials Science and Engineering, 346 (2018) 012047, doi:10.1088/1757-899X/346/1/012047
7. Sujit Das, P. S Robi, Tribological Properties of WMoVCrTa and $W_{23}Mo_{23}V_{17}Cr_8Ta_7Fe_{22}$ Refractory High Entropy Alloys, Journal of Tribology, Under review